UNIVERSITY of GLASGOW

Physical Science Graduate School

Department of Physics and Astronomy

Signal generation in highly irradiated silicon microstrip detectors for the ATLAS experiment

PhD Thesis

Gennaro Ruggiero

Supervisors:

Prof. Kenway Smith

Dr. Vladimir Eremin

Dr. Mahfuzur Rahman

Dr. Shaun Roe

Abstract

Silicon detectors are the most diffused tracking devices in High Energy Physics (HEP). The reason of such success can be found in the characteristics of the material together with the existing advanced technology for the fabrication of these devices. Nevertheless in many modern HEP experiments the observation of vary rare events require data taking at high luminosity with a consequent extremely intense hadron radiation field that damages the silicon and degrades the performance of these devices.

In this thesis work a detailed study of the signal generation in microstrip detectors has been produced with a special care for the ATLAS semiconductor tracker geometry. This has required a development of an appropriate setup to perform measurements with Transient Current/ Charge Technique. This has allowed studying the evolution of the signal in several microstrips detector samples irradiated at fluences covering the range expected in the ATLAS Semiconductor Tracker. For a better understanding of these measurements a powerful software package that simulates the signal generation in these devices has been developed.

Moreover in this thesis it has been also shown that the degradation due to radiation in silicon detectors can be strongly reduced if the data taking is done with detectors operated at 130 K. This makes low temperature operation that benefits of the recovery of the charge collection efficiency in highly irradiated silicon detectors (also known as *Lazarus effect*) an optimal option for future high luminosity experiments.

to my brother Vincenzo,
in his loving memory.

"Life is what happens to you when
you are busy doing other things"
John Lennon

Acknowledgements

Finally I have the chance to express all my gratefulness to all the people who have supported me during my PhD work. First of all I am grateful to Prof. Kenway Smith who believed in my potential and offered me a PhD studentship in his wonderful group in the Physics and Astronomy department of the Glasgow University. Besides his great competence, his humanity makes of him a unique person. He has always encouraged me to overcome the difficulties that I met during all these years. A special acknowledgement goes also to Dr. Shaun Roe for choosing me as doctoral student in his group at CERN. I had a great chance of having him as supervisor and I owe him a lot. I will always be grateful to him for having introduced me to numerical simulation of semiconductor devices. I feel very much in debt also with Dr. Vladimir Eremin for all he has taught me about silicon detectors and radiation damage. My collaboration with him has been very precious. We have worked a lot together very intensively and always with great pleasure.

I also want to acknowledge Prof. Peter Weilhammer, Dr. Luca Casagrande, Eng. Richard Fortin, Eng. Birgitte Herskind, Dr. Zhang Li, Dr. Tapio Niinikoski, Dr. Valentine O'Shea, Dr. Vittorio Palmieri, Dr. Terry Pritchard, Dr. Mahfuzur Raman, Eng. Alan Rudge, Dr. Francesco Tramontano and Dr. Elena Verbitskaia for fruitful discussions and support. Dr. Cinzia Da Via and Prof. Steve Watts are greatly acknowledged for their support especially in the last year of my thesis work. Greatly acknowledged are also the Secretaries Mrs Sue Ferrand and Miss Catherine MacIntyre for simplifying my life with bureaucracy many times.

My parents, Francesco and Angela and my sister Nunzia have been of great support in these years for all their joy in welcoming me in my trips back to my hometown Napoli. Nevertheless I never felt alone in Geneva, Ioana has been always taking care of me greatly. I must admit that she has had a lot of patience with me and for that I will always be grateful to her. Moreover I was always surrounded by friends, in Glasgow as in Geneva. A special mention goes to Steven, who is also a great trombone player and Hugues, probably the best Catamaran sailor of Lac Léman.

This thesis is dedicated to my brother Vincenzo who disappeared in the years of my thesis, leaving in my heart an unfillable void. He has been my guide for many

choices I have made in my life. It was my deep admiration and sense of emulation that I had for him that led me to choose a scientific profile through all my studies. He has been my first physics' teacher and I am sure he would be proud now to see how far I have gone.

Declaration

Except where explicit reference is made to the work of the others, this dissertation is the result of my own work. None of this material has been submitted for any other degree at the University of Glasgow or any other institution.

Gennaro Ruggiero

Table of Contents

1 Introduction

1.1 The Standard Model

In the second half of the last century theoretical and experimental studies in high energy physics have produced the most comprehensive theory of modern physics: the Standard Model [1]. The Standard Model is a relativistic quantum field theory describing the behaviour and the interactions between the elementary particles of matter. The gauge symmetry group of the SM is given by:

$$G_{SM} = U(1)_Y \otimes SU(2)_L \otimes SU(3)_C \qquad (1)$$

where each group corresponds to the three forces of the SM: the electromagnetism and weak (nuclear) force, unified by the electroweak group of symmetry $U(1)_Y \otimes SU(2)_L$ and the strong nuclear interaction. Gravity is not taken into account because of the difficulties of describing it in a quantum theory. The types of particles foreseen in the SM are of two kinds: the fermions (with spin 1/2) and the bosons (with spin 1). While fermions build matter, bosons transmit the interaction between the particles of matter. Fermions are divided in two classes: leptons and quarks. All fermions interact electroweakly but only quarks experience strong interactions. In Figure 1 are shown the different relations between interactions, the bosons and the fermions.

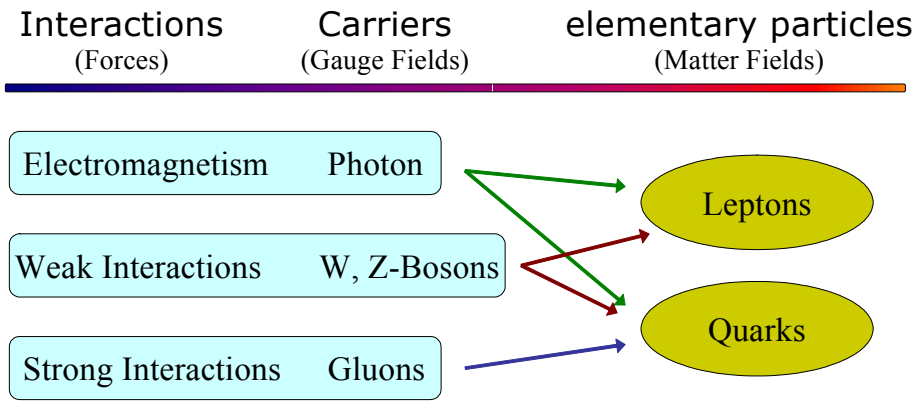

Figure 1 Schematic of relations between SM interactions their gauge bosons and fermions.

Fermions can be further divided into three generations of particles each composed of a weak isospin doublet of massive quarks (one charged *2/3e* and the other charged *-1/3e* with *-e* the electron charge) and a weak isospin doublet of leptons (a massive lepton charged *–e* and a massless neutral neutrino). The first generation contains all the particles to make stable matter: the up and the down quarks, the electron and its neutrino. Nevertheless, two more generations also exist: the charm and strange quarks with the muon and its neutrino and the top and bottom quarks with the tau lepton and its neutrino. Among them the top quark has been discovered only a few years ago [2].

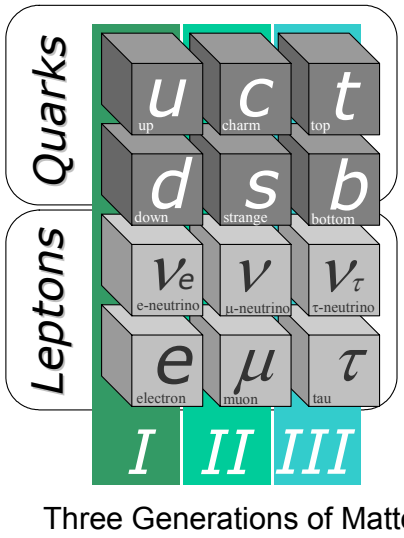

Figure 2 Representation of the three generations of Leptons and Quarks.

The electroweak interactions are mediated via four bosons: the massless photon, responsible for electromagnetic interactions, two massive charged bosons $W^{\pm}$ (M_W~80 GeV) responsible for the charged weak interactions, and a massive neutral boson Z^0 responsible for the weak neutral currents. The introduction of bosons with mass breaks the gauge invariance of the theory and makes it non-renormalisable. The acquisition of masses for bosons is done via spontaneous symmetry breaking of the Higgs field which has a non zero expectation value. This mechanism introduces an additional spin 0 particle, the Higgs boson, but the theory does not predict its mass. Moreover by adding an arbitrary 'Yukawa' coupling of the Higgs field to all the other particles, they can be given mass while preserving the gauge invariance.

1.2 Incompleteness of the Standard Model

Despite the success of the Standard Model, confirmation of a vital part has yet to come from discovery of the Higgs boson postulated. Nevertheless there are still strong questions that the SM has so far failed to address. A review of these can be found in [3], here we will summarise a few of them:

- The Standard Model contains 26 unspecified parameters, i.e. the particle masses and the coupling constants. Although the Higgs mechanism provides masses for quark and leptons via Yukawa coupling, the Standard Model fails to predict them as they have to be put in 'manually' with values derived from experiments. Moreover, the spread in the observed mass spectrum has no justification.
- Stable matter requires only fermions from the first generation nevertheless three generations exist. The Standard Model does not account for this and even more fermion generations are theoretically possible.
- Astronomical observations have shown that the universe contains a large fraction of non luminous matter. The origin of this non-baryonic dark matter is still unknown and lies outside the Standard Model.

These previous and other inadequacies have been addressed by some theories which aim to extend the SM. Among them Supersymmetry (SUSY) [3] based on an additional symmetry that, involving superheavy gauge bosons, exchanges fermions and bosons.

1.3 Necessity of LHC

The demand of studying the SM in greater detail and to search for evidence beyond it requires a high energy, high luminosity collider. The Large Hadron Collider [5] (LHC) has been designed to address these issues. The primary physics goal at the LHC is to search for the Standard Model Higgs boson. The mass of the Higgs boson is expected to be in the range 90 GeV$<m_H<$1 TeV. Some of the best experimental signatures for observing the Higgs are expected to be:

$$
\begin{aligned}
H &\to \gamma\gamma && if \quad m_H < 2m_Z \\
ttH &\to lbb + X \\
H &\to ZZ^* \to 4leptons \\
H &\to WW^{(*)} \to lvlv \\
H &\to ZZ \to 4leptons, llvv, llqq && if \quad m_H > 2m_Z \\
H &\to WW \to lv\bar{q}q
\end{aligned}
$$

The LHC that is scheduled to start operation in 2007 has two counter-rotating proton beams each with maximum energy of 7 TeV giving total collision energy in the centre of mass of 14 TeV. This energy is limited by the radius of the tunnel hosting the machine (once the tunnel where the LEP collider was situated) and the bending magnetic field for which 8.65 T magnets are used. The LHC will have a dynamic range of discovery from energy scales of 5 MeV, also allowing investigations of b-physics, to a few TeV for the discovery of new vector bosons or quark compositeness.

The luminosity of a particle collider is defined as:

$$L = \frac{1}{4\pi} \frac{N^2 f}{t A_T} \tag{2}$$

where N is the number of particles in each bunch, t the time between individual bunches, A_T the transverse dimension of the bunches at the interaction points and f the fraction of bunch positions actually containing particles.

This parameter is linked to event rates of specific processes by:

$$n_x = \sigma_x L \tag{3}$$

where σ_x is the cross section of the process. So high event rates require high luminosity.

The time between bunches is limited by the requirement that there should be no additional interactions on each side of the interaction region and the time resolution of the experiment. For the LHC the bunch crossing time will be 25 ns corresponding to approximately 23 interactions per bunch. The transverse dimensions of the beam can be a few microns at the interaction point. To be able to inject new

bunches into the LHC and to operate the beam dump it is necessary to order the proton bunches in bunch trains followed by some empty bunches. In total 2835 of the 3557 available positions with 25 ns separation will contain protons corresponding to f=0.80. The only remaining way to increase the luminosity is to increase the number of protons per bunch but this is limited by electromagnetic forces.

The nominal luminosity is fixed at 10^{34} $cm^{-2}s^{-1}$ but for the first years of operation it is foreseen to run at a lower luminosity $L_{low}=10^{33}cm^{-2}s^{-1}$ and increase it gradually to the nominal value [5].

1.4 The Atlas Detector

ATLAS ("A Toroidal Lhc ApparatuS") is a general-purpose *p-p* spectrometer designed to exploit the full discovery potential of the LHC. The detector concept and its physics potential have been presented in the Technical Proposal [6] in 1994 and in different Technical Design Reports [7]. The overall detector layout, as shown in Figure 3, has a cylindrical symmetry with a total length of 42 m and a radius of 11 m.

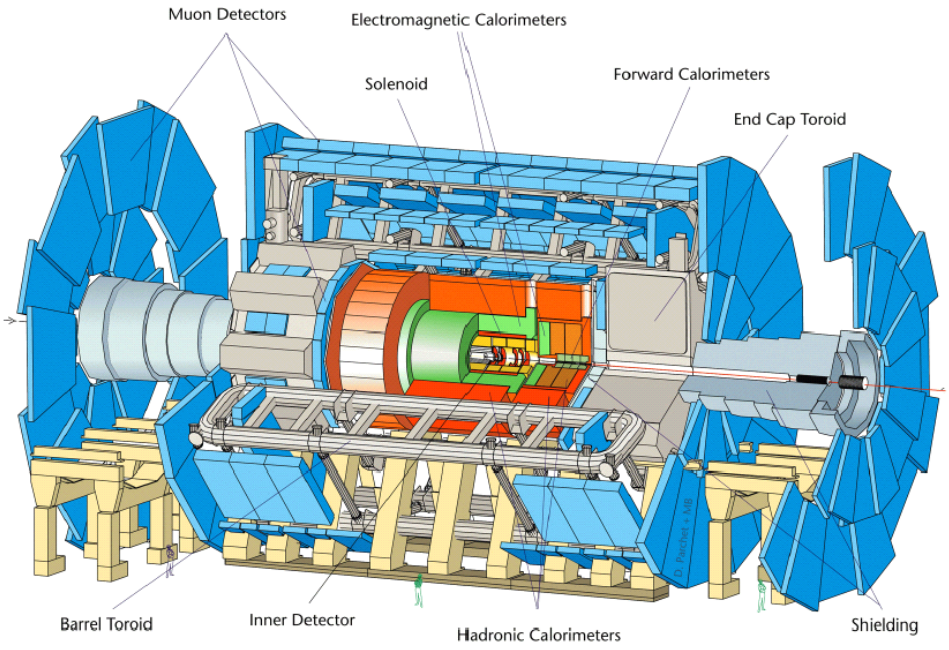

Figure 3 General overview of the ATLAS Detector

The detector will be installed 100 m under ground level in the cavern Ux15, at the interaction point 1 of the LHC. The underground facilities of the experiment are shown in Figure 4.

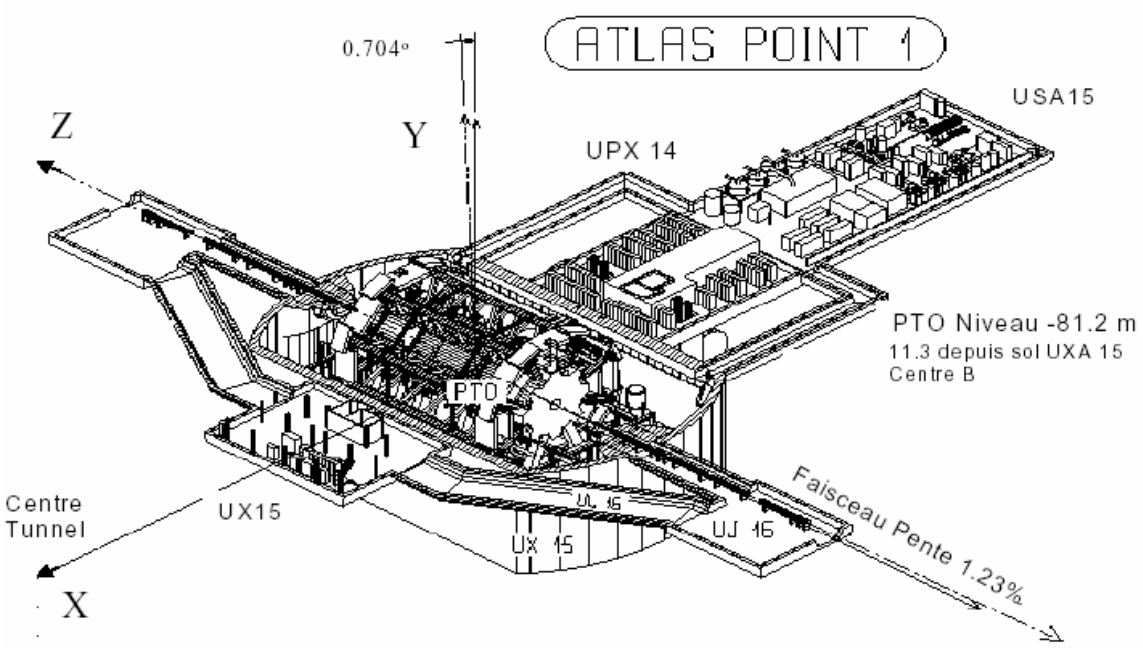

Figure 4 Right-handed co-ordinate system of the ATLAS Detector.

The detector is optimized for a wide range of known and hypothetical process. The observable cross-section for most of the processes is small over a large part of mass range; hence it is an important design consideration to operate at high luminosity and to maximize the detectable rates above backgrounds by high resolution measurements. The basic design criteria of the detector include the following:

- Very good electromagnetic calorimetry for electron and photon identification and measurements, complemented by full-coverage hadronic calorimetry for accurate jet and missing transverse energy (E_{Tmiss}) measurements.
- High-precision muon measurements, with the capability to guarantee accurate measurements at the highest luminosity using the external muon spectrometer alone.
- Efficient tracking at high luminosity for high-p_T[*] lepton-momentum measurements, electron and photon identification, τ-lepton and heavy-flavour identification, and full event reconstruction capability at lower luminosity.

[*] The transverse momentum of the particles p_T is defined as the component of the momentum perpendicular to the LHC beam axis.

- Large acceptance in pseudo-rapidity $\eta^{\dagger}$ with almost full azimuthal angle ϕ coverage everywhere. The azimuthal angle is measured around the beam axis.
- Triggering and measurements of particles at low-p_T thresholds, providing high efficiencies for most physics processes of interest at LHC.

ATLAS is characterized by two different magnetic field systems required for particle identification and momentum measurements. A super-conducting solenoid, providing a magnetic field of 2 T, will be installed around the Inner Detector cavity, whereas a large super-conducting air-core toroid system, providing a magnetic field of 1.5 T, will be arranged outside the calorimetry. The latter gives a high-resolution, large acceptance and robust muon spectrometer with excellent stand-alone capabilities. The total weight of the detector is ~7000 Tons, mainly due to the calorimetry system. The inner detector (ID) is contained within a cylinder of length 7 m and a radius of 1.15 m. The ID is designed to reconstruct tracks and decay vertices in any event with high efficiency. Using additional information from the calorimeter and muon systems, the inner detector also contributes to electron, photon, and muon identification, and supplies extra signatures for short-lived particle decay vertices. Pattern recognition, momentum and vertex measurements, and electron identification are achieved with a combination of discrete high-resolution semiconductor pixel and strip detectors in the inner part of the tracking volume, and continuous straw tube tracking detectors with transition radiation capability in its outer part.

Highly granular liquid-argon (LiAr) electromagnetic (EM) sampling calorimetry, with excellent performance in terms of energy and position resolution, covers the pseudorapidity range $|\eta|<3.2$. In the end-caps, the LiAr technology is also used for the hadronic calorimeters, which share the cryostats with the EM end-caps. The same cryostats also house the special LiAr forward calorimeters which extend the pseudorapidity coverage to $|\eta|<4.9$. The LiAr calorimetry is contained in a cylinder

---

† The pseudo-rapidity of the particles from the interaction vertex is defined as: $\eta = -\log\tan\frac{\theta}{2}$ where θ is the polar angle measured from the positive z-axis.

with an outer radius of 2.2 m and extends longitudinally to ±6.6 m along the beam axis.

The bulk of the hadronic calorimetry is provided by a novel scintillating-tile calorimeter, which is separated into a large barrel and two smaller extended barrel cylinders, one on each side of the barrel. The outer radius of the scintillating-tile calorimeter is 4.25 m and its half length is 6.10 m. The overall calorimeter system provides the very good jet and E_{Tmiss} (transverse missing energy) performance of the detector. The calorimeter is surrounded by the muon spectrometer. The air-core toroid system, with a long barrel and two inserted end-cap magnets, generates a large magnetic field volume with strong bending power within a light and open structure. Multiple-scattering effects are thereby minimized, and excellent muon momentum resolution is achieved with three stations of high-precision tracking chambers. The muon instrumentation also includes trigger chambers with very fast time response as a key component. The muon spectrometer defines the overall dimensions of the ATLAS detector. The outer chambers of the barrel are at a radius of about 11 m. The half-length of the barrel toroid coils is 12.5 m, and the third layer of the forward muon chambers, mounted on the cavern wall, is located about 23 m from the interaction point.

This short description of the ATLAS detector still gives an idea of the complexity for the high technological requirements that modern high energy physics experiments have to face. These experiments require a large number of scientific institutes (for ATLAS ~ 140 institutes counting more than 1500 between physicist and engineers) and before they start they need a wide program of R&D to provide the technological knowledge to build the experiment and run it efficiently during the period of data-taking.

In the area of the inner tracker where a large amount of silicon detectors is used an aspect of great concern is the capability of these devices to stand the high radiation doses foreseen for this region which is the closest to the interaction point. In fact high luminosity and high interaction energy at the LHC will result in extremely high interaction rates: at the maximum luminosity about 30 primary interactions will occur in every bunch crossing, producing several hundreds of secondary particles. This will result in a very high radiation dose at the level of the inner tracker. In the ID,

at Semiconductor Tracker (SCT) radii radiation doses are calculated to reach $1.5*10^{13}$ cm^{-2} 1 MeV equivalent neutrons per year [8] as shown in Figure 5.

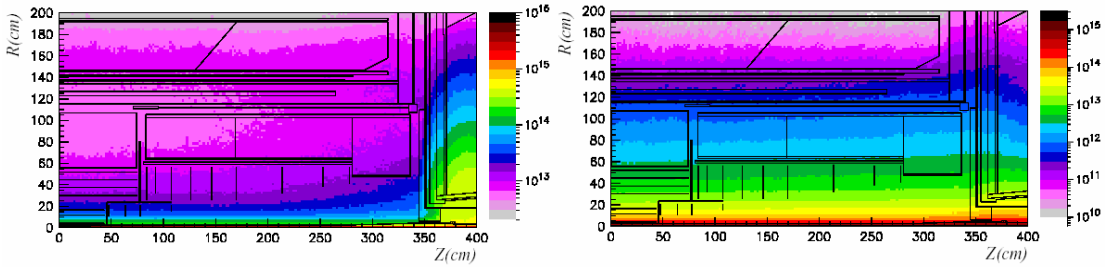

Figure 5 Flux in inner detector cavity of 1 MeV equivalent neutrons (left) and charged hadrons (right) per cm^2 per year [8].

This concern has created the need for a deep study of the damage caused by radiation in silicon devices. The damage appearing at atomic level has severe consequences on macroscopic properties resulting in a degradation of the performance of these devices. These have been widely studied for silicon detector with simple pad geometry [9]. Nevertheless the detectors used in real experiments have generally strip-like or pixel-like symmetry and the generalization to these cases from pad detector studies is not straightforward. This thesis, mainly developed within the ATLAS experiment, will present a detailed investigation of how the signal readout from microstrip detector will evolve with absorbed dose via numerical simulations and experimental investigation. Particular attention will be given to the geometry of the microstrip detectors in the ATLAS Semiconductor Tracker.

Furthermore, during these years of preparation for the LHC, a lot of effort has been invested in attempts to conceive possible alternatives to improve the radiation hardness at the tracker level [10] [11] [12]. A part of this thesis work is also devoted to these studies. This part has been developed within the CERN Collaboration RD39 [10], whose aim is the development of radiation silicon detectors hardened by low temperature operation.

1.5 Outline of the thesis

The main objective of this thesis is to study the capability of silicon detectors to stand high radiation doses of the order expected in the ATLAS SCT.

In the next chapter a general overview of silicon detectors will be given. The main features of semiconductors and the working principle of these devices will be described.

Chapter 3 will present first a description of the radiation damage in silicon and the related degradation of silicon detectors properties and then how to remedy the loss of charge collection by low temperature operation. The analysis of data collected during a test beam performed with silicon detectors irradiated at low temperature will be also presented.

In Chapter 4 a package of numerical simulations of silicon detectors realised during this PhD thesis will be presented. These simulations are aimed at understanding the performance of silicon detectors at different absorbed doses for comparison with experimental results presented in following chapters.

Chapter 5 will present a fully automated experimental setup developed during this thesis to perform Transient Current/Charge Technique for a segmented detector. A first discussion on the evolution with the dose of the depletion voltage is also presented at the end of the chapter. An extended range of TC/ChT measurements with their discussion will be presented in Chapter 6. Finally a summary of the main achievement of this thesis will be presented in Chapter 7.

1.6 References

[1] W. Weinberg, Phys. Rev. Lett. 19, 1264 (1967);
S.L. Glashow, Nucl. Phys. B 22, 579 (1961)

[2] F. Abe, et al. (CDF collaboration), Phys. Rev. Lett. 74, 2626 (1995); S. Abachi, et al. (DØ collaboration), Phys. Rev. Lett. 74, 2632 (1995).

[3] K. Kunszt, *Bread and Butter Standard Model*, lectures given at ISSP, 37th Course, Basic and Highlights of Fundamental Physics, Erice, Italy 29 Aug. -7Sept. 1999

[4] J. Wess, J. Bagger, *Supersymmetry and Supergravity*, Princeton University Press NJ; 2nd Edition, 1992

[5] The LHC Conceptual Design Report - The Yellow Book, CERN/AC/95-05(LHC) (1995)

[6] ATLAS Technical Proposal for a General-Purpose pp Experiment at the Large Hadron Collider at CERN, CERN/LHCC/94-43 (1994)

[7] An index of all the ATLAS TDRs can be found for ex. on the ATLAS web page at http://atlas.web.cern.ch/Atlas/internal/tdr.html

[8] ATLAS Inner Detector Technical Design Report Vol.1, ATLAS TDR 4, CERN/LHCC 97-16 (1997);

[9] 3rd RD48 STATUS REPORT CERN LHCC 2000-009, LEB Status Report/RD48, 31 December 1999

[10] RD39 Status Report, CERN-LHCC-2000-010

[11] RD42 Status Report, CERN-LHCC-2002-010 ; LHCC-Status-Report-RD-42 ; LHCC-RD-001

[12] RD50 Proposal, CERN, LHCC 2002-003 / P6– 12, 15 Feb.

2 Silicon Detectors in High Energy Physics

Silicon detectors are now widely used in High Energy Physics. Their basic working principle is the following: high energy particles crossing the detector release a certain amount of energy ionizing the detector crystal where an electric field is present. The free charge carriers generated in the ionization process drift due to the electric field and are collected at the detector electrodes. This gives rise to a signal that is detected by the readout electronics indicating the transit of the crossing particles. This basic principle will be fully explained in this chapter together with the main features that make possible the realisation of tracking detectors with silicon.

2.1 Energy loss of high energy particles in silicon detectors

A charged particle that crosses a semiconductor continuously loses a part of its energy through various types of interaction. The predominant one is the electromagnetic with the electrons of the atoms in the lattice. As a consequence electrons from the valence band are excited to the conduction band (electron-hole pairs generation), ionizing the lattice [1].

The loss of energy dE for a charged particle that crosses a medium for a distance dx is given by the formula of Bethe and Bloch [2].

$$-\frac{dE}{dx} = K\, z^2 \frac{Z}{A}\frac{1}{\beta^2}\left[\frac{1}{2}\ln\frac{2m_e c^2\beta^2\gamma^2 U_{\max}}{I^2} - \beta^2 - \frac{\delta}{2}\right] \qquad (1)$$

The parameters of the equation (1) are contained in the Table 1.

Variable	Value	Units	Definition
z			charge of the incident particle
Z	Si: 14		atomic number of the detector
A	Si: 28.0855		atomic mass of the detector
β	v/c		Relative speed (in respect to light in vacuum)
γ	$1/\sqrt{1-\beta^2}$		
U_{max}			Maximum kinetic energy transferred to a free electron in an interaction
I	(10±1) Z Si: 172	eV	Mean excitation energy (for Z>8 only)
K	$4\pi N_A r_e^2 m_e c^2$ 0.307	$MeVg^{-1}\ cm^2$	

Table 1 Definition of parameters in the equation (1)

The parameter δ corrects the effects of the density, i.e. that which is due to the electric field of the incident particles modifying the electric field of the lattice in the semiconductor. This weakens the forthcoming interactions, reducing the transferred

energy. The effects of the density become relevant especially for ultra relativistic particles. A general expression for δ is given in [3].

The loss of energy in the equation (1) shows only a minimal dependence on the mass of the incident particles, through the maximum transferred energy U_{max}. Therefore, in applications relative to high energy physics a reasonable approximation is that dE/dx depends only on the βγ of the incident particle. Figure 1 shows the loss of energy for three different cases: without considering corrections due to density effect, considering this effect and assuming a loss of energy restricted to 0.5 MeV due to the finite dimension of the detector.

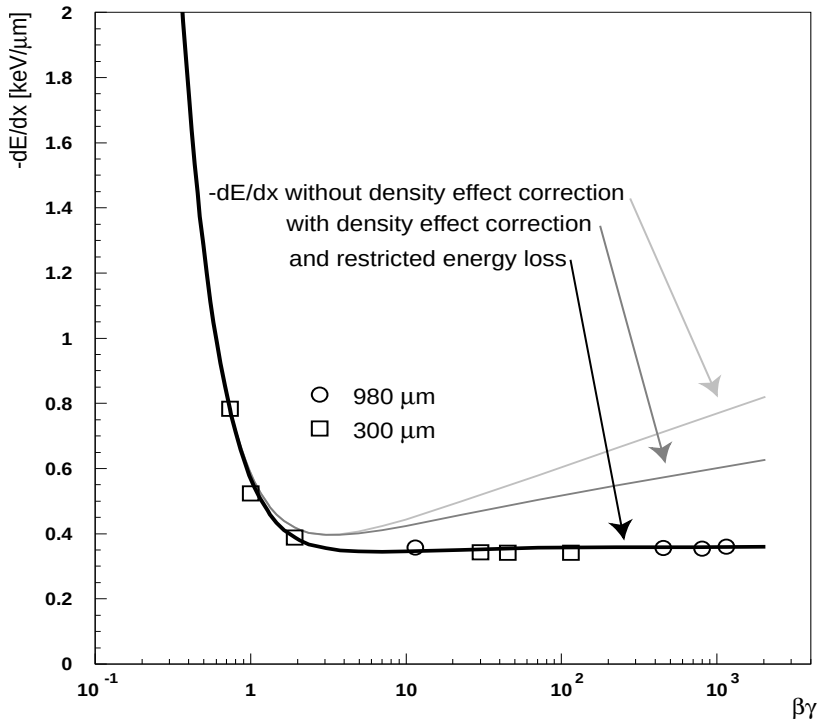

Figure 1 Mean energy deposition in silicon as a function of particle energy. The density effect and the restriction of the energy loss to 0.5 MeV become important at high energies. The circular data were taken with a 980 μm thick detector [4]. The rectangular data are calculated from measurements of the most probable energy deposited in a 300 μm thick detector [1]

Figure 1 shows that for particles with $\beta\gamma$ bigger than 3, the mean loss of energy can be considered constant. Particles crossing the medium releasing such minimum energy are called mips (*minimum ionizing particles*). The mean energy released following the equation (1) is equivalent to the most probable energy only for thicker detectors[1]. For such detectors such energy is distributed following Gauss' Law as can be shown by the Central Limit Theorem for a large number of events [6]. In thin detectors the Central Limit Theorem is no longer valid because the assumption of large number of event (i.e. the number of interactions of the crossing particle with the matter) does not hold anymore and the distribution of energy loss becomes very complicated to calculate. The possibility of large energy transfer in a single interaction, although rare, adds a long tail to the high energy side of the energy-loss probability distribution giving it a skewed asymmetric form with the most probable transferred energy smaller than the mean one. All the detectors considered in this thesis can be considered thin. Landau has formulated a theory for the loss of energy in thin detectors [7]. In a semiconductor the quantity of energy released in the material by an ionizing particle can be converted to a number of generated electron-hole pairs. The conversion is given by the amount of energy ε_c needed to generate an electron-hole pair. For silicon this energy is 3.6 eV at 300 K, where only one third of it is necessary to promote an electron to the conduction band and the rest is absorbed by the medium in reticular excitations. Figure 2 shows Landau distribution for a silicon detector 300 μm and 150 μm thick, numerically calculated. For mips that lose an average energy of 390 eV/μm in silicon, the most probable value of generated pairs in a 300 μm thick detector is about 24000.

[1] The thickness of a detector is defined with respect to the material radiation length that in silicon is 9.4 cm [5].

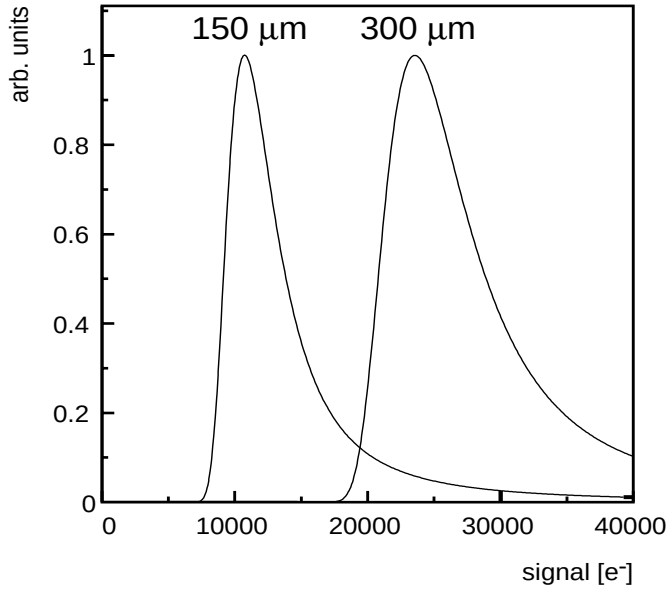

Figure 2 Landau distribution computed numerically for a 300 μm and a 150 μm thick silicon detector. The most probable values are 24000 and 11000 electrons, respectively.

This low electron-hole pair creation energy, together with the high drift velocity of the charge carriers, makes silicon an ideal material for tracking applications in a high interaction rate environment. In order to separate the carriers and generate a drift motion in a silicon bulk that would give rise to a detectable signal, an electric field has to be present. The description of how an electric field can be generated in a semiconductor crystal is the subject of the next section.

2.2 Basic features of semiconductor physics

Silicon, like all semiconductor materials, is organised in a periodic atomic disposition whose regularity give rise to the energetic structure in bands for the electrons belonging to the outer atomic shells. Due to their fermionic nature, in thermal equilibrium the probability that an electron occupies an electronic state with energy E is given by the Fermi-Dirac distribution function:

$$F(E) = \frac{1}{1 + e^{-(E - E_f)/k_B T}} \qquad (2)$$

For non degenerate semiconductors the population of electrons in the conduction band *n(T)* and the population of holes[2] in the valence band *p(T)* is[3] [8]:

$$n(T) = N_c(T) e^{-(E_c - E_f)/k_B T} \qquad (3)$$

$$p(T) = P_v(T) e^{-(E_f - Ev)/k_B T} \qquad (4)$$

where E_f is the Fermi level, E_c is lower limit of the conduction band, E_v is the upper limit of the valence band, T is the temperature and k_B is the Boltzman constant. N_c and P_v are respectively the level densities in the conduction and the valence band. Formally:

$$N_c(T), P_v(T) = \frac{1}{4}\left(\frac{2 m_{c,v} k_B T}{\pi \hbar^2}\right)^{3/2} \qquad (5)$$

where m_c is the determinant of the conduction band effective mass tensor and m_v is similarly defined.

The conduction band electrons come from the formerly occupied valence band levels, leaving holes behind them. Therefore the number of conduction band electrons is the same as the valence band holes[4] for charge neutrality:

$$n(T) = p(T) = n_i(T) \qquad (6)$$

From the equations *(2)*, *(3)* and *(4)*:

---

[2]The *holes* are missing electrons in the valence band. In semiconductors partially filled energetic bands guarantee the electric conduction.

[3] The expression derives from a simplification, which is valid when $(E_c - E_f), (E_f - E_v) >> k_B T$.

[4] This is true only in the case of pure silicon (*intrinsic* silicon), as will be discussed next.

$$n_i(T) = \sqrt{n(T)p(T)} = \left[N_c(T)P_v(T)\right]^{1/2} e^{-Eg/2k_BT} \qquad (7)$$

Where E_g is the energetic gap between the conduction and the valence band. The Fermi level can then be calculated as:

$$E_f = \frac{E_C + E_V}{2} + \frac{k_B T}{2}\ln\left(\frac{N_V}{N_C}\right) = \frac{E_C + E_V}{2} + \frac{3k_B T}{4}\ln\left(\frac{m_v}{m_c}\right) \qquad (8)$$

Here we see that at 0 K the Fermi level stands right in the middle of the bandgap and $\ln\left(\frac{m_v}{m_c}\right)$ being of the order of the unity, will rise within a k_BT at higher temperatures.

2.2.1 Crystal defects and impurities

In nature semiconductors also present defects and atomic impurities in the lattice. The *point defect* is a single disarrangement of reticular atoms and/or a reticular impurity. Such defects and impurities deform the band structure energy generating discrete energy levels. When these energy levels are in the forbidden gap they are generally classified as *acceptors* or *donors* if their electric state is respectively negative or neutral when an electron occupies them[5]. In particular *donor* impurities are atoms that have a higher chemical valence than the atoms making up the pure (host) material, while *acceptors* have a lower chemical valence. In thermal equilibrium the Fermi level, whose position in the bandgap depends on the type of material (resistivity) and temperature, rules the electric state of the defects. If the defects are ionised at room temperature they are in general called *shallow levels* (i.e. the donor (acceptor) level stands between the Fermi level and the conduction (valence) band). In the other case, when the acceptors or donors are filled respectively with a hole or an electron, they are called *deep levels*.

When impurities constitute the main source of charge carriers, one speaks of an *extrinsic semiconductor*. Hence the semiconductor crystal will have n-type conductivity

[5] Some defects can also present more than one level in the band gap. This behaviour is called *amphoteric*.

if the presence of donor impurities is higher, or p-type conductivity in the opposite situation.

In both of the cases described above, given the presence of impurities, the Fermi level is displaced from the centre of the mid gap, moving towards the valence band in the p-type crystals or towards the conductive band if the presence of the donors prevails on the acceptors.

Calling n_i the common value for electrons and hole respectively in conduction and valence band in the intrinsic semiconductor, for an extrinsic one the validity of the following relation can be shown:

$$n(T), p(T) = n_i e^{\pm(E_f - E_i)/k_B T} \qquad (9)$$

where E_f and E_i are respectively the Fermi level in the extrinsic and intrinsic semiconductor. From the eqn. (9) derives that:

$$n_i^{\,2}(T) = n(T)\,p(T) \qquad (10)$$

which is in general called the **mass-action law**.

2.2.2 Shockley-Read-Hall statistics

The population for any level of energy E at the thermal equilibrium is given by $N_d \cdot F(E_d)$ where $F(E_d)$ is defined in equation *(2)* and N_d is the density of corresponding defects in the space. For E_d in the forbidden gap this result comes out of the continuous interaction of the level itself with the conductive and valence bands in processes of emission and absorption. So, from the occupation of the level at equilibrium can be derived the rate of these processes that take their name from the scientists who first studied them [9] [10]. Considering a single defect level in thermal equilibrium, four competing processes will take place as shown in Figure 3.

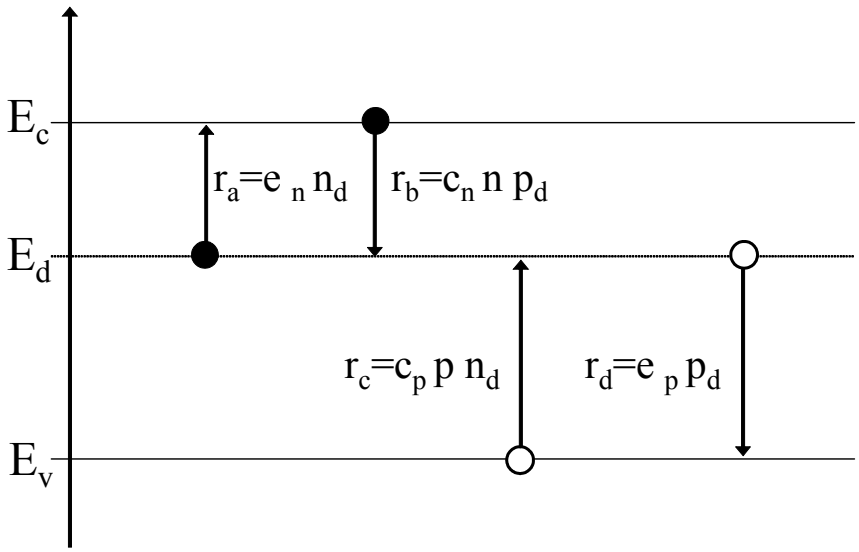

Figure 3 Schematic of the four competing processes taking place at equilibrium for a single level defect E_d: a) emission of electron into the conductive band with a rate r_a, b) capture of electrons from the conductive band with a rate r_b, c) capture of holes from the valence band with a rate r_c and d) emission of holes into the valence band with a rate r_d.

As defined in the Figure 3 the four processes taking place are:

- The emission of electrons (holes) into the conductive (valence) band with a rate r_a (r_d), proportional to the fraction of level states occupied by an electron n_d.(a hole p_d) which is:

$$n_d = N_d F(E_d) = N_d f_d \qquad (p_d = N_d(1 - F(E_d)) = N_d(1 - f_d)) \qquad (11)$$

- The capture of electrons (holes) from the conductive (valence) band with a rate r_b (r_c), proportional to the product of the fraction of the level states p_d (n_d) occupied by a hole (electron) and the density n (p) of electrons (holes) in the conduction (valence) band.

The proportional factors are the *emission* or *generation coefficient* e_n (e_p) and the *capture* or *trapping coefficient* c_n (c_p) where the last is given by the product of the carrier velocity and the capture cross section of the trap. The trapping time, i.e. the time the unoccupied defect takes to change state is given by:

$$\tau_n^c = \frac{1}{nc_n} \quad for\ donors, \quad \tau_p^c = \frac{1}{pc_p} \quad for\ acceptors \qquad (12)$$

The electron (hole) population of the conduction (valence) band being constant at thermal equilibrium, the rates of emission and capture of electrons (holes) have to be equal. This means that:

$$e_n n_d = c_n n p_d \qquad (e_p p_d = c_p p n_d) \qquad (13)$$

The equilibrium condition allows the calculation of the emission rate and the detrapping times:

$$e_n = \frac{1}{\tau_n^e} = nc_n \exp\left(\frac{E_d - E_F}{k_B T}\right) = n_1 c_n \quad for\ donors \qquad (14)$$

$$e_p = \frac{1}{\tau_p^e} = pc_p \exp\left(\frac{E_F - E_d}{k_B T}\right) = p_1 c_p \quad for\ acceptors \qquad (15)$$

where n_1 and p_1 are respectively the density of electron in the conducting band and the density of the holes in the valence band when the Fermi level is coincident with E_d. These relations are also valid when not in equilibrium if one assumes the condition of electrons (holes) in the conduction (valence) band in equilibrium with themselves and separately the trapped electrons (holes) also in reciprocal equilibrium[6]. The *generation-recombination* (G-R) *rate* for electrons (holes), that at the equilibrium is vanishing, can be expressed in terms of capture rate as:

$$U_{cn} = N_d\left[c_n n(1 - f_d) - c_n n_1 f_d\right] \qquad \left(U_{cp} = N_d\left[c_p p f_d - c_p p_1(1 - f_d)\right]\right) \quad (16)$$

[6] Two "quasi Fermi levels" characterize the condition of separated equilibrium between the electrons in the conductive band and the trapped electrons. At the equilibrium these two levels will be coincident in the system Fermi level.

An interesting case is the steady-state condition of a constant G-R rate $U = U_{cn} = U_{cp}$. From this equivalence the probability to have electrons in the level E_d is:

$$f_d = \frac{c_n n + c_p p_1}{c_n(n + n_1) + c_p(p + p_1)} \qquad (17)$$

This result allows writing the G-R rate in terms of electron and hole capture coefficients and density in the conduction and valence band:

$$U = U_{cn} = U_{cp} = \frac{N_d c_n c_p (np - n_i^2)}{\left[c_n(n + n_1) + c_p(p + p_1)\right]} \qquad (18)$$

In the previous equation n_i is the hole and electron concentration in an intrinsic sample and is given by the product $n_1 p_1$, as seen in the eqn. (10). The product np is greater than n_i^2 when generation prevails on the capture rate and viceversa.

2.3 Semiconductor junctions

In order to modify the electrical properties, a semiconductor can be enriched in impurities, through a process called *doping*, increasing the density of donor levels or acceptor levels. These processes are widely used, as they are the bases for the realisation of semiconductor devices.

2.3.1 P-n junction

When in a crystal of semiconductor the impurity concentration varies only along one direction and in a small region called the *transition region*, where at the extremities the type of conductivity is inverted, one speaks of *p-n junction*.

In the future we will consider *abrupt junction,* in which the *transition region* is so sharp that variation in impurity concentrations can be represented by a single discontinuous change in type of conductivity between the two regions of the junction. Nevertheless real junctions may be regarded as abrupt if the *transition region* in the actual doping profile is small in extent compared with the length of the junction. In the

junction the presence of a strong gradient of carriers between the two regions causes the diffusion of holes from the *p-type* region to the *n-type* region and electrons diffusing in the opposite direction. As a consequence the diffused electrons recombine with holes on the p-type region and the diffused holes capture electrons on the *n-type* side. Charge migration leaves the *p-type* region with a net negative charge and the *n-type* region with a net positive charge due to unneutralised acceptor and donor ions. This charged region, also called the *space charge region*, generates an electric field that produces a current that opposes the diffusion. At equilibrium the two currents are equal and on the border of the depleted area a *built-in voltage* appears. Given a reference system whose zero is in the junction and the positive side goes along the n-type side, the electric field and the electric potential drop across the junction can be calculated with the Poisson equation:

$$\frac{d^2V}{dx^2} = -\frac{\rho_c(x)}{\varepsilon_{Si}} \tag{19}$$

where, due to the hypothesis of abrupt junction and absence of charge carriers, the charge density is:

$$\rho_c(x) = \begin{cases} eN_d, & x_n > x > 0 \\ -eN_a, & -x_p < x < 0 \end{cases} \tag{20}$$

The potential across the junction can be seen to be:

$$V_{bi} = \frac{e}{2\varepsilon_{Si}}(x_n^2 N_d + x_p^2 N_a) \tag{21}$$

and the condition of electrical neutrality of the entire system brings us to:

$$N_a x_p = N_d x_n \tag{22}$$

So, the full extension *w* of the SCR is given by:

$$w = x_n + x_p = \left[\frac{2\varepsilon_{Si} V_{bi}}{e} \left(\frac{1}{N_d} + \frac{1}{N_a} \right) \right]^{1/2} \qquad (23)$$

For what concerns *pn* junctions used as tracking detectors the doping of one side (usually the p side) is much higher than the other ($N_a >> N_d$). Moreover in a low doped *n*-type side the acceptor concentration can be nearly the same order of magnitude as the donor concentration and the evaluation of the SCR will be given by:

$$w \approx x_n = \sqrt{\frac{2\varepsilon_{Si} V_{bi}}{eN_d}} \qquad (24)$$

It is worth stressing that N_d and N_a both represent the relative doping concentration in each junction side. For this reason one often refers to the effective doping concentration expressed as N_{eff} to indicate the doping in the junction side with lower concentration that in this case is $N_d = |N_d' - N_a'|$ with N_d' and N_a' respectively the absolute density of the donors and acceptors in the *n*-type region.

In order to extend the SCR in *pn* junctions an external voltage V with the same polarity of the built-in voltage is applied. This will increase the extension of the depleted region so that:

$$w(V) = \sqrt{\frac{2\varepsilon_{Si}(V_{bi} + V)}{eN_{eff}}} \approx \sqrt{\frac{2\varepsilon_{Si} V}{eN_{eff}}} \quad for \quad V >> V_{bi} \qquad (25)$$

Supposing that the highly doped *p*-type region has a small extension compared to the *n*-type region, to fully deplete the *pn* junction it one has to apply a voltage:

$$V_{FD} = \frac{eN_{eff} d^2}{2\varepsilon_{Si}} \qquad (26)$$

where d is the *pn* junction thickness.

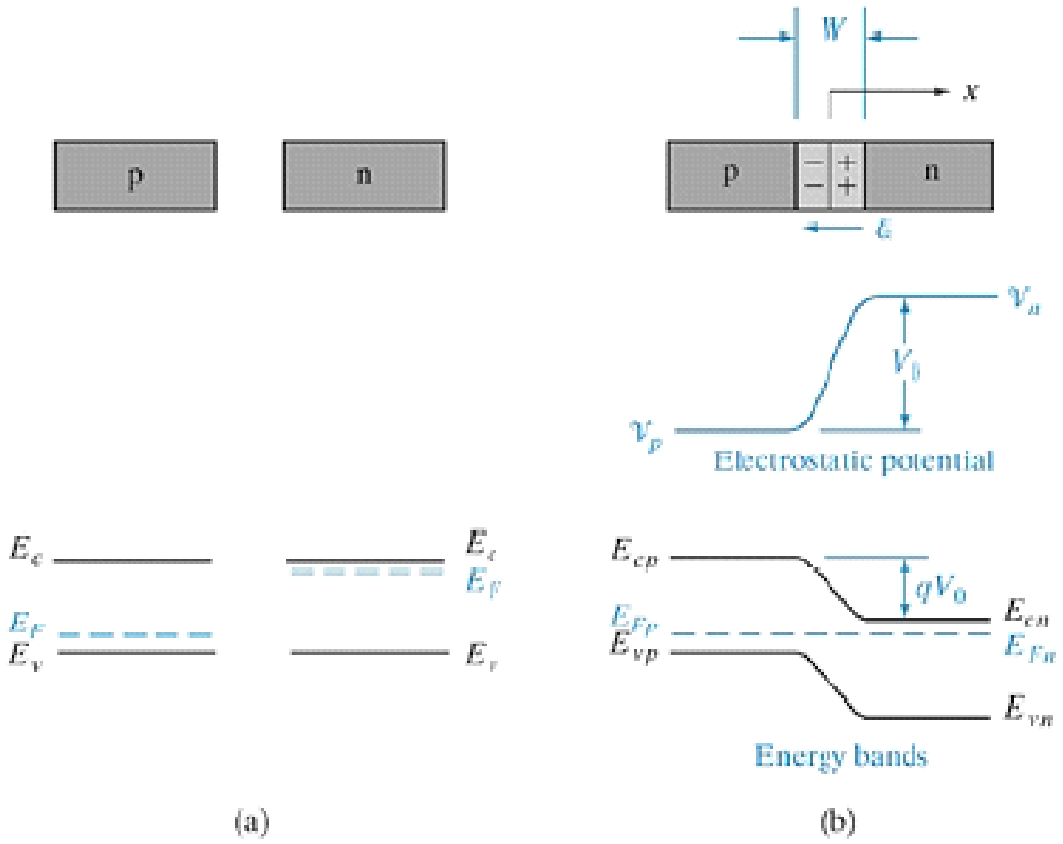

Figure 4 Non-equilibrium state of a pn junction (a), from which the establishment of thermodynamic equilibrium develops (b).

2.3.2 Metal-Semiconductor junction

When a metal is making intimate contact with a semiconductor, the Fermi level in the two materials must be coincident at thermal equilibrium. Either in the presence or in the absence of surface states on semiconductor, the effect of the contact is the appearance of a potential barrier at the interface due to a depletion layer similar to that of the one-sided (e.g., p^+-n) junction [11]. This depletion layer can be extended in the same manner as in *pn* junction by applying an external voltage.

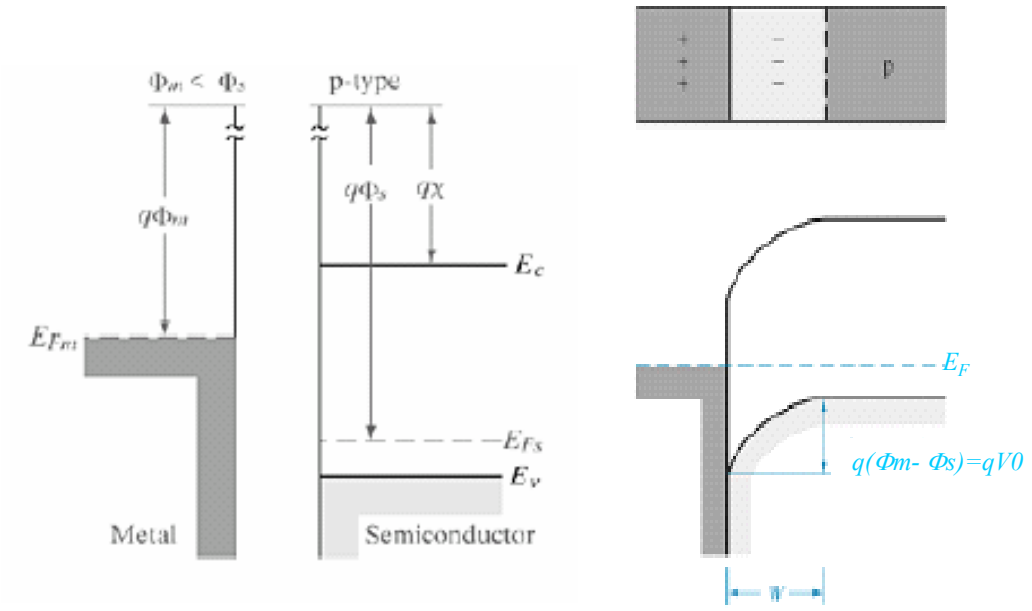

Figure 5 Band bending and depletion for metal contact on p-substrates.

In the semiconductor, an electron at a certain distance from the metal surface experiences an electrostatic attraction due to the positive charge induced on the metal surface. This effect, combined with the presence of an electric field in the depleted region gives rise to what is in general referred to as the "Schottky effect" for which a lowering of the potential barrier is experienced by the electrons flowing through the interface metal-semiconductor.

The barrier width goes all along the space charge region whose extension depends on the doping concentration. It follows that the higher is the doping the narrower is the barrier width. This fact makes possible the creation of *ohmic contacts* that play an important role as electrical contacts for semiconductor detectors.

The *ohmic contact* is realized by introducing a thin layer of highly doped semiconductor of the same type of conductivity as the bulk between the semiconductor and the metal. Due to the narrow barrier quantum tunnelling is the main current transport through the metal-semiconductor interface. This allows the necessary device current and the voltage drop across the contact is small compared to the voltage across the active

device region. A good *ohmic contact* should not degrade the device performance and have linear (or quasi-linear) voltage current characteristics.

2.3.3 Metal-Insulator-Semiconductor (MIS) structure

In order to better understand the behaviour of semiconductor detectors one has also to understand the properties of the MIS structure. This structure is often referred as the MOS (metal-oxide-semiconductor) structure since the most widely insulator used in this technology is the silicon oxide (SiO_2). In an ideal approximation of the MOS structure, at thermal equilibrium ($V_{bias}=0$) the work function for the metal and semiconductor is the same (*flat band condition*), the resistivity of the insulator is infinite hence no carrier transport appears in the insulator under dc biasing condition and under any biasing condition the only charges that can appear in the structure are those in the semiconductor and those, equal but of opposite sign, induced on the metal surface adjacent to the semiconductor.

In a very naïve vision of the structure, applying a positive bias on the metal would attract electrons in the semiconductor that accumulate in the region close to the Si-SiO_2 interface (semiconductor bands bend downward) and a positive charge distributes on the metal surface in contact with the SiO_2, otherwise for a negative bias a positive charge is accumulated at the interface (bands bend upward) with electrons at the metal interface.

This structure in silicon detectors can be used to AC couple the signal generated by radiation in the detector to the readout electronics.

A relevant property of the oxide is the presence of charge that distorts the ideal behaviour of the MOS structure. The charge in the oxide can be of different origins: *interface trapped charges* which are discrete energy levels in the silicon forbidden gap located in the Si-SiO_2 interface and able to exchange charges with silicon in short time, the *fixed oxide charge*, generally positive, located at or near the interface and are immobile under an applied electric field, *mobile ionic charge,* which is mobile within the oxide and the *oxide trapped charge* which can be created for instance by high energy particles. This basic classification is shown in the Figure 6.

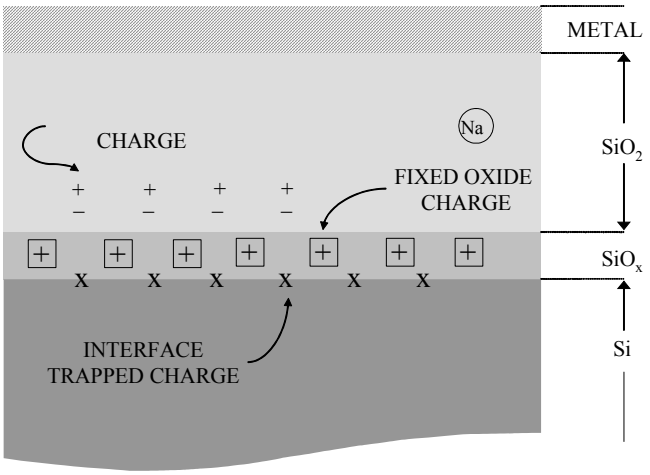

Figure 6 Different charges present in the oxide layer.

2.4 Charge carrier transport in silicon

For non-equilibrium and non-stationary conditions in uniformly doped silicon the charge carriers' concentration depends generally on the space coordinate and on time. We consider first the carrier transport in a semiconductor, with a uniform concentration of carriers, in the presence of an electric field.

In a low electric field $\vec{E}$ the motion of free carriers is due to the superposition of two effects taking place: thermal motion and electric motion. As a result the carriers drift with a velocity $\vec{v}_{n,p}$ that is for electrons and holes respectively:

$$\vec{v}_{n,p} = \mp \mu^0_{n,p} \cdot \vec{E} \qquad (27)$$

where $\mu_{n,p}$ is the mobility for the electron and the holes. From a classical Drude-like model [8] based on the collision of the carriers with the lattice the mobility can be derived as:

$$\mu_{n,p}^{0} = \frac{e\tau_{n,p}^{c}}{m_{n,p}^{*}} \qquad (28)$$

where e is the positive unitary charge, $\tau_{n,p}^{c}$ is the collision time and $m_{n,p}^{*}$ is the effective mass for electrons and holes. More precisely, the value of the mobility for low electric field ($\leq 10^3$ V/cm) is related to carrier scattering, which is affected by the presence of acoustic phonons[7] and ionized impurities. For high electric field, starting around 10^4 V/cm, the most frequent event of the scattering is the emission of optical phonons and the carriers start to acquire more energy than they have at thermal equilibrium achieving an effective temperature T_e higher than the lattice temperature. Balancing the rate at which energy transferred from the field to the carriers by an equal rate of loss of energy to the lattice one obtains that the equation *(28)* is still valid but the mobility will be [14]:

$$\mu_{n,p} = \mu_{n,p}^{0} \cdot \sqrt{\frac{T}{T_e}} \qquad (29)$$

Increasing the electric field the carrier drift velocity approaches a saturation velocity, which is of the order of 10^7 cm s^{-1}. More detailed numerical approximations of the mobility will be discussed later. Furthermore for still higher electric fields avalanche processes might become active [13].

In the presence of an appreciable gradient of free carrier density the diffusion takes place, acting in a way to restore the equilibrium values of the carrier densities. Together the drift and the diffusion can be summarised in the following equation for the carrier current densities that can be derived from Boltzmann transport theory[8].

---

[7] The acoustic phonons are the reticular excitation corresponding to non dispersive elastic waves in the crystal.

[8] For a deeper treatment of how to derive the equation (30) from the Boltzmann transport theory see for example [15].

$$\begin{cases} \vec{J}_e = -\mu_n n_c(\vec{x})\vec{E} - D_n \vec{\nabla} n_c(\vec{x}) & \textit{for electrons} \\ \vec{J}_h = \mu_p p_v(\vec{x})\vec{E} - D_p \vec{\nabla} p_v(\vec{x}) & \textit{for holes} \end{cases} \qquad (30)$$

The positive constants D_n and D_p are called *diffusion constants* and are related to the mobility by the *Einstein relations*:

$$\mu_n = \frac{eD_n}{k_B T}, \qquad \mu_p = \frac{eD_p}{k_B T} \qquad (31)$$

The Einstein relations follow directly from the fact that electrons and hole current densities must vanish at equilibrium. Out of equilibrium these relations are extended empirically.

The gradient of the carrier current density and the time derivative of the carrier density are related together for continuity. Nevertheless, as previously seen, a conduction band electron and a valence band hole can be generated by the thermal excitation of an electron out of the valence band and carrier numbers are not conserved. Hence the continuity equation is stated as following:

$$\frac{\partial n}{\partial t} = U_{cn} - \vec{\nabla} \cdot \vec{J}_e \qquad (32)$$

$$\frac{\partial p}{\partial t} = U_{cp} - \vec{\nabla} \cdot \vec{J}_h \qquad (33)$$

where U_{cn} and U_{cp} are respectively the *generation*/ *recombination* rates for electrons and holes derived from the Shockley-Read-Hall statistics. These rates act to restore thermal equilibrium when the carrier densities deviate from their equilibrium values. In regions where n and p exceed their equilibrium values, recombination occurs faster than generation, leading to a decrease in the carrier densities, while in regions where they fall short of their equilibrium values, generation occurs faster than recombination.

In the case of non-equilibrium but stationary conditions, with the terms U_{cn} and U_{cp} equal (see equation *(18)*), interesting cases can be analyzed. In particular one can consider a depleted *pn* junction where at the end of the *n*-side pairs are generated (for example by a light pulse as we will see in a following chapter). In case of low generation there will be:

$$p = p_0 + \delta p \qquad (34)$$

and the lifetime can be expressed as:

$$\tau = \frac{\delta p}{U} \qquad (35)$$

An interesting application of the continuity equation is given by the case in which localised pulses generate excess carriers in a semiconductor. In this case the transport equation after the pulse for holes is:

$$\frac{\partial p}{\partial t} = -\frac{p - p^0}{\tau} - \mu_p \frac{\partial}{\partial x}\left(p \cdot \vec{E}\right) + D_p \frac{\partial^2}{\partial x^2} p \qquad (36)$$

In the simpler case of electric field slowly varying in *x* the solution of the transport equation for the holes with the boundary condition of $p(0,0) = p_0 + \delta p = p_0 + N\delta(t)\delta(x)$ due to the charge generation by the pulse is given by:

$$p(x,t) = \frac{N}{\sqrt{4\pi D_p t}} \exp\left(-\frac{(\vec{x} - \mu_p \vec{E} t)^2}{4 D_p t} - \frac{t}{\tau} \right) + p^0 \qquad (37)$$

where *N* is the density of pairs generated.

Thus the whole package of holes moves away from the injection, diffusing and recombining, going towards the negative end of the sample with drift velocity $\mu_p \vec{E}$. Similar considerations can be made for the electrons.

2.5 Position Sensitive Devices

Semiconductor detectors, and especially silicon detectors, are largely used in high-energy physics experiments for high-precision position measurements. The advanced technology in the fabrication of these structures and their intrinsic properties discussed before makes them an unbeatable device for this purpose. The technology itself has gained a lot from the great efforts made in the field of silicon processing for electronics and nowadays allows a high segmentation for finer tracking. In these devices the basic structure is the *p-n* junction operated in reverse bias. Depending of their particular purpose, they can be prepared in different geometries. In the following, the most relevant geometries for the thesis work will be described.

2.5.1 Single Pad Detectors

The single pad detector is a simple planar *p-n* junction structure. The junction consists of a highly doped shallow p^+ region on a very low-doped n^- substrate and a backside of a highly doped n^+ layer. While the strong doping of the p^+ region gives a space charge region extending through all the substrate, the n^+ allows a good ohmic contact and prevents breakdown when operated in over depleted mode. The readout scheme for this device is in general *DC coupling*, i.e. the highly doped p^+ region is directly connected to its metallic contact and to the readout amplifier. Typical dimensions of the pad detector surface are 1cm*1cm and the thickness is of the order of hundreds of microns. This type of device, rather than being used for particle positioning, presents a geometry that is very convenient for studies of the material properties and is widely used for photodiodes or spectroscopic purposes.

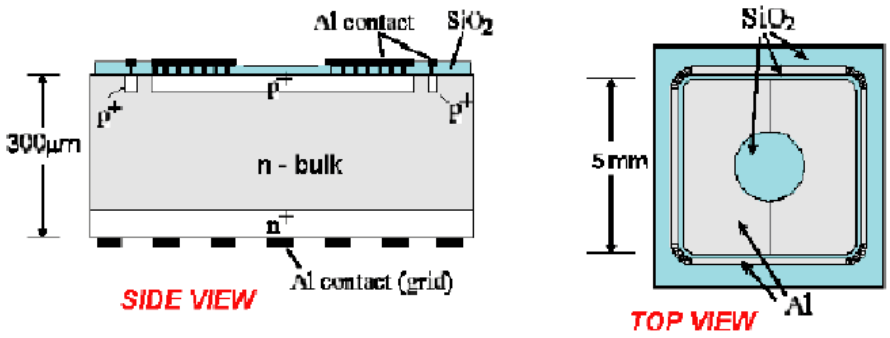

Figure 7 Schematic view of a pad detector.

2.5.2 Microstrip Detectors

Microstrip detector geometry is based on an array of regularly arranged parallel p-n junctions. Here parallel strips of p^+ implants replace the planar p^+ implantation on an n bulk present in a single pad detector. Typically, their width is of the order of a few tens of microns and their distance of less than one hundred microns. Each of these strips (or a part of them) can be connected to a separate read out channel. This geometry has been developed to measure the position of single particles incident or traversing the detector. The basic working principle is the following: for each particle crossing such a detector its position is given by the strip associated to the read out channel that carries the signal.

Microstrip detectors are frequently *AC coupled.* The advantage is that the dark current of the single junctions associated with each strip is not directly fed into the amplifier. In fact, as the dark current for each single junction can be different, in a *DC coupling* scheme, large pedestal variation might appear. Furthermore, if the dark current grows a lot during the operation, it can lead to the saturation of the electronics. In *AC coupling* a capacitor is introduced between the p^+ strip and the metallisation that is in direct contact with the readout electronics. This capacitor is actually given by an insulating layer of silicon dioxide underneath the strip metallisation.

To ensure equal potential for the different strips, each of them is connected via a polycrystalline silicon resistor to a common line of p^+ implant that is grounded and runs across all the strips on one side of the detectors.

The rear side of the detector has a layer of n^+ implant to allow the ohmic contact with an aluminised back electrode. An eventual segmentation of the n^+ layer into strips with a tilt respect to the p^+ strips can be used to determine the second co-ordinate avoiding multiple scattering. However, manufacturing process almost doubles the cost of such a device with respect to the one with a single segmented side.

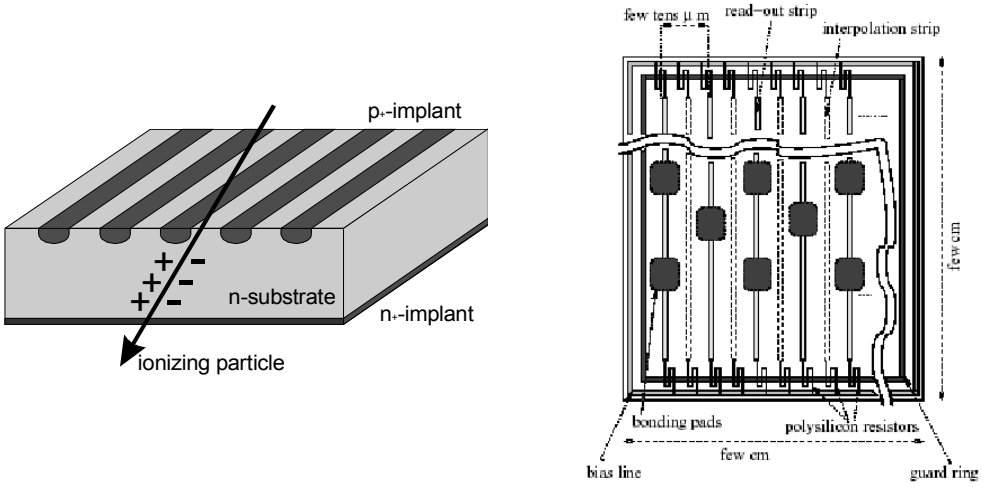

Figure 8 Schematic of the working principle (left) and some detail on the segmentation of a microstrip detector (right).

Depletion voltage in microstrip detectors

As a consequence of the finite pitch *p* and width *w* of a single side strip detector, the electric field appearing under reverse bias changes from the one in planar geometry. In fact the equi-potential lines encircle the strips and become parallel to the surface only at a depth of about the pitch *p*. Hence with respect to the planar geometry, for a given thickness *d,* the full depletion voltage increases to [16]:

$$V_{fd} = V_{fd}^0 \left[1 + 2\frac{p}{d} f\left(\frac{w}{p}\right) \right] \qquad (38)$$

where V_{fd}^{0} if the full depletion voltage for a pad detector with equal resistivity and f is an empirical function whose behaviour is shown in the Figure 9

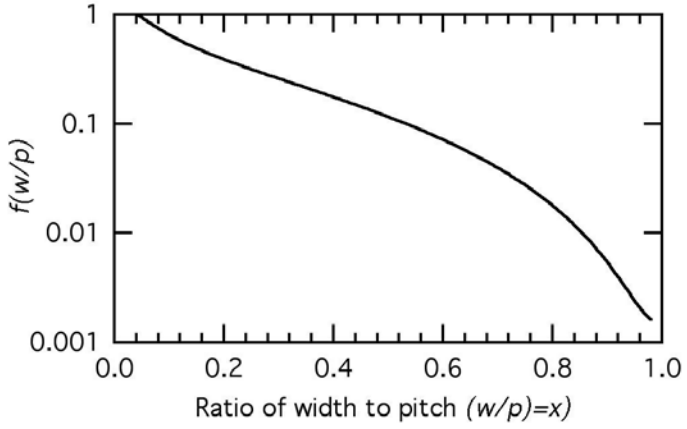

Figure 9 Behaviour of the empirical function f(w/p).

2.6 Signal generation in silicon detectors

The charge generated in silicon detectors by impinging radiation drifts due to the electric field, inducing mirror charge on the electrodes. The evolution of signal can be measured by adequate electronics. The theoretical computation of this signal is not trivial especially in cases like the microstrip detector where the charge generated is collected by a system of multi-electrodes. For this purpose one has to use the Gauss identity for which, given a system of conductors, two different electrical states are correlated. For any state each electrode i is characterised by its charge q_i and potential V_i, and the Gauss identity is:

$$\sum_i q_i V_i' = \sum_i q_i' V_i \qquad (39)$$

where the non-primed quantities and primed ones are associated to two different states of the multi-electrode system.

If we consider in the vacuum a network of three electrodes *a*, *b*, and *c* and a point-like charge *q* that can itself be considered as a small electrode positioned where the charge is, we can calculate the charge induced on each single electrode. Let's consider the electric state where the three electrodes are grounded and a positive charge away from them is at a certain potential and a state where the electrode associated to the point-like charge is not carrying any charge, the electrode *a* is at a fixed potential V_a' and the others are all grounded. Solving the Gauss identity for these two states we have:

$$qV_q' + Q_a V_a' = 0 \qquad (40)$$

Hence the charge induced by *q* on the electrode *a* when all electrodes are grounded is:

$$Q_a = -q\frac{V_q'}{V_a'} \qquad (41)$$

The current induced on the electrode *a* is obtained deriving Q_a respect to time:

$$I_a = \frac{dQ_a}{dt} = -q\frac{dV_w}{dt} \qquad \text{with} \qquad V_w = \left(\frac{V_q'}{V_a'}\right) \qquad (42)$$

$$I_a = -q\frac{dV_w}{d\vec{r}_q}\cdot\frac{d\vec{r}_q}{dt} = -q\vec{\nabla}V_w\cdot\vec{v}_q \qquad (43)$$

where $d\vec{r}_q$ is the elementary displacement of the charge *q* and $\vec{v}_q$ is its velocity.

This result is also known as Ramo's theorem [17] [18]. Generally, one refers to $-\vec{\nabla}V_w$ as the *weighting field* $\vec{E}_w$ and to V_w as the *weighting potential* and is a measure of the electrostatic coupling in the electrodes network. Its computation is obtained solving the Laplace equation in space and deriving the boundary conditions from its definition:

$$V_w = \frac{V_i'}{V_a'} = \begin{cases} 1 & i = a \\ 0 & i \neq a \end{cases} \qquad (44)$$

So far we have been considering the case of a system of electrodes in the vacuum. Nevertheless a radiation silicon detector is composed of a collection of electrodes surrounding a dielectric and, when operated, presents a fixed space charge. As has been demonstrated in [19] the dielectric properties and the fixed space charge do not change the charge induced on the electrodes and the equation (41) is still applicable. Furthermore, in a silicon crystal in presence of an electric field the motion law is given by *(27)*, where the velocity depends linearly on the electric field. Summarising, in silicon detectors, where the readout electrodes are connected to low impedance amplifiers, the evaluation of their output current at a given electrode requires:

- The knowledge of the initial distribution of electrons and holes generated by the ionising radiation.
- The evaluation of the law of motion for the free carriers in the electric field generated by electrodes biasing and the space charge.
- The evaluation of the contribution of every generated charge in motion through the weighting field $\vec{E}_w$.

If we are interested only in the total induced charge and not in the waveforms for the single generated charge we obtain from *(44)*:

$$Q_a = \int I_a dt = -q \int_{r_{p0}}^{r_{p1}} \vec{\nabla} V_w \cdot d\vec{r}_p = q\left[V_w\left(\vec{r}_{p1}\right) - V_w\left(\vec{r}_{p0}\right)\right] \qquad (45)$$

The induced charge is simply given by the difference in the weighting potentials between any two positions of the moving charge.

2.6.1 Signal generation in a silicon pad detector

When a *mip* transits a silicon detector as we have seen before it generates electron-hole pairs uniformly distributed along the particle track. The signal generated in the detector is due to the contribution of each of these pairs. For pad detectors the simple

geometry allows an analytical calculation of the current and the charge induced on the electrodes. In fact, for the two parallel electrodes with lateral dimensions much larger than the detector thickness, *d*, the weighting field calculation has a simple solution, which is: $E_w = -1/d$. It follows that for a single generated pair the current induction problem is solved in one dimension with:

$$I_{e,h}(t) = -\frac{q_{e,h}}{d} v_{e,h}(t) \qquad (46)$$

Consider such a device whose bulk has a low concentration of donors N_D and a highly p^+ doped layer over one side of the bulk. Let's suppose we reverse bias the detector with $V \geq V_{fd}$ where V_{fd} is the full depletion voltage. If we consider the junction along the x direction with the origin in the junction itself, then the electric field in the sensor is:

$$E(x) = -\frac{2V_{fd}}{d^2}(d - x) - \frac{V - V_{fd}}{d} = ax - b \qquad (47)$$

where *d* is the detector thickness.

Inside the detector the electric field lines are straight and directed normally from the n^+ to the p^+ layer. In the uniformly ionized track due to a mip particle crossing the detector, holes follow the field lines while the electrons move in the opposite direction. Considering a pair of carriers *e*, *h* generated at the point x_0, assuming the mobility constant, their motion equation from (27) is:

$$x_{e,h} = \frac{b}{a} + \left(x_0 - \frac{b}{a} \right) \exp(\mp \mu_{e,h} a t) \qquad (48)$$

and their velocity is:

$$v_{e,h} = \mp \mu_{e,h} a \left(x_0 - \frac{b}{a} \right) \exp(\mp \mu_{e,h} a t) \qquad (49)$$

The collection time for *e*, *h* is the time $\tau_{ce,ch}$ they need to reach the electrodes and is:

$$\tau_{ce} = \frac{1}{a\mu_e}\log\left(\frac{ax_0 - b}{ad - b}\right) = \frac{d^2}{2\mu_e V_{fd}}\log\left(\frac{V + V_{fd}\left(1 - \frac{2x_0}{d}\right)}{V - V_{fd}}\right) \qquad (50)$$

$$\tau_{ch} = \frac{1}{a\mu_h}\log\left(\frac{b}{b - ax_0}\right) = \frac{d^2}{2\mu_e V_{fd}}\log\left(\frac{V + V_{fd}}{V - V_{fd}\left(1 - \frac{2x_0}{d}\right)}\right) \qquad (51)$$

Hence, the higher the applied bias the faster the charge collection.

The charge induced on the electrodes by the pair is:

$$Q_{e,h} = -\frac{e}{ad}(ax_0 - b)\left[\exp\left(\mp\mu_{e,h}at\right) - 1\right] \qquad 0 \le t \le \tau_{ce,ch} \qquad (52)$$

and the current:

$$I_{e,h} = \pm\mu_{e,h}a\frac{e}{ad}(ax_0 - b)\exp\left(\mp\mu_{e,h}at\right) \qquad 0 \le t \le \tau_{ce,ch} \qquad (53)$$

At the end of the drifting the charge induced on the electrode is

$$Q = Q_e + Q_h = -\frac{e(d - x_0)}{d} - \frac{ex_0}{d} = -e \qquad (54)$$

The sum of the final values of Q_e and Q_h gives the unitary electron charge.

2.7 References

[1] H. Bichsel, *Passage of charged particles through matter*, AIP handbook, 3rd ed., McGraw-Hill, 1972.

[2] Europ. Phys. Journ. C, 3, 1998.

[3] R. M. Sternheimer and R. F. Peierls, Phys. Rev. B, 3: 3681, 1971

[4] E. H. M. Heijne, CERN Yellow Report 83-06, 1983.

[5] The European Physical Journal C, *Review of Particle Physics*, Vol 15, n 1-4, 2000

[6] W. R. Leo, *Techniques for nuclear and particle physics experiments*, Springer-Verlag, 1994

[7] L. Landau, Journ. Phys. U.S.S.R. 8, p201, 1944

[8] A. W. Ashcroft and N. D Mermin, *Solid State Physics*, Saunders College Publishing, Int. Edit. 1976

[9] R. N. Hall, Phys. Rev. 87, p387, 1952

[10] W. Shockley, W. T. Read, Phys. Rev 87, p835, 1952

[11] R. A. Smith, *Semiconductors* 2nd Edit, Cambridge University Press, 1978

[12] W. Shockley, Bell Sys. Tech. J. 28, p 435, 1949

[13] S. M. Sze, *Physics of Semiconductor Devices* 2nd Edit, John Wiley & Sons, 1981

[14] J. L. Moll, *Physics of Semiconductors*, McGraw-Hill, 1964

[15] G. Grosso, G. Pastori Parravicini, *Solid State Physics*, Academic Press, 2000

[16] E. Barberis et al., Nucl. Instr. and Meth. A 342, p90, 1994

[17] Ramo, P.I.R.E. 27, p584, 1939

[18] E. Gatti et al., Nucl. Instr. and Meth. 193, p651, 1982

[19] G. Cavalleri et al., Nucl. Instr. and Meth. 92, p137, 1971

3 Radiation Damage Mechanism in Silicon Detectors and New Results at Lower Temperature

Radiation incident on silicon detectors loses part of its energy in non-ionising processes. It will be seen in this chapter that this released energy contributes to the degradation of the quality of the material, which in turn lowers the performance of the detector. Over the last years this has been a crucial problem facing the high energy physics community, but much remains to be done to understand these processes and possible remedies. Towards the end of the chapter, one possible method to reduce the inefficiency at high fluences is explored, with experimental results.

3.1 Radiation Damage in Silicon Detectors

The energy released by high energy particles in silicon detectors causes both ionisation and atom dislocation. Although ionisation in the bulk is not damaging and constitutes the working principle of these devices, on the surface it can generate fixed positive charge at the level of the SiO_2 and SiO_2-Si interface [1] leaving permanent damage. This charge accumulation in the silicon-oxide interface significantly decreases the interstrip resistance of microstrip detectors. Given the large interest in surface damage by the electronics industry, this phenomenon is well understood and can be controlled to a certain extent by proper manufacturing processes.

The bulk can be permanently damaged when radiation causes atom dislocation in the silicon lattice and as a consequence generates deep levels in the forbidden gap. The bulk damage is a limiting factor for the use of silicon detectors in the intense radiation fields close to the interaction point of high energy physics experiments. Many studies have been done in the past characterizing these defect levels and looking at the consequences of this damage. These studies are still ongoing. In the next paragraphs some of these studies will be summarized and discussed.

3.2 Radiation Induced Defects

The elastic collision of high energy particles on lattice atoms is the main cause for the formation of defects in the silicon bulk exposed to radiation [2]. The transferred energy ΔE received by an atom of mass M_{Si} in a non ionising interaction with an impinging particle of mass m_p and energy E_p (in the non relativistic case) is given by:

$$\Delta E = 4\frac{m_p M_{Si}}{\left(m_p + M_{Si}\right)^2}\sin^2\left(\frac{\theta}{2}\right) * E_p \qquad (1)$$

where θ is the scattering angle. The threshold energy to overcome lattice bonding for a silicon atom is $E_d \approx 25$ eV [3]. When $\Delta E \geq E_d$ the displaced atom (called the *primary knock on atom* (PKA)) looses its reticular position to leave a vacancy and may occupy

an interstitial position (Frenkel pair). Both interstitial atom and vacancy can migrate in the lattice and, together with other impurities present in the crystal, give birth to permanent defects. The energy of the PKA can be high enough to recoil and continue to contribute to ionisation and additional dislocations. At the end of any heavy recoil the non ionising interaction prevails and a dense agglomeration of defects (*cluster*) is formed as displayed in Figure 1.

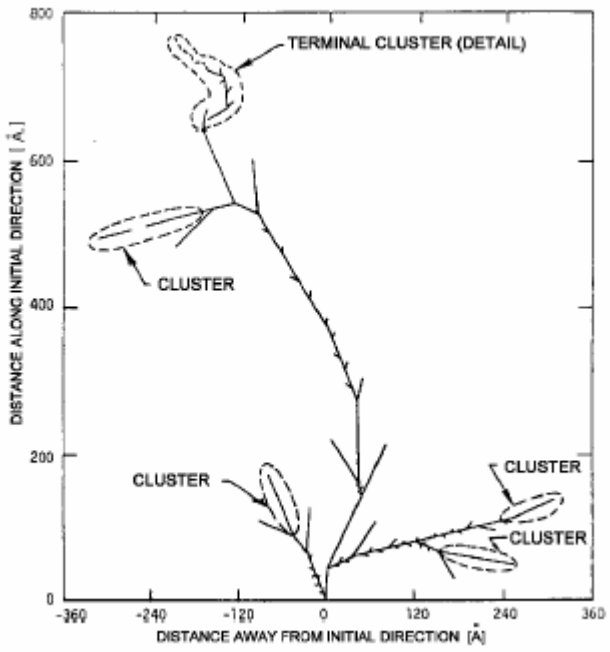

Figure 1 Monte Carlo simulation of a recoil-atom track with a primary energy of 50keV [3].

After irradiation ends, the evolution of the dislocated atoms continues. Given the high mobility of vacancies and interstitial atoms for temperatures higher than 150 K, it has been shown that, especially in the cluster region, over the 90% of these defects recombine [4]. The remaining vacancies and interstitials keep migrating through the bulk. They undergo several reactions with each other and with the impurities present in the bulk. The defects produced in these reactions cause observable damage of the silicon bulk: their electrical properties influence the macroscopic properties of the detector, degrading its performance.

3.2.1 NIEL hypothesis

The *Non Ionizing Energy Loss hypothesis* (NIEL) [5] states that for each type of incident particle, the amount of displacements-damages induced in the bulk scales linearly with energy released by the particle itself, imparted to displace silicon atoms. This allows the comparison of different particle irradiations with different energy spectrum in term of the amount of damage /displacement generated. To scale the damage one generally refers to 1 MeV neutrons, and for a given fluence Φ_{mis} of a kind of particle, one can correlate it to an equivalent fluence of 1 MeV neutrons $\Phi_{eq}^{1\,MeV}$ in the following way:

$$\Phi_{eq}^{1\,MeV} = k\Phi_{mis} \qquad (2)$$

where k is called *hardness factor*. To compute k one has to introduce the damage function $D(E_p)$ [6]. This function gives an estimation of the amount of displacements given by a particle p with energy E_p, considering the different types of interaction between the particle and the silicon atom. In Figure 2 is shown the damage function for different particles.

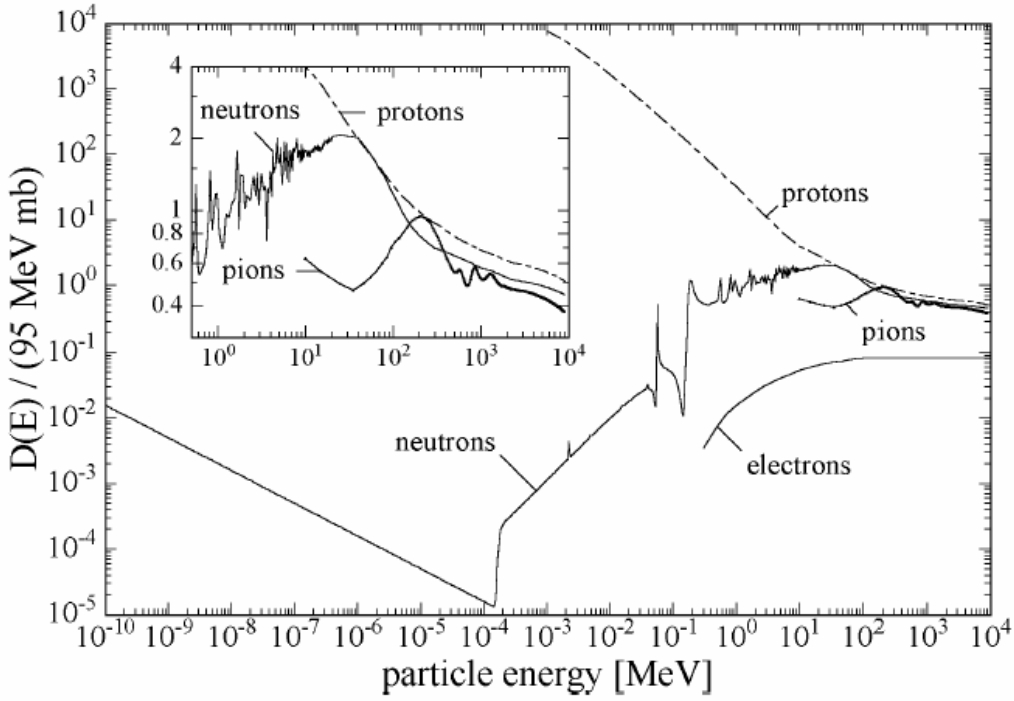

Figure 2 Displacement damage function D(E) normalized to 95 MeVmb for neutrons , protons, pions and electrons [8].

The *hardness factor k* is hence defined as:

$$k = \frac{\int D(E)\phi(E)dE}{D(E_n = 1MeV) * \int \phi(E)dE} \qquad (3)$$

where $\phi(E)$ is the particle energy spectrum and E_n is the neutron energy.

3.2.2 Defects classification

Damage in the detector bulk is characterised by two different features: the *clusters* and the *point defects*. The *cluster* model was first presented in [7]. Very little is known about the topology of this composition of vacancies and interstitials, as well as the nature of defects inside the clusters and their electrical properties in the space charge region or in thermal equilibrium.

The *point defect* is a single disarrangement of lattice atoms and/or impurity. When their energy levels are in the forbidden gap they are generally classified as *acceptors* or *donors* if their electric state is respectively negative or neutral when an

electron occupies them[1]. In thermal equilibrium the Fermi level, whose position in the bandgap depends on the type of material (resistivity) and temperature, determines the electric state of the defects. If the defects are ionised at room temperature they are in general called *shallow levels*. In the other case, i.e. when the acceptors or donors are filled respectively with a hole or an electron, they are call *deep levels* or *carrier traps*.

3.2.3 Electrical behaviour of point defects

The density of traps in highly irradiated detectors made of initially pure silicon crystal causes dramatic changes in the detector behaviour. Before looking at these changes, it is worth describing the behaviour of these traps for particular cases relevant to our study.

Carrier traps in the space charge region

In a fully depleted detector with low leakage current, one can neglect free carriers in the space charge region and hence the capture processes, deriving the occupation of the traps only from the emission process. For a fixed bias, in steady-state conditions, the generation G of holes and electrons has to be the same and can be derived from the eqn. (18) of Chapter 2:

$$p, n = 0 \quad and \quad G = -U = \frac{N_d c_n c_p n_i^2}{\left[c_n n_1 + c_p p_1\right]} \qquad (4)$$

In general one assumes c_n and c_p of the same order of magnitude and the expression for the generation can be simplified more:

$$G = \frac{N_d c n_i}{2\cosh\left(\frac{E_d - E_i}{k_B T}\right)} \quad with \quad c = c_n = c_p \qquad (5)$$

It can be seen from eqn. (5) that only defect levels with energies within few times $k_B T$ from the intrinsic Fermi level E_i play a significant role in the generation process in the space charge region.

[1] Some defects can also present more than one level in the band gap. This behaviour is called *amphoteric*.

Carrier traps under high leakage current

In the presence of a high leakage current the approximation of neglecting free carriers is not valid anymore. Hence to establish the occupation of the traps in the space charge region one has to refer to the general formulation presented in eqn. (18) of the previous chapter. Very often Shockley-Read-Hall statistics is presented with the capture coefficients expressed as:

$$c_{n,p} = \sigma_{n,p} v_{n,p}^{th} \quad with \quad v_{n,p}^{th} = \sqrt{\frac{3k_B T}{m_{c,v}}} \tag{6}$$

where $\sigma_{n,p}$ is capture cross section, $v_{n,p}^{th}$ is the thermal velocity and $m_{c,v}$ is the effective mass respectively for electrons and holes.

In the presence of multiple energy levels each level contributes separately and the total recombination-generation rate is given by $U = \sum_{traps} U_i$.

3.3 Radiation Effects on Silicon Detectors

The microscopic changes in silicon detectors due to radiation manifest as a degradation of their working properties. In this section the impact of radiation on detector properties due to the changes in the material at atomic level is analysed.

3.3.1 Depletion Voltage

The depletion voltage in a silicon detector is dominated by the value of the space charge density ($V_{dep} \propto \left|N_{eff}\right|$). With defects introduced by radiation, the value of N_{eff} changes, changing V_{dep}.

It is worth remembering that in the depleted region of the detector:

$$N_{eff} = N_{D-A}^{S} + \sum_{don} N_{don}^{D}\left(1 - f_d\right) - \sum_{acc} N_{acc}^{D} f_d + \left(p - n\right)_G \tag{7}$$

where N_{D-A}^{S} is the contribution due to all the shallow levels, f_d is the occupation probability as defined in eqn. (17) of Chapter 2, $\sum_{don} N_{don}^{D}\left(1 - f_d\right)$ is the fraction of

empty deep donors, $\sum_{acc} N_{acc}^{D} f_d$ is the fraction of occupied deep acceptors. The last term is given by the density of free carriers present in the depleted area due to diffusion from the non depleted area and, especially for highly irradiated detectors, due to their generation rate from deep levels.

A lot of studies have been done in the past to generate an empirical model for the evolution of N_{eff} after irradiation [8]. As a result it has been proven that right after the irradiation the change of depletion with the dose for an initially *n*-type material is first dominated by an apparent donor removal (decrease of V_{dep}) leading to an inversion of type of material, after which $|N_{eff}|$ starts to increase proportionally with the fluence [9]. This can lead to very high bias needed to fully deplete silicon detectors in the LHC scenario. As material type inversion has occurred, a diode that was originally p^+-*n*-n^+ will turn to a p^+-*p*-n^+ type of structure with the junction at the originally ohmic contact.

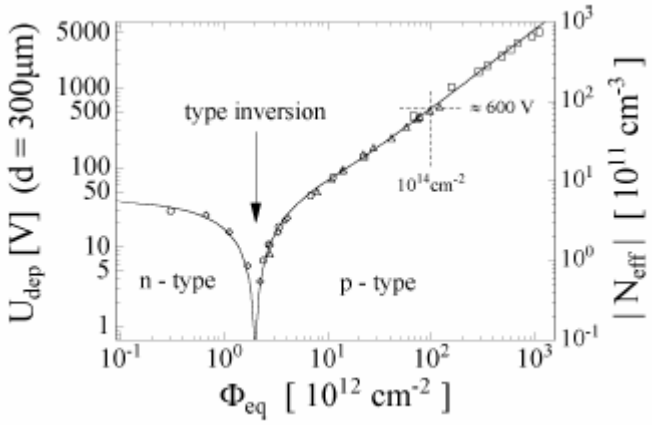

Figure 3 Change in the depletion voltage respectively the absolute effective doping concentration, measured right after the irradiation [9].

Given the fact that in the bulk defects can also migrate and combine among themselves, N_{eff} undergoes further changes (*annealing* and *reverse annealing*) at the end of the irradiation. As a result the devices experience first a period in which N_{eff} is

reduced and then, a reversal of this effect resulting in a further increase in the N_{eff}. A more detailed description of the phenomena taking place is given in [10].

Most of these studies have been based on Capacitance-Voltage measurements with diode structures [11], assuming a uniform N_{eff} in the bulk. This has been partially contradicted by recent experiments where it has been shown that although a junction appears on the back side, the profile of N_{eff} decreases with distance from the backside and inverts its sign towards the original junction side, generating another junction that is smaller than the one on the backside. The explanation of this feature is under study and an analysis can be found in [12].

3.3.2 Leakage current

In semiconductor diodes a DC current (*leakage current*) flows through the bulk. This current is due to minority carriers diffusing in the Space Charge Region (SCR) from undepleted regions and thermally generated carriers in the SCR [13]. For non irradiated silicon detectors, the leakage current density is of the order of 100 nA/cm^3. In irradiated detectors the thermally generated current strongly dominates and increases rapidly with irradiation due especially to deep levels' injection. Assuming a uniform recombination-generation rate U_t for each trap in the SCR the resulting leakage current density will be:

$$J = qd \sum_{traps} U_t \qquad (8)$$

where d is the thickness of the SCR. From this expression one can get also a feeling for how the current decreases rapidly with decreasing reducing the temperature, given that from eqn. (5) and eqn. (6) all the terms, except N_d, depend on the temperature, with $\sigma_{e,h} \propto T^{-m}$ with m varying from 0 to 2 [14] (see Figure 4).

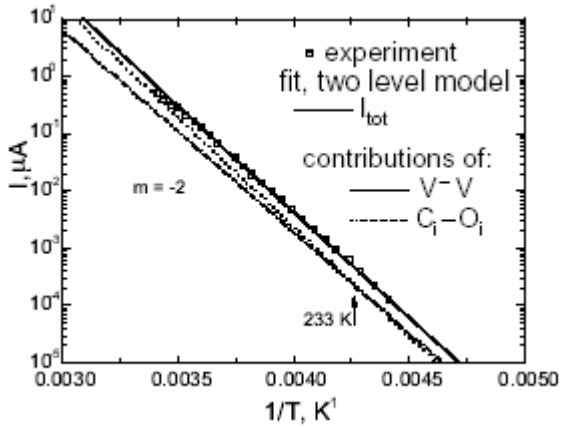

Figure 4 Experimental dependence of the reverse current on temperature for a Si detector irradiated by γ-rays and fits using equation (8) according to a double-level generation model where the considered defects are the V-V and C_i-O_i [14].

It has been found that the leakage current increases linearly with the irradiation dose through the relation:

$$\frac{J(\Phi_{eq})-J_0}{d}=\alpha(t,T_a)\Phi_{eq} \qquad (9)$$

where $\alpha(t,T_a)$ is the current related damage rate. This parameter with value of approx 10^{-17} A/cm has been widely studied and its behaviour with respect to annealing temperature and time can be found for example in [16].

3.3.3 Charge Collection Efficiency

The 100% efficiency in silicon detectors is lost as they absorb a high dose of radiation: the deep levels induced by radiation trap the free carriers generated by ionizing radiation reducing the collection of the charge at the readout electrodes. How much the trapping influences the collection is also due to the particular weighting field of the electrode itself. To better visualise this it is worth describing this phenomenon more accurately. Considering an ionizing track in the depleted detector and, for sake of simplicity, considering the case in which this track lies along an electric field line, the initial distribution of generated carriers along the track that we will call $\pm q_0(x)$ will evolve due to the electric field and the trapping time. The

evolution of each cloud of holes and electrons between the generation point x_0 and an arbitrary point *x* along their drift is respectively:

$$q_{h,e}(x,x_0) = \pm q_0(x_0)\exp\left(-\frac{t_{h,e}(x,x_0)}{\tau_{h,e}}\right) \quad with \quad t_{h,e} = \int_{x_0}^{x} \frac{d\xi}{\pm \mu E} \tag{10}$$

where $\tau_{h,e}$ is respectively the hole and electron trapping time and $t_{h,e}$ is the time taken to reach *x* from x_0. During the motion to the electrodes placed in *d* and in 0 along $\hat{x}$ (the first collects holes and the second collects electrons) the hole and electron contributions to the charge induced is:

$$Q_{h,e}(x_0) = -\int_{x_0}^{d,0} q_{h,e}(x,x_0) * \vec{E}_W(x) \cdot d\vec{x} \tag{11}$$

and the charge collection efficiency is given by

$$CCE = \frac{\int_0^d \sum_{h,e} Q_i(\xi) d\xi}{\int_0^d q_0(\xi) d\xi} \tag{12}$$

In the simple geometry of pad detector with the approximation of uniform electric field it is easy to see that for a uniform generation of charge along $\hat{x}$ with linear charge density $\pm q_0$ the contributions of holes and electrons are:

$$\overline{Q}_{h,e} = \int_0^d Q_{h,e}(\xi) d\xi = q_0 \delta_{h,e}\left(1 - \frac{\delta_{h,e}}{d}\left(1 - \exp\left(-\frac{d}{\delta_{h,e}}\right)\right)\right) \tag{13}$$

where $\delta_{h,e} = \mu_{h,e} E \tau_{h,e}$ is the average drift length. If one considers both average drift lengths equal to δ just for a simple illustrative purpose the collection efficiency is:

$$CCE = \frac{\overline{Q}_e + \overline{Q}_h}{q_0 d} = \frac{2\delta}{d}\left(1 - \frac{\delta}{d}\left(1 - \exp\left(-\frac{d}{\delta}\right)\right)\right) \tag{14}$$

and its behavior is shown in Figure 5.

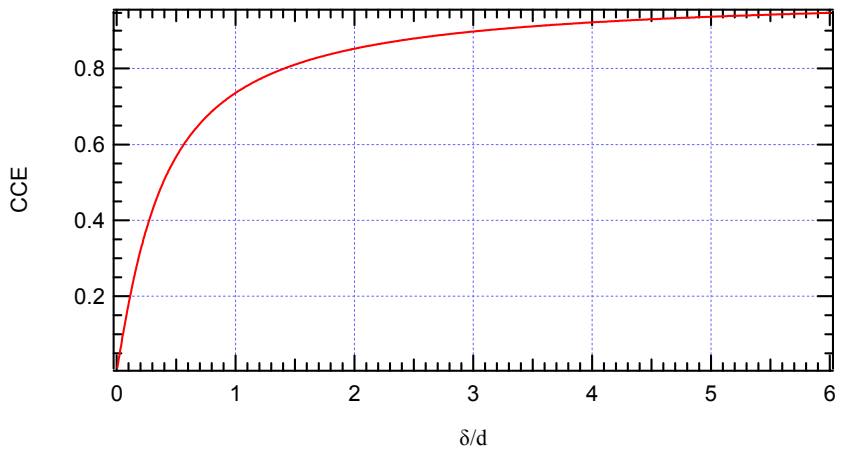

Figure 5 Charge collection efficiency (CCE) dependence respect to the ratio of the average drift length δ with the detector thickness d.

As it can be seen in this particular case the CCE drops to 70% as the average drift length reduces to the detector thickness and rapidly decreases for shorter δ .

Considering to all traps an effective trapping time can be defined in terms of the trap's occupation probability f_d for each carrier, i.e. the probability of the carriers being trapped given by:

$$\begin{aligned} \frac{1}{\tau_{eff_e}^{Tr}} &= \frac{1}{\sum_d \tau_{d_e}^{Tr}} = v_e^{th} \sum_d \sigma_d^e N_d^D \left(1 - f_d\right) \quad \textit{for electrons} \\ \frac{1}{\tau_{eff_h}^{Tr}} &= \frac{1}{\sum_d \tau_{d_h}^{Tr}} = v_h^{th} \sum_d \sigma_d^h N_d^D f_d \quad \textit{for holes} \end{aligned} \tag{15}$$

where $\tau_{d_{e,h}}^{Tr}$ is the trapping time for the single defect *d* with density N_d^D .

Also the effective trapping times can be parameterised in terms of radiation fluence as:

$$\frac{1}{\tau_{eff_{e,h}}^{Tr}} = \beta_{e,h}\left(t, T_a\right)\Phi_{eq} \tag{16}$$

where $\beta_{e,h}\left(t, T_a\right)$ is generally called the effective electron or hole trapping damage constant. Recent measurements of this parameter can be found in [17].

3.4 Low temperature operation as a radiation hardening mechanism

The high fluence foreseen for LHC operation at the level of the silicon trackers has raised the need of studying new possibilities to reduce the effects of the damage generated by high radiation. Different research projects were born in the last years within this context, based on different approaches on how to improve the radiation hardness of the trackers in the LHC detectors. In this section we will look at one particular technique developed from a first observation of radiation hardening of silicon when cooled down to low temperature [18].

In the next paragraphs will follow the description of the behaviour of the charge collection at temperatures between 77 and 200 K. This unconventional range to use silicon detectors has shown to be very promising in terms of radiation hardness leading the collaboration CERN RD 39 [19] to propose low temperature operation for silicon detectors as a remedy to the radiation damage for experiments where, due to harsh radiation environments and high background, radiation hardness is required. The effect of recovery of the CCE with the temperature has been called the "Lazarus effect" and has been shown to extend the radiation hardness of silicon to fluences at least ten times higher than what was previously studied.

The characterization of the Lazarus effect has been based on the measurement of the charge collection efficiency (CCE). It is worth remembering that non irradiated silicon detectors are 100% efficient at full depletion. The degradation of the CCE after irradiation can come from incomplete depletion (the carriers generated in the non depleted area are not collected) and carrier trapping (part of the generated carriers are trapped before reaching the collecting electrodes). From these two phenomena one can define the CCE due to trapping for holes and electrons as:

$$CCE_t^{e,h} = \frac{\overline{Q}_{e,h}}{2q_0 d} \qquad (17)$$

where all the terms in the equation are defined previously in *(12)* and *(13)* and the CCE due to undepletion that, for radiation generating charge uniformly in a pad detector, is:

$$CCE_d = \left(\frac{W}{d}\right)^2 \qquad (18)$$

where W is the extension of the depleted layer. It is worth stressing that with the partial depletion of the detector:

$$CCE_t^{h,e} = \frac{\delta_{h,e}}{W}\left(1 - \frac{\delta_{h,e}}{W}\left(1 - \exp\left(-\frac{W}{\delta_{h,e}}\right)\right)\right) \qquad (19)$$

and that:

$$CCE = CCE_d \cdot \left[CCE_t^e + CCE_t^h\right] \qquad (20)$$

To evaluate the low temperature recovery of the CCE the behaviour of terms contained in (20) with respect to temperature have to be evaluated.

The following description will contemplate measurements with detectors previously irradiated at room temperature as described extensively in [20] and represent the main achievement of my Laurea thesis [21]. These data will be then compared to the results that came out of an experiment of irradiation "in situ" at low temperature to check whether the damage at low temperature would carry different macroscopic features with respect to the damage at room temperature. The "in situ" irradiation experiment has been carried out in the context of this thesis and described also in the publication [22]. At the end of the chapter the temperature dependence of the terms in (20) will be described in detail explaining the Lazarus effect.

3.4.1 The "Lazarus effect"

The investigation of the CCE vs. Temperature has been made with DC-coupled p^+-n-n^+ silicon pad detectors processed at BNL (Brookhaven National Laboratory, USA) with a sensitive area of 5×5 mm^2 surrounded by a guard ring and, before irradiation, full depletion achieved with voltages above 50–80 V. These diodes were irradiated unbiased at room temperature with neutrons in the TRIGA reactor of Ljubljana. The properties of the investigated detectors are summarized in Table 1.

Diode	Fluence (n/cm^2)	Thickness (μm)	Resistivity (kΩ cm)
#1	1×10^{14}	350	1.8
#2	5×10^{14}	400	4.0
#3	1×10^{15}	400	4.0
#4	2×10^{15}	300	2.7

Table 1 Parameters of the investigated diodes. The resistivity values are those before irradiation

To measure the CCE a ^{90}Sr β-source with a maximum energy of 2.3 MeV was used. The selection of Minimum Ionizing Particles (MIPs) was done using a second silicon detector placed behind the detector under study The temperature dependence of the CCE for these detectors is presented in Figure 6. These detectors, biased with a voltage such that at high temperature they are certainly not fully depleted, show some common features. All detectors show very low CCE values in the high temperature range. A substantial rise of the CCE starts around 180 K, and the CCE reaches its maximum value at a temperature of around 130 K for all samples.

From the fluence of $5*10^{14}$ n cm^{-2} on the CCE is lower than 100% at the maximum applied bias voltage of 250 V; however, some recovery effect is still observable at low temperatures. Another common striking feature is that the CCE decreases with time, i.e. the measurements repeated some time after turn-on of the HV yield a monotonically decreasing CCE, which converges towards a stable value. The time dependence of CCE for #3 is also shown in Figure 6 (right).

Forward bias operation has been considered very interesting for heavily irradiated silicon detectors, and promising results have already been obtained in the case of moderate cooling [23]. It is worth stressing, however, that in the case of cryogenic operation, due to very high bulk resistivity, one cannot distinguish this mode from the conventional reverse bias operation, judging from the current passing through the detector.

The temperature dependence of the CCE for detectors #2, #3 and #4 is shown in Figure 7 (left) for forward bias operation. The CCE starts increasing around 180 K and saturates below 130 K, for all detectors. Measured values are about three times higher than those observed under reverse bias. Moreover, good values of CCE start being recorded as soon as the temperature is low enough to allow the measurements.

The observation of good CCE values for these relatively high temperatures is in good agreement with previous observations [23] [24].

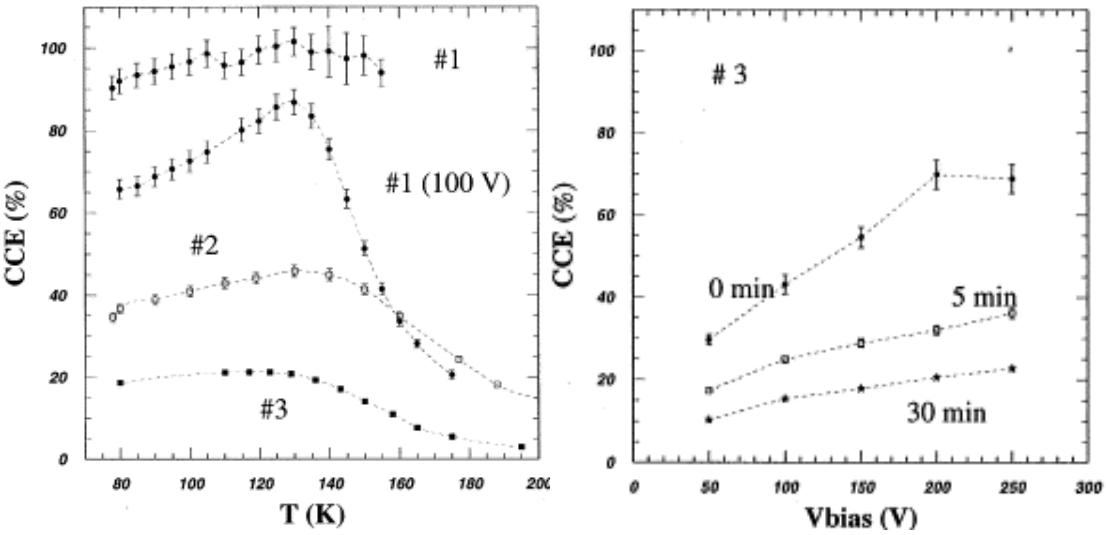

Figure 6 Temperature dependence of CCE for detectors #1, #2 and #3 (left) and Voltage dependence of the CCE of detector #3 at 77 K, measured at different time intervals after HV turn-on (right).For the temperature dependence the three detectors were measured with a reverse bias voltage of 250 V. The detector #1 was measured also with a reverse bias voltage of 100 .

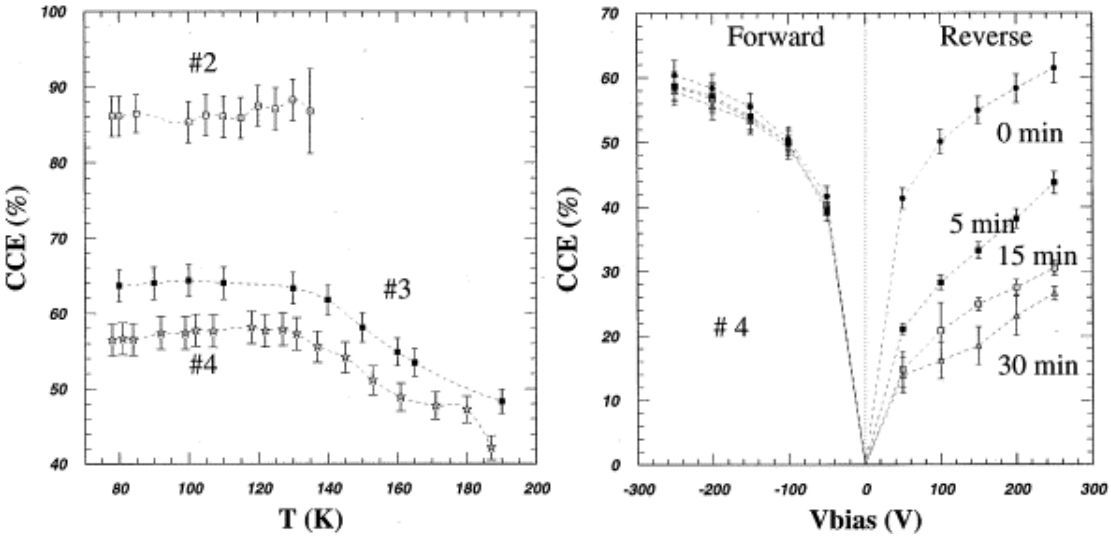

Figure 7 On the left, temperature dependence of the CCE for detectors #2, #3 and #4, all operated at a forward bias voltage of 250 V. On the right, voltage

dependence of the CCE of detector #4 in the extended voltage range. Measurements at different time intervals after HV turn-on are shown

In Figure 7 is also shown the CCE measured at 77 K for #4 over the full range of available bias voltage at different times from the application of the HV.

The CCE is about three times higher with forward bias than with reverse bias in stable conditions. Moreover, under forward bias operation the detector shows a time-independent CCE and, the large values obtained are similar to those observed under reverse bias immediately after switching on the HV.

3.4.2 "In situ" irradiation at low temperature

In the "in situ" irradiation experiment a silicon structure of square pads with active area 1.5x1.5 mm^{-2} configured as a 3x3 array pad detector p^+-n-n^+, 400 μm thick with 4k Ωcm float-zone substrate was irradiated at 83 K with 450 GeV protons at the CERN-SPS. The upper central pad was exposed to a dose of 1.2×10^{15} p·cm^{-2}, with 450 GeV protons. This would correspond to a 1 MeV neutron fluence of about 6×10^{14} n·cm^{-2} [25]. However, this conversion is based only on extrapolation of existing data, since no damage conversion factors for particles of such high energy are available in the literature.

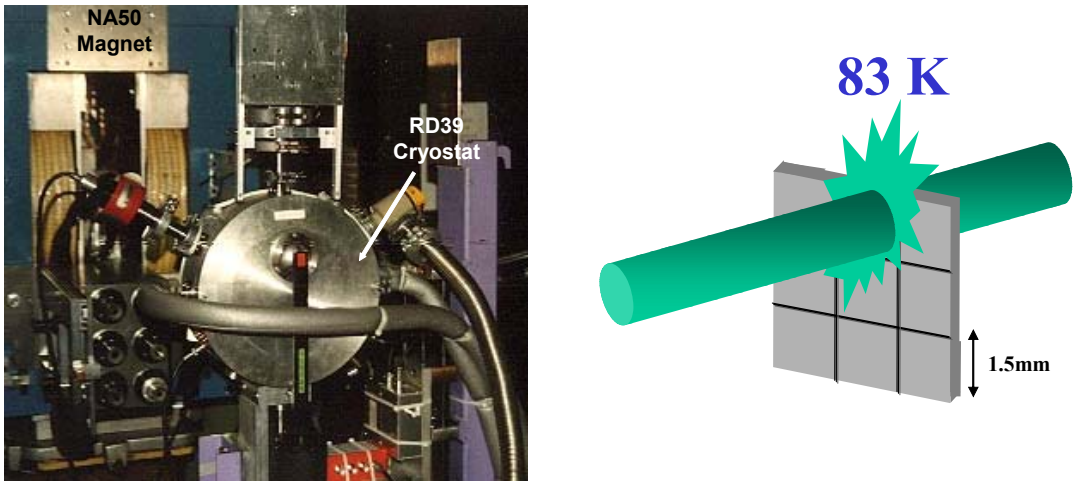

Figure 8 Picture of the cryostat used for the "in situ" irradiation at the H.I. SPS proton beam area at CERN (left), schematic of the pad matrix irradiation (right).

At this extreme dose, operation at cryogenic temperatures ensures negligible leakage current, making it possible to perform charge collection efficiency (CCE) measurements on the detector. For these, it was necessary to insert trigger scintillators into the beam and hence the beam intensity was lowered to 10^5 p/spill at 300 GeV by inserting an Aluminium target 118m upstream from the detector. A continuous flow liquid nitrogen cryostat housed the test diodes. The sample holder was kept in an ultra high vacuum chamber and was connected to a cold copper finger. The sample was then cooled by thermal conduction down to 83 K. The proton beam entered the cryostat via two 100 μm stainless steel windows aligned with the test detector. Two scintillators, external to cryostat, were used to provide coincident triggers for the detection of minimum ionising particles (MIPS). The detector under test was read out with a charge amplifier (shaping time constant of 2 μs) placed outside the cryostat. The signal was connected to an oscilloscope (LeCroy 9350), which was used to build histograms of the charge spectrum.

Experimental result.

Once the system had been cooled to 83 K, CCE measurements were taken. The signals were normalised to those from a fully depleted pad before the irradiation, which achieves 100% CCE at 50 V, as shown in the Figure 9. For the irradiated pad, each measurement was performed after the detector had been left at 0 V for a few minutes, to allow de-polarisation. In fact, the electric field in a damaged bulk of the silicon detector, and its time dependence, are strongly related to the spectrum of the deep levels present in the band gap [26]. It was therefore important to start measurements with the detector always in a stable condition. Then, having biased the detector, the CCE was monitored for about 1 h and found to have a stable value in time up to the dose of 6.5×10^{14} p cm^{-2}.

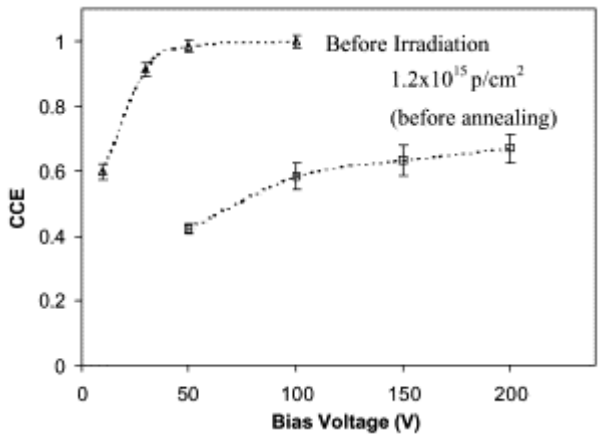

Figure 9 Charge collection efficiency at different bias voltage. The two curves indicate the behaviour of the detector before the irradiation and after the maximum dose (1.2×10^{15} p cm^{-2}), at 83 K. For the1.2×10^{15} p cm^{-2} curve are displayed only the initial values.

The CCE observed at different reverse bias voltages, increased as the voltage was increased. Starting from 100% CCE at 50 V for zero dose, the CCE is seen to decrease with the dose absorbed. At the fluence of 1.2×10^{15} p cm^{-2} a time dependence of the CCE appears, with an initial value of 42% right after the biasing at 50 V bias. At this dose, with the bias voltage increased to 200 V to improve the efficiency, an initial CCE of 67% was reached. The CCE increases with voltage within all the observed range, suggesting a higher value of the CCE for higher bias voltage. The increase with the voltage of the initial CCE follows a fast rise until 100 V and then a slower rise (see Figure 9).

After the maximum irradiation dose, the detector was warmed first at 160 K. After less than 1 h, once the CCE was measured, the detector was warmed again up to 207 K, and kept at this temperature for 1 h while making measurements. At 160 K, with a bias voltage of 200 V, the CCE reaches a value of 95% and no degradation with time is registered. These measurements are shown in Figure 10. It is worth noting how the rising slope of the CCE curves varies with the temperature.

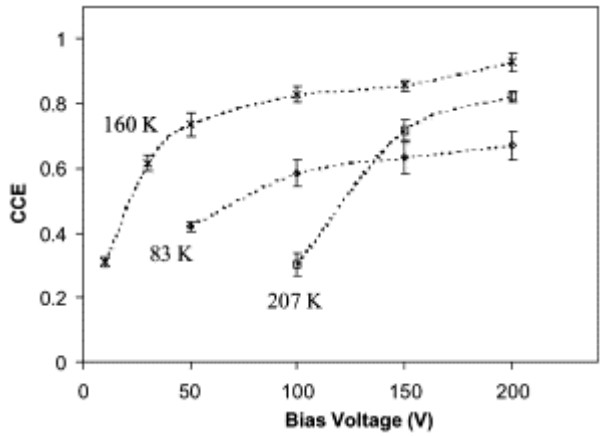

Figure 10 CCE at the temperature of 160 and of 207 K compared with the one registered before warming up at T=*83 K. For all the curves the absorbed dose is* 1.2×10^{15} *p* cm^{-2}.

Then the detector was cooled down again to 83 K. At the end of the thermal cycle, a recovery of CCE above the 60% level at 50 V bias is observed (see Figure 11). With a further increase of bias to 200 V, the detector regains a CCE of 95%.

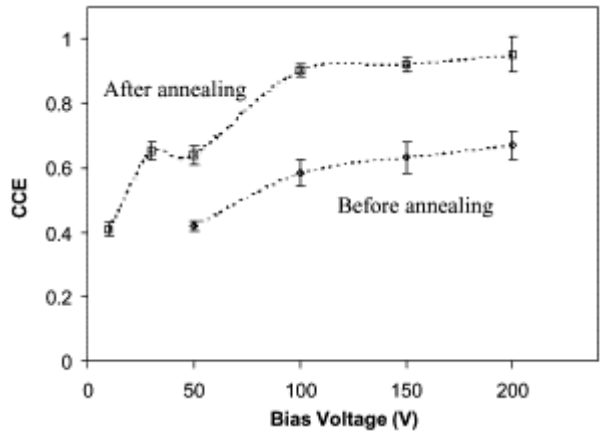

Figure 11 CCE of the sample at 83 K after accumulating the maximum dose before annealing and at the end of the thermal cycle.

The sample was checked again after one year spent at room temperature. The test was done with the set up specified in [20]. The detector was biased at 190 V and the CCE was checked. A stable value of 53% was found which is compatible with the CCE measured at the maximum dose before the annealing.

It is interesting to note a time evolution of the CCE that takes place above fluences of 6.5×10^{14} p cm^{-2}. This effect, though lightly apparent at 1.2×10^{15} p cm^{-2}, is more evident after a partial annealing. Nevertheless, this CCE degradation with time seems not to compromise the beneficial annealing for which a stable value above 70% CCE is observed at 200 V bias voltage (Figure 12).

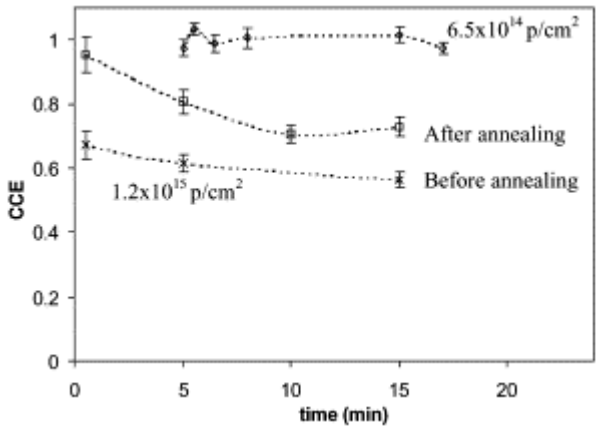

Figure 12 Charge collection efficiency evolution of CCE with time at 83 K and a bias of 200 V for a dose of 6.5×10^{14} p cm^{-2} and for the maximum dose (1.2×10^{15} p cm^{-2}) before annealing and at the end of the thermal cycle.

These experimental results show that the CCE recovery of a heavily irradiated silicon detector when operated at low temperature is not affected by the temperature during irradiation. Moreover, if one were to compare the data shown in this work following an irradiation of 1.2×10^{15} $p_{450\ GeV}$ cm^{-2} equivalent approximately to 6×10^{14} $n_{1\ MeV}$ cm^{-2}, with the results following room temperature during irradiation, one would find a reasonable compatibility. Also, the fact that the reverse annealing does not affect the recovery of the CCE leads to the conclusion that to improve radiation hardness cooling is needed only during operation.

3.4.3 Physical analysis of the Lazarus Effect

The recovery of the CCE with temperature for highly irradiated silicon detectors has shown to be maximum for ~130 K (see Figure 6) if the detector is operated at normal reverse bias. Moreover it has been shown that better results can be achieved if the device is operated in forward bias with a saturation of the CCE occurring at ~130 K. Nevertheless, although this result is extremely positive, it is

more complicated to realise for experiments using this approach due to the need of bipolar power supplies in order to switch mode in different moments of the experiment.

For the ordinary reverse bias, the characteristic behaviour of CCE(T) that is independent of the fluence can be explained as a competition of increase of depletion and trapping at the same time. In fact, as has been shown previously the loss of CCE can be split in to CCE_t and CCE_d. The temperature dependence of CCE_t arises mainly from the dependence of τ on T, since μE is nearly constant due to the saturation of the drift velocity v_{dr}. Since

$$\tau = \frac{1}{\sigma v_{th} N_{tt}} \qquad (21)$$

where σ is the effective carrier capture cross section for trapping centers with the total concentration N_{tt}, and v_{th} is the thermal velocity of the carrier. The temperature dependence of τ is due to that of the involved parameters. Among these the power-law dependencies are theoretically predicted for σ [14] and v_{th}:

$$\sigma = \sigma_o \left(\frac{T}{300}\right)^{-m} \qquad 0 \le m \le 2 \qquad (22)$$

$$v_{th} \sim T^{1/2} \qquad (23)$$

where σ_0 is the capture cross-section at room temperature.

Nevertheless, the concentration of trapping centres, which contribute to *CCE*, is temperature dependent and gives even stronger dependence compared with that for σ and v_{th}, due to the changes of charge state with temperature. Therefore the different types of charge states, including electrically neutral energy levels with high de-trapping time (>1 μs) should be taken into account in trapping-related effects. Consequently, the effective concentration of trapping centres N_{tt} is defined as the sum

of the concentrations of both types of traps: the charged deep donors $\sum_{don} N_{don}^{D}$ and deep acceptors $\sum_{acc} N_{acc}^{D}$ and the neutral deep levels $\sum_{neut} N_{neut}^{D}$:

$$N_{tt} = \sum_{don} N_{don}^{D} + \sum_{acc} N_{acc}^{D} + \sum_{neut} N_{neut}^{D} \qquad (24)$$

On the other side, the temperature dependence of CCE_d then arises from the dependence of W on T through:

$$W^2 = \frac{2\varepsilon\varepsilon_o V}{eN_{eff}} \qquad (25)$$

where ε and ε_0 are the permittivity of silicon and vacuum, respectively, e is the elementary charge and N_{eff} is the effective concentration of charged centres in the SCR. N_{eff}, as it was shown in *(7)* is the difference between the concentrations of positive charges and negative charges present in the SCR, which are also temperature dependent. The sign of N_{eff} is determined by the relative contributions of the charges.

In the specific case of heavily irradiated Si detectors the main contribution to N_{eff} arises from the charged states of deep levels. Indeed, for non-irradiated high purity Si, the concentrations of charged shallow levels N_{SL} (donors and acceptors) are less than 10^{12} cm^{-3} and are constant in the wide range of temperature down to 20 K. Moreover, after irradiation, these concentrations may be even lower due to shallow donor/acceptor removal [10]. In contrast, concentrations of the radiation-induced deep levels for detectors irradiated up to $\Phi_n \geq 1 \cdot 10^{14}$, reach values $\geq 10^{14}$ cm^{-3} [27] [28], Hence for heavily irradiated Si detectors in a wide temperature range one can disregard the contribution of the shallow levels to the space charge, and given the fact that free carriers strongly decrease with temperature, in our range of interest N_{eff} can be entirely defined by the concentrations of charged deep levels:

$$N_{eff} \approx \sum_{don} N_{don}^{D} - \sum_{acc} N_{acc}^{D} \qquad (26)$$

The Eqs. (24) and (26) define the concentrations N_{tt} and N_{eff}, which are responsible for the main factors of the *CCE*. The overall *CCE* is affected by both trapping and depletion factors:

$$CCE = CCE_t * CCE_d \qquad (27)$$

Noting that N_{tt}, responsible for CCE_t, is the sum of the total concentrations of deep donors and acceptors, whereas N_{eff}, which controls CCE_d, depends on the difference between the charged fraction concentrations only, in the case of large and close concentrations of deep donors and deep acceptors, as it happens for high irradiated detectors, the trapping component CCE_t will be less sensitive than CCE_d to the changes with temperature of the charged deep level concentrations. This is a strong argument in favor of the statement that the Lazarus effect is related to the changes of N_{eff} with temperature, bringing to the maximum depletion, and so to the maximum CCE_d per given bias for $T \approx 130K$. The reason for a decrease of the CCE once $T \approx 130K$ is reached, has to be the found in the fact that, although the capture cross sections of the charged centres can be a factor of 10 larger than that of neutral centres [29], implying that the charged centres will play a dominant role in trapping if both concentrations are of the same order of magnitude, the concentrations of the charged fractions of the deep levels decrease rapidly with decreasing temperature, and the neutral fraction becomes dominant in trapping. So, for $T \leq 130K$, the CCE is controlled by the trapping mechanism. In this temperature interval the increase in carrier capture cross section as defined by (22) leads to a significant reduction of the trapping time constant, which in turn leads to the *CCE* decrease.

In Figure 13 is shown a comparison of the numerical simulation of CCE and CCE_d with the measurement of the CCE at different temperatures for the detector #1 (from Table 1). This quantitative comparison to the data together with the modelling of charge collection mechanisms in highly irradiated detectors has been produced in the framework of the RD39 Collaboration. A more detailed analysis of these processes together with their numerical simulation can be found in [30].

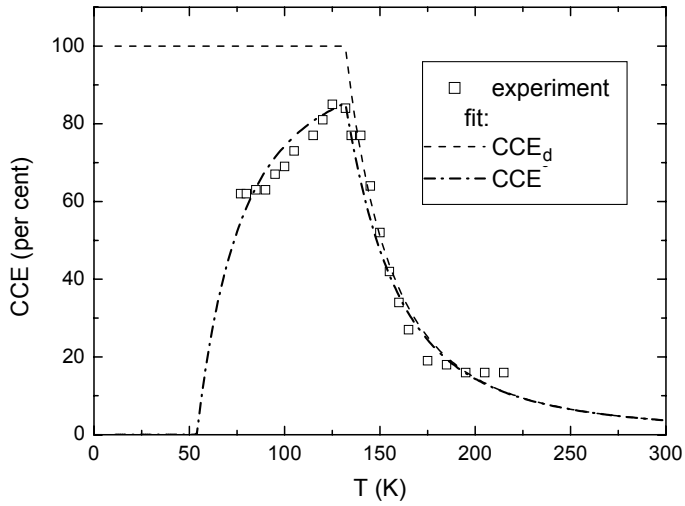

Figure 13 Experimental temperature dependence of the CCE for detector #1 (biased with 100 V) compared with its quantitative model.

3.5 References

[1] G. C. Messenger, M. S. Ash, *The Effects of Radiation on Electronic Systems*, Van Nostrand Reinhold; 2nd edition (July 1992)

[2] V.L. Vinetskii and G.A. Kholodar, *Physics of Radiation Effects in Crystals*, Eds. V.M. Agranovic and A.A. Maradudin, Vol.13, 283, North Holland 1986

[3] V.A.J. van Lint, T.M. Flanagan, R. E. Leadon, J.A. Naber, V.C. Rogers, *Mechanism of Radiation Effects in Electronic Materials,* John Wiley & Sons, 1980

[4] Y. Shi, D.X. Shen, F.M. Wu and K.J.Cheng. A numerical study of cluster centre formation in neutron-irradiated silicon. J. Appl. Phys., Vol. 67, 1116 (1990)

[5] G. Summers et al. IEEE Trans. Nucl. Sci., Vol. 34, 1134 (1987)

[6] J. Lindhard et al., Kgl. Danske Videnskab. Mat. Fys. Medd. Vol 33, n. 10 (1963)

[7] B.R. Gossick. Disordered Regions in Semiconductors Bombarded by Fast Neutrons. J. Appl. Phys. Vol. 30, 1214 (1959)

[8] 2nd RD48 Status Report, 1998. LEB Status Report/ RD48, CERN / LHCC 98-39

[9] R. Wunstorf, Systematische Untersuchngen zur Strahlenresistenz von Silizium Detektoren fur die Verwendung in Hochenergiephysik-Experimenten. PhD thesis, Univesitat Hamburg,1992

[10] M. Moll, Radiation Damage in Silicon Particle Detectors, PhD thesis, Universitat Hamburg, 1999.

[11] D. K. Schroder, *Semiconductor Material and Device Characterization*, John Wiley & Sons, Inc. 1990

[12] V. Eremin et al., Nucl. Instr. and Meth. A476 (2002) 556-564

[13] S. M. Sze, *Physics of Semiconductor Devices* 2nd Edit, John Wiley & Sons, 1981

[14] Abakumov V.N. et al. Sov. Phys. Semicond., 12, 1 (1978)

[15] RD39 Status Report, 2002 / RD49, CERN / LHCC 2002-004

[16] H. Feick, Radiation Tolerance of Silicon Particle Detectors, PhD thesis, Universitat Hamburg, 1997.

[17] G. Kramberger et al., Nucl. Instr. Meth. A476 (2002) 645

[18] V. Palmieri *et al.*, *Nucl. Instr. and Meth. A* **413** (1998), p. 475

[19] RD39 Collaboration, K. Borer et al., CERN/LHCC 98-27, DRDC P53 Add. 1 (1998).

[20] K. Borer et al*., Nucl. Instr. and Meth. A* **440** (2000), p. 5

[21] G. Ruggiero, Resistenza alla radiazione di rivelatori al silicio operanti a temperature criogeniche, Laurea thesis, Universita di Napoli “Federico II”, 1999.

[22] G. Ruggiero et al., *Nucl. Instr. and Meth. A* **476** (2002), p. 583

[23] L.J. Beattie et al., in proc. Elmau Workshop "New developments on radiation detectors", 8th European Symposium on Semiconductor Detectors, Schloß Elmau, June 14–17, 1998,

[24] A. Chilingarov and T. Sloan. *Nucl. Instr. and Meth. A* **399** (1997), p. 35

[25] RD 48 Collaboration, V. Augelli, et al., CERN/LHCC 98-39, LEB Status Report/ RD48 21 October 1998

[26] V. Eremin *et al.Sov. Phys. Tech. Semicond.* **8** (1974), p. 1157

[27] L. Beattie et al, *Nucl. Instr. and Meth. A* **412** (1998) pp. 238-246.

[28] B. Dezillie, et al., IEEE Trans. Nucl. Sci., vol. **46**, No. 3 (1999) 221-227

[29] E. Verbiskaya, private communication

[30] V. Eremin, E. Verbitskaya, I. Ilyashenko, Z. Li, T.O. Niinikoski and G. Ruggiero, Temperature dependence of charge collection efficiency in heavily irradiated silicon detectors: the Lazarus effect model, submitted to Nucl. Instr. and Meth. **A**

4 Simulation of Silicon Detectors

The signal formation in silicon detectors cannot be calculated analytically when the detector assumes complicate geometries. Nevertheless for a good understanding of these devices it is worth to simulate numerically the processes taking place that originates a signal at the electrodes. In this chapter a successful attempt to simulate microstrip detectors based on simple numerical recipes will be shown.

4.1 Simulation Strategy

Given the strong interest in the silicon industry, many products have been developed in the last decades to simulate silicon devices. Most of the times these packages tend to be very powerful but require particular CPU architectures to be used. Instead, the simulation that will be described in this chapter has been developed for any commercial PC (under Windows or Mac OS), using the application IGOR Pro by WaveMetrics [1]. IGOR Pro is an interactive environment for experimentation with scientific and engineering data, completely programmable via a built-in programming environment and equipped with an extended variety of graphic tools to visualise data.

The simulation package has been developed within three main steps:

- *The computation of electrostatic fields*
- *The charge transport through the drift-diffusion process.*
- *The induction of the signal at the microstrip electrodes.*

Given the symmetry of the devices under investigation a 2D simulation is sufficient to explore all those points listed above. For its simpler development finite difference methods have been mainly used. These numerical recipes used will be described with more details in the next sections.

4.2 Electric and Weighting field calculation

4.2.1 The Electric Field

The numerical resolution of the Poisson equation is often the only way to evaluate the electric potential, also for simple domain geometry and boundary conditions. In the devices of our interest the potential is independent of the coordinate along the strip direction. This reduces the numerical evaluation over a 2D mesh on whose points the potential $U(\vec{r})$ is computed with the numeric evaluation of the equation:

$$\nabla^2 U(\vec{r}) = -\frac{eN_{eff}(\vec{r})}{\varepsilon_{Si}\varepsilon_0} \qquad (1)$$

Furthermore given the regular repetition of strips, the restriction of the 2D domain to a cell that extends over a half of a strip pitch (starting from half strip up to the next half of the inter-strip mid-gap) is sufficient.

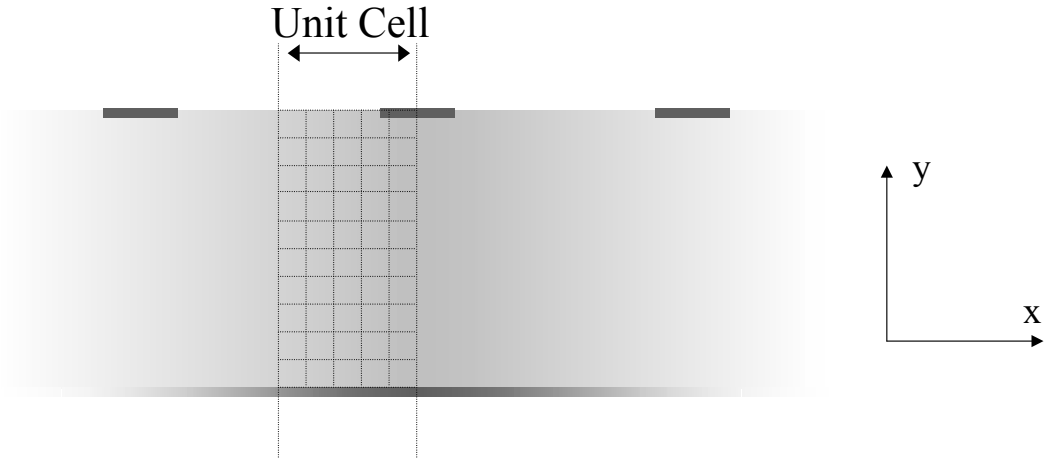

Figure 1 Unit Cell to which limit the numerical evaluation

Hence the boundary condition for a fully depleted p^+-n-n^+ strip detector is given by:

1. U=V_{bias} at the strip, where V_{bias} is the bias at which the simulated detector is operated
2. $\partial U / \partial y = 0\,V$ at the surface on the interstrip gap, i.e. the electric field in this region is parallel to the surface
3. $U=0\ V$ at the backplane
4. $\partial U / \partial x = 0\,V$ at the two lateral cell edges, due to the mirror symmetry respect to these edges.

It is worth noting that usually microstrip detectors have a layer of SiO_2 covering the interstrip gap. As seen previously the presence of a native positive charge in the SiO_2 layer attracts electrons in an accumulation layer that is present also when the detector is depleted shielding the electric field due to the positive charge. In this sense, it is intended that the condition 2 above is an approximation to the real

behaviour. The simulation of this accumulation layer in silicon microstrip detectors can be found for example in [2] or [3]. Nevertheless in the next chapters there will be the occasion to see the quality of this approximation comparing simulations with measurements.

Within these boundaries, the domain is reduced to a mesh of points where the Poisson equation is calculated. The method used is the Finite Difference (FD) [4]. To simplify the calculation the mesh is chosen uniform with a constant mesh distance equal in the direction *x* and *y*. The calculated value is the average value of the real potential over the region surrounding the mesh point limited by the half distance with the adjacent mesh points.

For a reliable calculation in semiconductors where the charge varies in the volume, the mesh distance does not have to exceed the Debye length, which is given by:

$$L_D = \sqrt{\frac{\varepsilon_r \varepsilon_0 k_B T}{q^2 N_{eff}}} \qquad (2)$$

This is due to the fact that between two differently doped regions the carriers will diffuse from the region with higher doping to the region with lower doping, following an exponential decrease ruled by the distance L_D. In low resistivity silicon with $N_{eff} \approx 10^{12}$ L_D is about .5 μm. Nevertheless, at this stage we will consider only fully depleted detectors, where the space charge is supposed to be almost uniform through all the bulk. This allows a less restrictive distance mesh in the internal region. Moreover the implants being normally 1 μm thick they will be considered as linear arrays on external mesh points. An example of calculation of the electric potential and electric field is shown in Figure 2, where the values are calculated over a region which is the double of the unit cell used for the numeric calculation and shown in Figure 1.

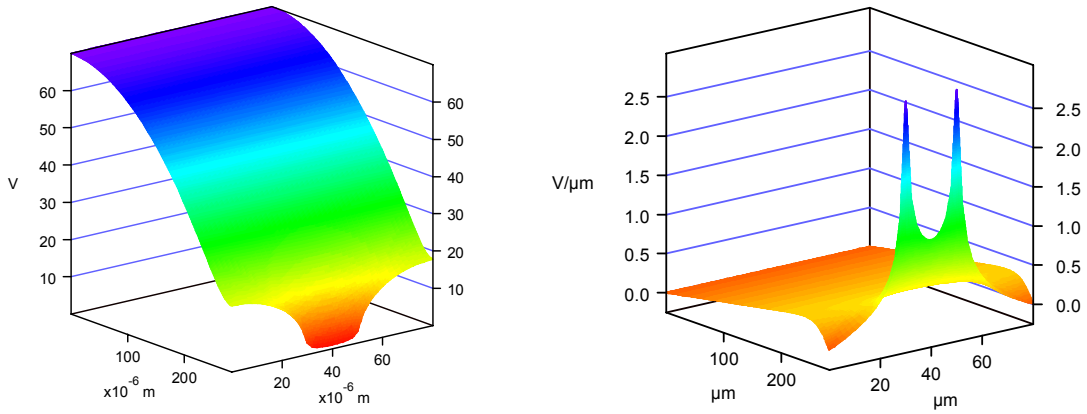

Electric potential Electric field

Figure 2 Electric potential and electric field for a 285 µm thick detector, with a strip width and a strip pitch respectively of 20 µm and 80 µm. The detector is operated right at its full depletion of 70 V.

4.2.2 The Weighting Field

The Weighting potential U_w as defined in Chapter 2, has to be calculated for each readout strip. It is the result of the equation (1) with N_{eff}=0 and with the boundary conditions:

- U_w=1 at the readout strip
- U_w=0 at the other strips and at the backplane
- $\partial U_w / \partial y = 0$ at the surface in the interstrip region
- $\partial U_w / \partial x = 0$ at the edges of the 2 outer strip pitches

Nevertheless a simulation of the detector with all the strips would require a very high CPU. Hence the simulation has to be limited over a segment of few strip pitches where the readout strip is the central one. Reducing to the region of a limited number of pitches such that its extension is large (about twice the detector thickness) has been shown to give a result that is less than 3% different respect to simulations on areas including two more external pitches. This criterion will be used for any further calculation of the weighting potential and is supposed to simulate central strips rather than external ones. An example of weighting potential and field calculated for a strip detector with the same geometry as the one shown in the previous paragraph is in Figure 3.

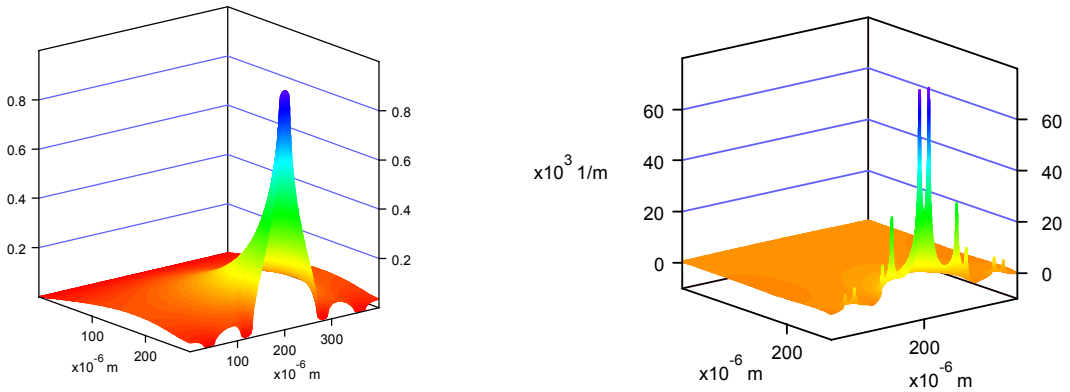

Weighting potential Weighting field

Figure 3 Weighting potential and weighting field for a 285 μm thick detector, with a strip width and a strip pitch respectively of 20 μm and 80 μm. In the next representations the microstrip detector will always have this geometry and depletion.

It can be noticed from the Figure 3 that for the given geometry the weighting potential at the readout strip is very high only in the region close to the readout strip. This means that most of the signal induced by the generated charge appears when this charge approaches the readout electrode.

4.3 Charge Transport

As we have seen in the Chapter 2, the complete calculation of the electric state of a semiconductor device requires the resolution of the current equations:

$$\begin{cases} \vec{J}_e = -\mu_n n_c(\vec{r})\vec{E} - D_n \vec{\nabla} n_c(\vec{r}) & \textit{for electrons} \\ \vec{J}_h = \mu_p p_v(\vec{r})\vec{E} - D_p \vec{\nabla} p_v(\vec{r}) & \textit{for holes} \end{cases} \tag{3}$$

and the continuity equations:

$$\begin{cases} \dfrac{\partial n}{\partial t}(\vec{r}) = U_{cn} - \vec{\nabla}\cdot\vec{J}_e & \textit{for electrons} \\ \dfrac{\partial p}{\partial t}(\vec{r}) = U_{cp} - \vec{\nabla}\cdot\vec{J}_h & \textit{for holes} \end{cases} \tag{4}$$

simultaneously to the Poisson's equation (1) where:

$$N_{eff} = p(\vec{r}) - n(\vec{r}) + N_d(\vec{r}) - N_a(\vec{r}) \tag{5}$$

This coupled non linear set of equation can not be generally solved in one step, but a non linear iteration method is required. Several common methods are generally used to solve the discretised equations, depending on the particular devices [5]. Nevertheless this simulation will mainly treat the case of fully depleted microstrip detectors with the assumption that the generated charge (both from ionization by high energy particles and from thermal emission from eventual traps) is negligible and the device is completely emptied of free carriers. This means that the perturbation of the free carriers on the local electric field will not be considered but only their induction on the electrodes through Ramo's theorem. In this way the electric field calculated resolving Poisson's equation numerically will be used to determine the drift motion of the free carrier following the equation (27) of Chapter 2. The trajectories will be represented in arrays whose elements for the 1D case are ruled by the following FD discretization of the motion law:

$$x_i = x_{i-1} + v\left(x_{i-1} + \frac{x_i - x_{i-1}}{2}\right) \cdot dt \approx x_{i-1} + v\left(x_{i-1} + \frac{v(x_{i-1}) \cdot dt}{2}\right) \cdot dt \tag{6}$$

with x_i the position occupied after a time dt starting from x_{i-1} with a velocity v. The time step dt is fixed and defines the resolution of the trajectory: the smaller is dt the smoother is the computed carrier trajectory. Hence for the motion of the free carriers in microstrip detectors, for each trajectory point the computation is done in three steps:

$$x_i^\alpha = x_{i-1}^\alpha + \Delta^\alpha \tag{7}$$

with

$$\Delta^\alpha = \pm\mu\left(q, T, E^\alpha\left(x_i^\alpha + dx_i^\alpha, x_i^\beta\right)\right) \cdot E^\alpha\left(x_i^\alpha + dx_i^\alpha, x_i^\beta\right) \cdot dt \tag{8}$$

and

$$dx_i^{\alpha} = \pm \frac{1}{2} \mu\left(q, T, E^{\alpha}\left(x_i^{\alpha}, x_i^{\beta}\right)\right) \cdot E^{\alpha}\left(x_i^{\alpha}, x_i^{\beta}\right) \cdot dt \qquad (9)$$

where the index ranges over the coordinates x and y.

The mobility model used in this simulation takes into account the local field dependence following the Canali [6] parameterisation combined with the constant mobility model [7] to describe the low field mobility that depends only on the lattice temperature.

In Figure 4 are shown selected hole and electron simulated trajectories from pairs generated along an ionised sagitta (green arrow) crossing the strip detector.

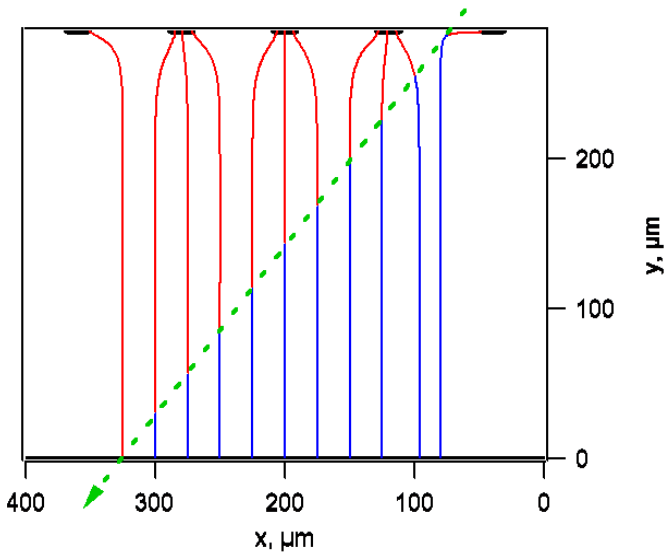

Figure 4 Simulation of hole (portion of lines over the oblique arrow) and electron (portion of lines under the oblique arrow) trajectories from pairs generated along an ionized track (oblique arrow) in a portion of detector. The trajectories correspond to a bias of 100 V.

4.3.1 The Drift-Diffusion mechanism

Together with the drift motion the carriers diffuse through the bulk. This is represented in the simulation with an additional contribution in (7):

$$x_i = x_{i-1} + \Delta_i + \Delta_i^{diff} \tag{10}$$

where Δ_i^{diff} is a randomly generated term that is distributed as a Gaussian in all directions, with the standard deviation depending on the diffusion coefficient, as seen in equation 37 of chapter 2:

$$\sigma_{e,h}^{diff} = \sqrt{2D_{e,h} \cdot dt} \tag{11}$$

An example of holes generated at the backplane and drifting and diffusing through the detector until they are collected at the electrodes is shown in Figure 5.

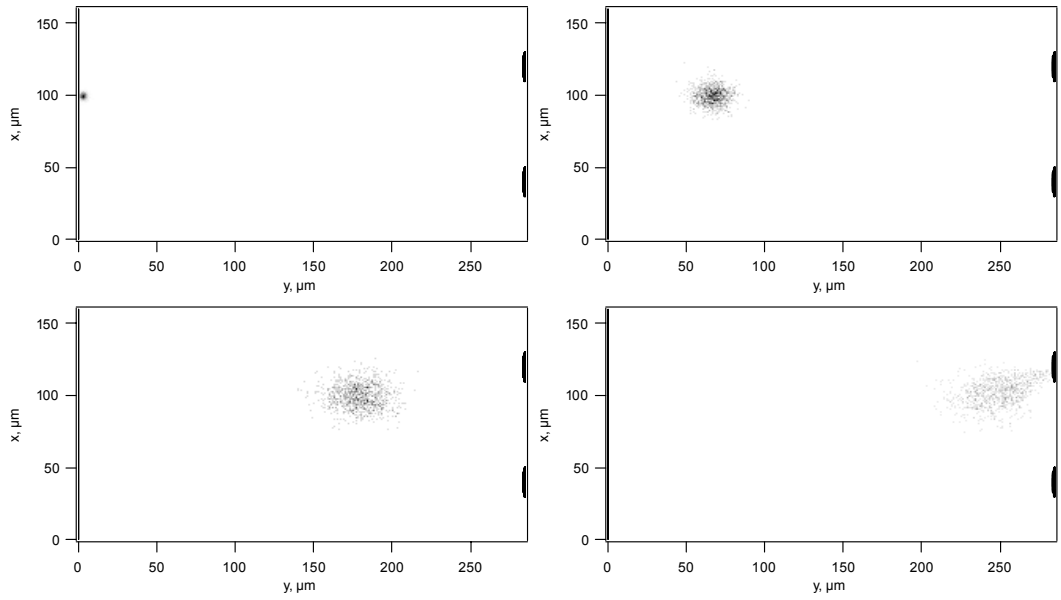

Figure 5 Drift and diffusion of holes injected at the back plane of a microstrip detector biased with 100 V, in four different moments: right after the injection (top left) after 12 ns (top right), after 23 ns (bottom left) and after 32 ns (bottom right) when the holes starts to reach the strip electrodes.

4.4 Signal Induction

Ionizing radiation crossing the detector generates a continuous track of electron-hole pairs. The motion of these carriers towards the electrodes induces a

current that Ramo's theorem predicts to be proportional to the weighting field. In the simulation only mip radiation has been considered and the continuous track of pairs has been discretised over a linear mesh running along the ionized track. On each mesh point is assigned a constant number of generated electrons and holes equal to the density of generated pairs. A detailed simulation of ionisation in the matter due to radiation can be done using the tool GEANT [8] but this would go beyond the objectives of this thesis.

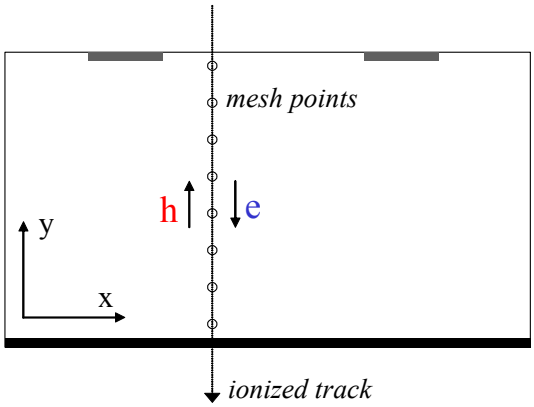

Figure 6 Schematics of the mesh points along the ionised track.

The motion of each generated carrier induces a current on the electrodes. The elements of the array giving this single carrier induced current are given by:

$$\frac{i^j}{q} = -\vec{v}\left(\vec{r}_j\right) \cdot \vec{E}_w\left(\vec{r}_j\right) \qquad (12)$$

where the $\vec{r}_j$ is the position assumed by the carrier after j times dt as described in the previous section, q is the carrier charge and $\vec{v}$ and $\vec{E}_w$ are respectively the punctual velocity and weighting field.

The total current is given by:

$$I^j = \sum_{mesh\ point} \left(\sum_{electons} i^j + \sum_{holes} i^j \right) \qquad (13)$$

where the internal sums are respectively over the electrons and the holes generated at each mesh point and the external one is over all the mesh points.

4.4.1 *Signal in Microstrip Detectors*

Given the weighting field in microstrip p^+-n-n^+ detectors, the current signal for mip radiation crossing the readout strip will always be unipolar and positive and will turn to bipolar as the radiation approaches the adjacent strips. Calculations of the mip signal at different volts are shown in Figure 7.

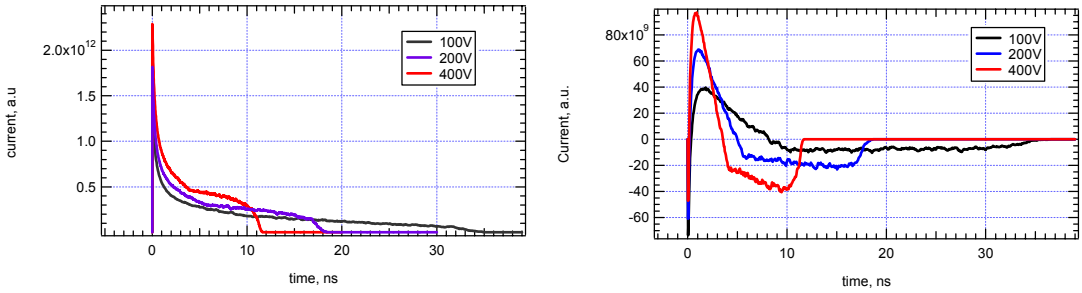

Figure 7 Mip current for radiation crossing the readout strip (left) and for radiation crossing at the adjacent strip.

The integrated charge is equal to the number of generated pairs for radiation crossing at the readout strips and is vanishing at the adjacent one. Between these two values the charge varies smoothly depending on the diffusion hence, on the voltage and detector thickness, with a crosstalk of 50% at the middle of interstrip gap. In Figure 8 Is shown the charge collected for radiation crossing the strip detector in the region between the middle of the readout strip and the middle of the adjacent one.

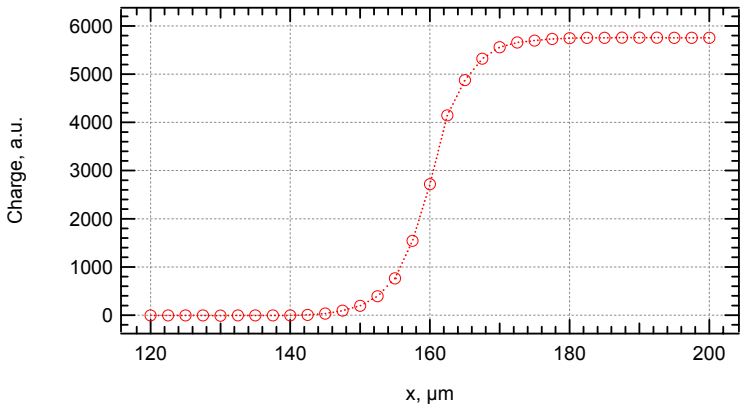

Figure 8 Evolution of the charge collection when the radiation moves from the middle of the adjacent strip (x=120 µm) to the middle of the readout strip (x=200 µm).

4.4.2 Electron Vs Hole signal

An interesting feature of the charge collection in microstrip detectors is the different contribution coming from the electron and holes. In fact as a direct consequence of the shape of the weighting potential there is always a carrier who prevails in inducing the signal. This can easily be seen also from their contribution to the current as shown in Figure 9.

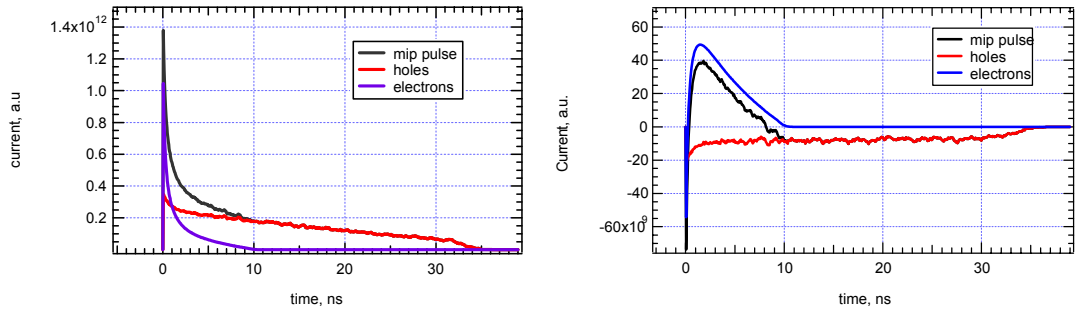

Figure 9 Mip current for radiation crossing the readout strip (left) and for radiation crossing at the adjacent strip with the detector biased at 100 V. In the two cases the different contribution from holes and electrons is shown.

A detailed behaviour of the ratio of charge induced by the electrons and holes Q_e/Q_h is shown in Figure 10 where three different areas are distinguished: the one centred at the readout strip and extending almost one pitch, where the ratio has a value depending on the geometry of the microstrip detector, right after the midgap, for an extension depending by the diffusion of the carriers, where the ratio diverges due to the vanishing charge induced by holes and, then at the strip adjacent to the one readout where the contribution of the two carriers is the same but of opposite sign.

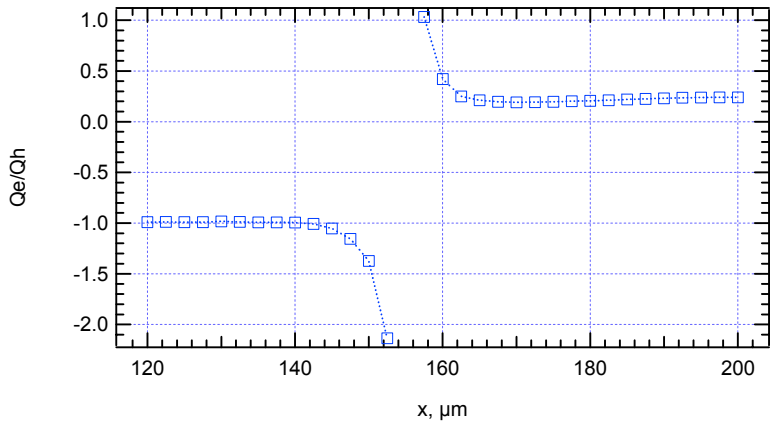

Figure 10 Ratio of charge induced by electrons to charge induced by holes for mip radiation crossing the microstrip detector from the middle of the adjacent strip (x=120 µm) to the middle of the readout strip (x=200 µm).

4.5 Signal induction in Irradiated Detector

As seen in the previous chapter p^+-n-n^+ detectors irradiated to a fluence over 10^{13} cm^{-2} of equivalent1 MeV neutrons undergo a space charge inversion and then increase their N_{eff} with the dose that at high doses comports a very high bias to fully deplete the device. Nevertheless in this simulation the irradiated detectors will be always considered fully depleted, and their depletion at different dose will be extrapolated from measurements that will be described in detail in the next chapter. An example of potential and electric field for a microstrip detectors irradiated to $1.7*10^{14}$ $_{24GeV}$ proton*cm^{-2} is shown in Figure 11.

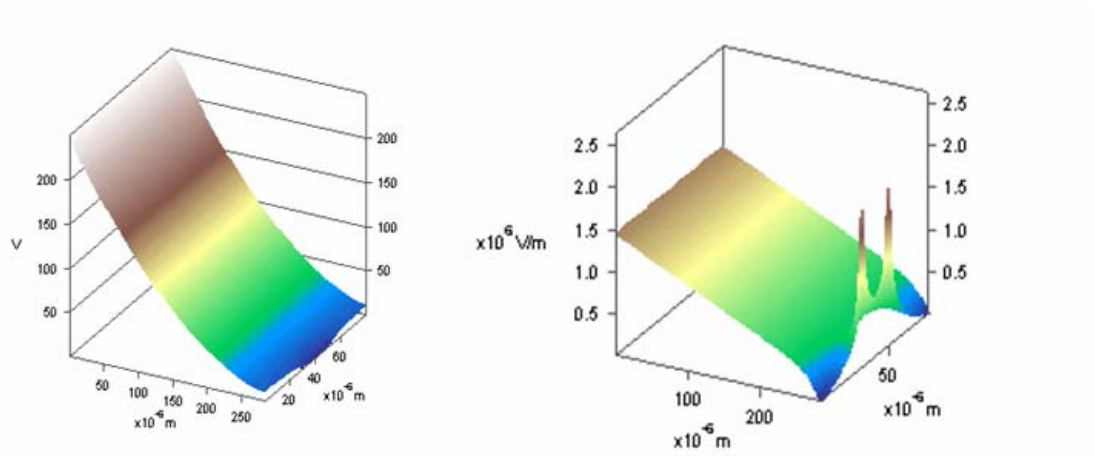

*Figure 11 Electric potential (left) and electric field (right) for a microstrip detector irradiated to $1.7*10^{14}$ $_{24GeV}$ proton*cm^{-2} over a region of one pitch centred in the middle of the strip. The detector is overdepleted (V_{fd}=200) with a bias of 250V.*

4.5.1 The Trapping Mechanism

As already seen, carriers trapping affects dramatically the charge collection in highly irradiated silicon detectors. In this simulation the trapping mechanism is produced by arresting the motion of each carrier at a time $\bar{t}_{trap}$ where $\bar{t}_{trap}$ is randomly generated along a logarithmic distribution that decays with the carrier's trapping time. Once arrested, the carriers stop contributing to the signal formation, also for long electronics shaping times. The carriers' trapping times used in the simulation have been extracted from [9]. An example of mip signal at the readout strip and at the adjacent one is shown in Figure 12

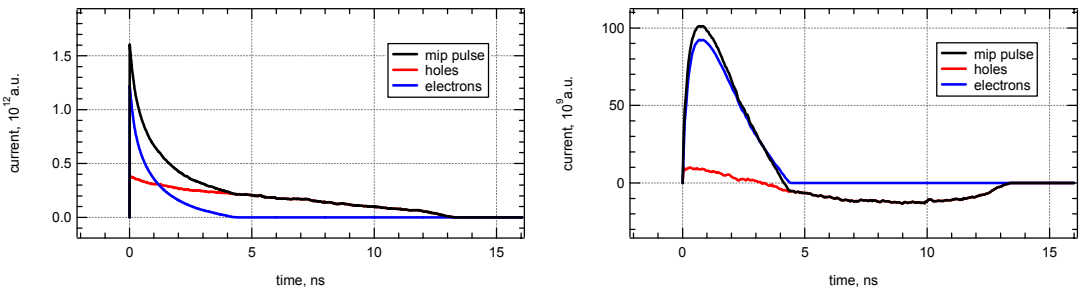

*Figure 12 Current induced at the strip crossed by radiation (left) and at the adjacent strip (right) for a detector irradiated at $1.7*10^{14}$ $_{24GeV}$ proton*cm^{-2} and biased with 250V. In the two cases are also shown the different contributions from holes and electrons.*

Taking place the carriers trapping, even for depleted detectors, there is a charge collection that is not vanishing for radiation crossing strips close to the one readout. Moreover for radiation crossing the readout strip the charge collected is not completed. Nevertheless the bias can increase the charge collection reducing the carriers' time of flight and therefore their probability of being trapped.

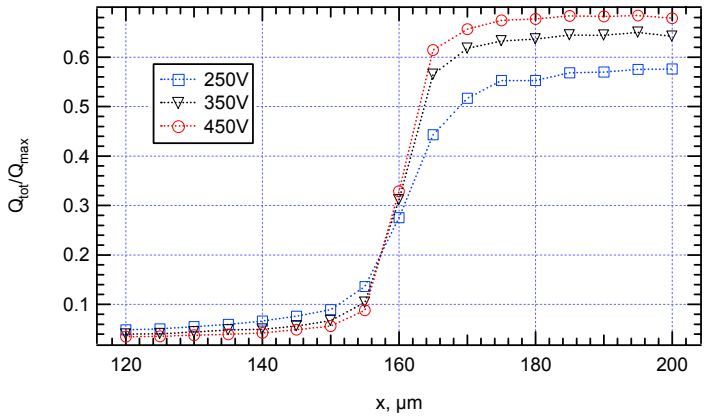

Figure 13 Charge collected for mip radiation crossing the detector along one pitch, starting from the middle of the strip adjacent to the one readout up to the middle of the readout strip, for different bias bigger than the full depletion voltage (200 V). The collected charge is normalized to the maximum charge collected in absence of trapping.

4.6 Charge collection in highly irradiated detectors

In order to study the charge collection behaviour with voltage bias, the strip detector of the geometry under study (thickness of 285 :m, strip pitch of 80 :m and strip width of 20 :m) is been simulated for two different absorbed doses: $1.7*10^{14}$ $_{24GeV}$ proton*cm^{-2} and $4*10^{14}$ $_{24GeV}$ proton*cm^{-2}. For these two doses the full depletion bias is respectively 200 V and 400 V. Also in this case we anticipate here a result obtained in this thesis work and that will be showed in the next chapter. Assuming the case of mips crossing the detector perpendicularly in the centre of one strip the charge collected at the same strip increases with increasing voltage bias for these two doses, as shown in Figure 14.

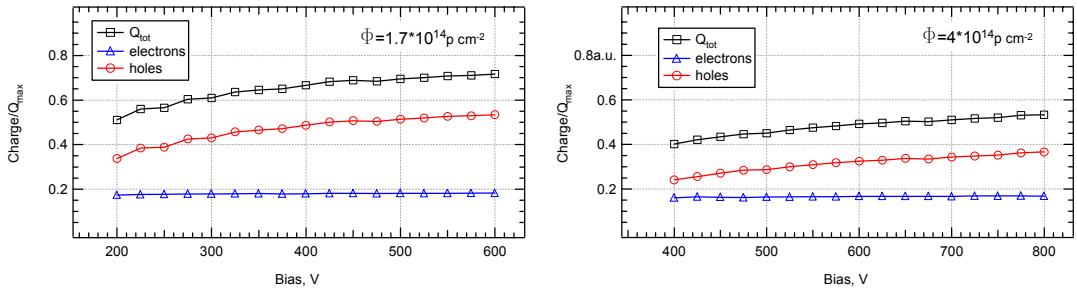

*Figure 14 Behaviour of charge collection (Q_{tot}) with bias voltage for a fluence of $1.7*10^{14}$ $_{24GeV}$ proton*cm^{-2} (plot on the left) and $4*10^{14}$ $_{24GeV}$ proton*cm^{-2} (plot on the right). The bias voltage range starts in both cases with the full depletion voltage and the values of the charge are normalised to the maximum charge collected in the case of non irradiated detector. Also the separated contribution coming respectively from electrons and holes are shown.*

In Figure 14 is shown also the separated contributions from electrons and holes. For both doses the contribution of electrons seems to be less affected by the voltage bias increase, while for holes the collection increases in all the investigated range.

It is also interesting to see how the ratio of the charge signal at the adjacent strip (Q_{strip2}) with the charge signal at the strip (Q_{strip1}) hit by perpendicular mips decreases with increasing bias. For the case of $1.7*10^{14}$ $_{24GeV}$ proton*cm^{-2} this ratio can be set to less than 0.05 if the detector is operated with a bias voltage of at least 450 V. For the higher dose this ratio is bigger at a given voltage bias. Nevertheless Q_{strip2}/ Q_{strip1} can achieve a value lower than 0.10 with a voltage bias of at least 600 V.

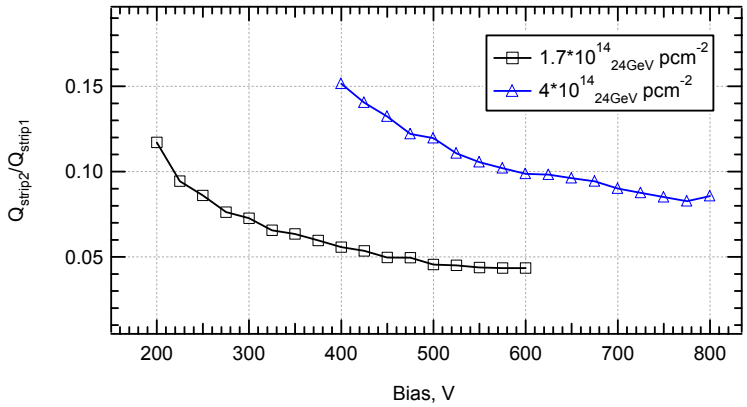

Figure 15 Ratio of the charge collected at the adjacent strip (Q_{strip2}) over the charge collected at the strip through which a charge uniformly is generated (Q_{strip1}).

4.7 References

[1] http://www.wavemetrics.com/Products/IGORPro/IgorPro.html

[2] R.H. Richter et al., Nucl. Instr. Meth. A377 (1996) 412

[3] P. Ciampoli et al., Nucl. Instr. Meth. A473 (2001) 178

[4] V.H. Press et al., *Numerical Recipes in C*, Cambridge University Press (1992)

[5] S. Selberherr, *Analysis and Simulation of Semiconductor Devices*, Springer-Verlag, 1984

[6] C. Canali et al., IEEE Trans. on Electron Devices, ED-22 (1975) 1045

[7] C. Lombardi et al., IEEE Trans. on CAD, 7, no 11 (1988) 1164

[8] For example see http://geant4.web.cern.ch/geant4/

[9] G. Kramberger et al., Nucl. Instr. Meth. A476 (2002) 645

5 Transient Charge/Current Technique Experimental Setup

The concept and realisation of the automated system is explained in this chapter. The basic idea is to replace short range particles and mips that require a complicated system of focusing and triggering by lasers suitable for free carrier generation either at a shallow depth or almost uniformly through the detector. This setup has been exploited to measure several relevant parameters concerning the charge collection in microstrip detectors. At the end of the chapter a method is described for the evaluation of the full depletion voltage in irradiated silicon detectors.

5.1 Physics Principle

Silicon detectors cover large areas in trackers for modern high energy physics experiment. These sensors require to be tested before being installed in the experimental area. Many groups [1] [2] [3] [4] have used IR laser set-ups in the past to perform quality assurance tests (bonding check, fast signal response of the readout electronics etc.) as well as charge collection studies. The almost uniform penetration through hundreds of microns in silicon, combined with the easy rate and position control of laser beams makes the IR laser an excellent tool for this purpose, especially if compared to minimum ionising particles that require complicated set-ups for precise beam focusing and triggering.

As described before, the working principle of silicon detectors is based on the collection at the electrodes of the charge carriers generated by charged particles crossing the detector, thanks to the presence of an electric field. In the same way, absorbed photons at optical frequencies can generate electron-hole pairs in the silicon. The minimal energy required is given by the bandgap. The intensity of the laser pulse penetrating in the silicon decreases exponentially as it goes through the silicon, due to the absorption, following the law:

$$I_{\omega}(x) = I_{\omega 0} e^{-\alpha_{\omega} x} \qquad (5.1)$$

where α_{ω} is the absorption coefficient at the frequency ω and $I_{\omega 0}$ is the initial intensity. Hence the density of pairs generated through the silicon is:

$$\rho(x) = \frac{\alpha_{\omega} I_{\omega 0}}{E_g} e^{-\alpha_{\omega} x} \qquad (5.2)$$

where E_g is the bandgap energy.

As the wavelength gets shorter the photon absorption rate increases and for visible light, with photon energies bigger than the silicon bandgap, “full” absorption is realised in the first few microns of silicon. The signal readout in this condition carries relevant information on the electric field inside the detector. Figure 1 shows the absorption spectra of single crystal silicon at 77 K and at 300 K

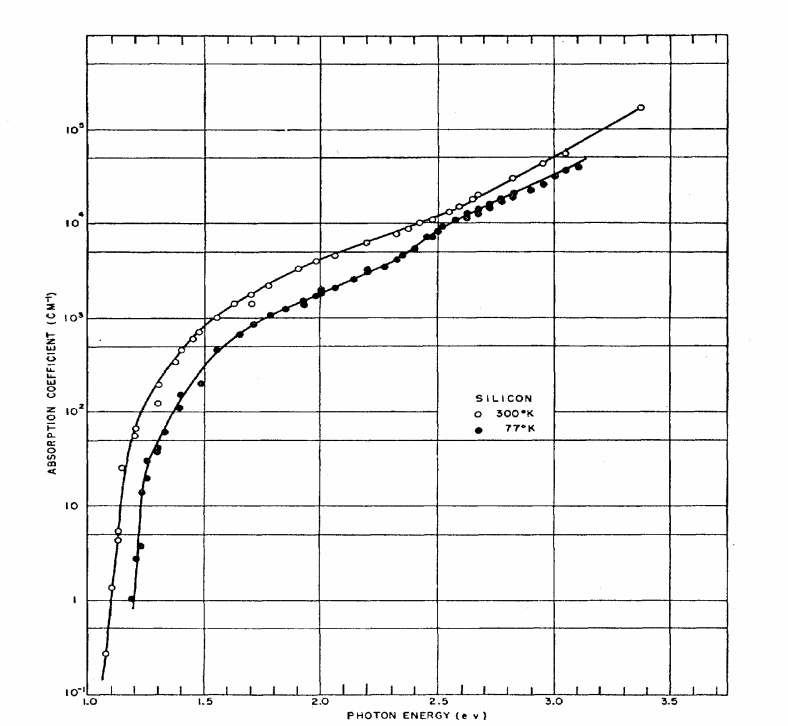

Figure 1 Absorption spectra of single crystal silicon at 77 K and at 300 K [5].

As we have seen in the previous chapter, for highly irradiated silicon the electric properties of the material change and so does the electric field. A coordinated analysis of the charge/current pulses due to focused IR and Red lasers turns to be an excellent tool to study the behaviour of silicon devices.

5.2 Experimental Set Up

In Figure 2 is shown the laser setup developed in this thesis. Its detailed description and functionality will follow in this section.

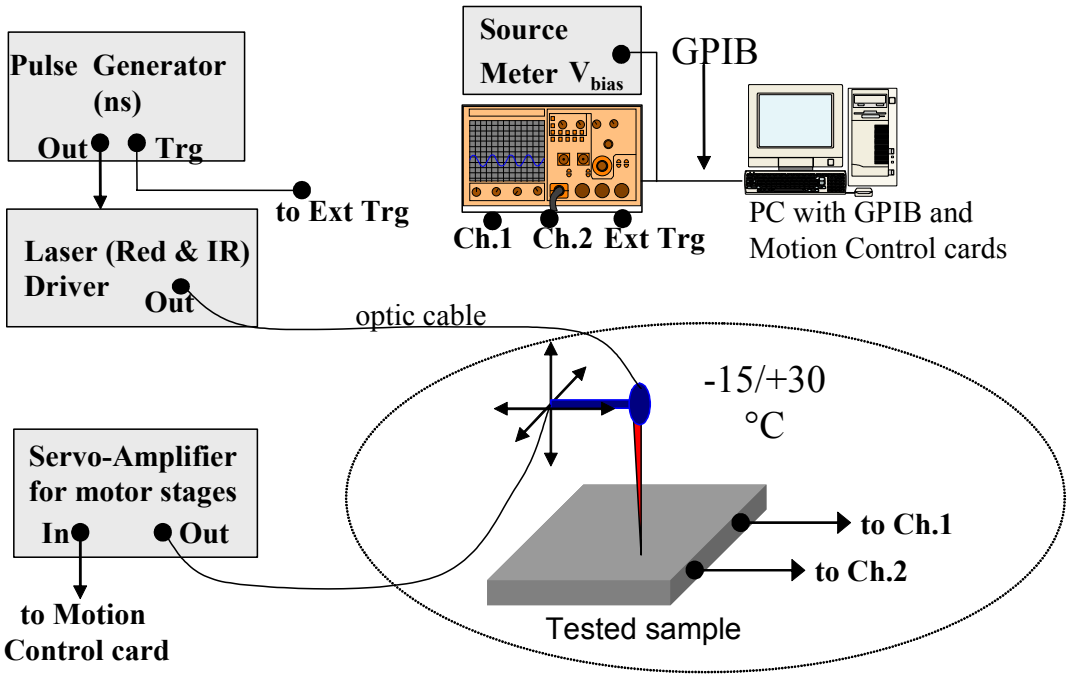

Figure 2 Schematic of the entire laser setup.

5.2.1 Optics

To generate carriers in the detector, two different lasers were used: a red one (wavelength of 660 nm and penetration depth of ~3 μm in the silicon at room temperature) and an infrared one (IR-laser) (wavelength of 1060 nm and penetration depth of ~400 μm) [5]. The density of the pairs generated through the bulk for these two working wavelength is shown in Figure 3.

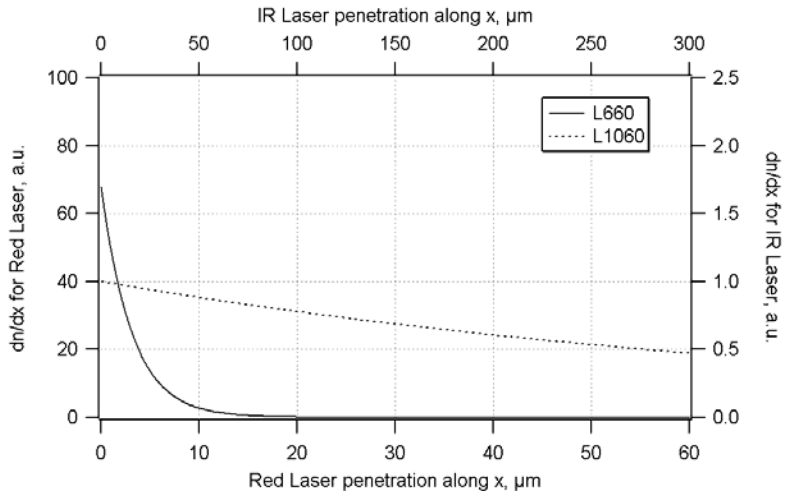

Figure 3 Generated pairs' density through the bulk for the two working wavelength: the red laser at 660nm (full line) and the infrared at 1060nm (dashed line).

The two lasers are triggered by a nanosecond pulse generator and the laser diode coupled to an optical fibre which is terminated with a focusing lens.

The nanosecond pulse generator output feeds in the laser driver, while the trigger output is used to select the signal from the detector at the oscilloscope. The pulse generator can generate voltage pulses with amplitude up to 2 V, matching the requirements of the laser drivers (both the IR and the Red). This signal is required to pump the laser diode electrically. For both wavelengths, the optical output power is ~1 mW

For the IR laser the time characteristic of the signal is regulated and measured with a TIA-950 Optic/Electric converter produced by Terahertz Technology Inc.[6].

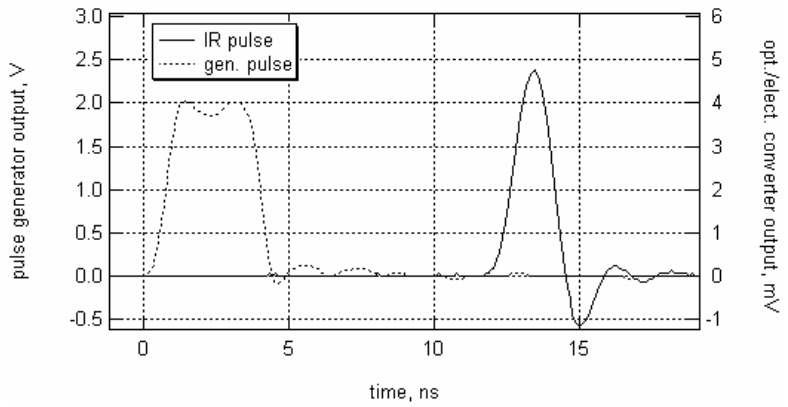

Figure 4 Electric output from the pulse generator (gen. pulse in the legend) feeding the IR laser and the corresponding signal from the O/E converter (IR pulse in the legend)

The laser pulse width selected was 2 ns (see Figure 4) and the rise time 1.5 ns. The rise time defines the time resolution of the TC/ChT system.

The optical fibres are single mode to achieve a better focusing and reduce the time spread of the light pulses through the light guide. With a core diameter of 9 μm at the end of the optical fibres a 12 mm focal length lens directs the light on the device under investigation.

On the silicon detector surface the laser light converges to a light spot and is then mainly refracted inside the detector. Thanks to the refractive index of 3.4 of silicon, the propagation of the light rays will be closer to the normal of the surface with respect to incident light, guaranteeing that the ionisation is in an almost cylindrical volume as for mip's ionising tracks. Nevertheless the latter have a diameter of only few microns [7], comparable with the minimum laser spot achieved of ≈ 10 μm. A detailed description of the laser spot will be given in a later section.

5.2.2 Electronics

The experimental set-up includes the 12V DC power supply for the amplifiers the means to set the detector operational mode and a high frequency part to measure the detector response to the light injected carriers.

The DC part used a Keithley 2401 Sourcemeter to bias the detector. This device allows computer-controlled operations.

The detector signal is read out with a fast current amplifier HP MSA-0886 with low input impedance (50 Ohm) mounted on a PCB as recommended in the

manufacturer's instructions. This amplifier has a usable gain up to 5.5 GHz. The typical gain is of 32,5 dB at 0.1 GHz and 22.5 dB at 1.0 GHz. At the latter frequency the noise figure is 3.3 dB. The amplified signal was digitised and integrated by a LeCroy 334A (0.5 GHz) sampling oscilloscope. The current signal read at the scope is in Volts and the charge signal extracted integrating in time is in Vs.

5.2.3 Mechanics

In order to control the laser position, a structure of of 3 stages has been made. In this structure three motorised linear stages have been assembled together, with motion in orthogonal directions. Each of them has a travel range of 25mm. The motors incorporate a magnetic encoder. The resolution for each stage is 0.5 μm with accuracy of ±0.1 μm- per 25 mm of travel. The power for the motor and the encoder is supplied by a multi-axis servo amplifier system. This device and the motorised stages have been produced by National Aperture [8]. Furthermore, the servo amplifier system interfaces a PC card for motion control issued by National Instruments [9].

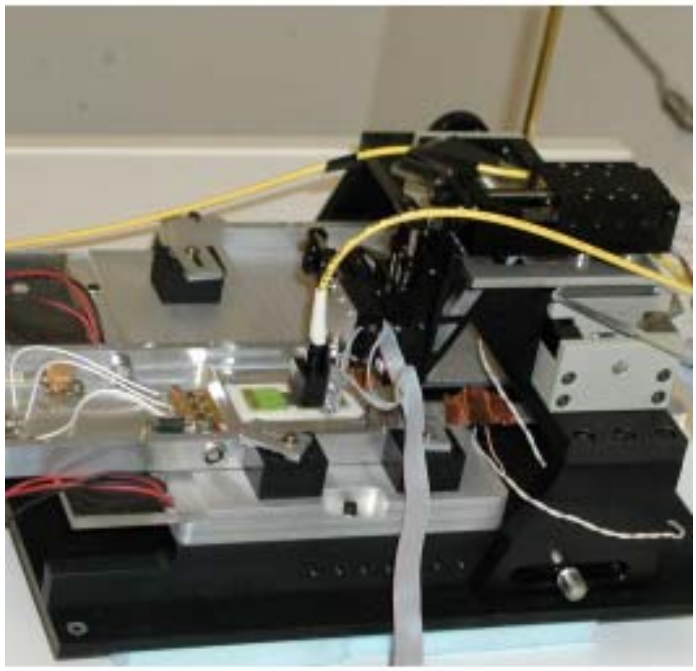

Figure 5 Picture of the three motorised stages with the laser pointing towards the detector.

5.2.4 Software Control

Several application software packages, written with the programming language LabView 6*i* [10], link the oscilloscope and the Sourcemeter with a PC via a GPIB bus (IEEE 488) and allow repeated measurements at different voltages with the signal response stored on the PC hard disk. Other applications were developed to provide PC control of the movement. In this way it was possible to perform automated measurements repeated at different points, driving scans over the detector's surface as well as optimising the distance of the lens from the detector to achieve a minimal diameter of the laser spot.

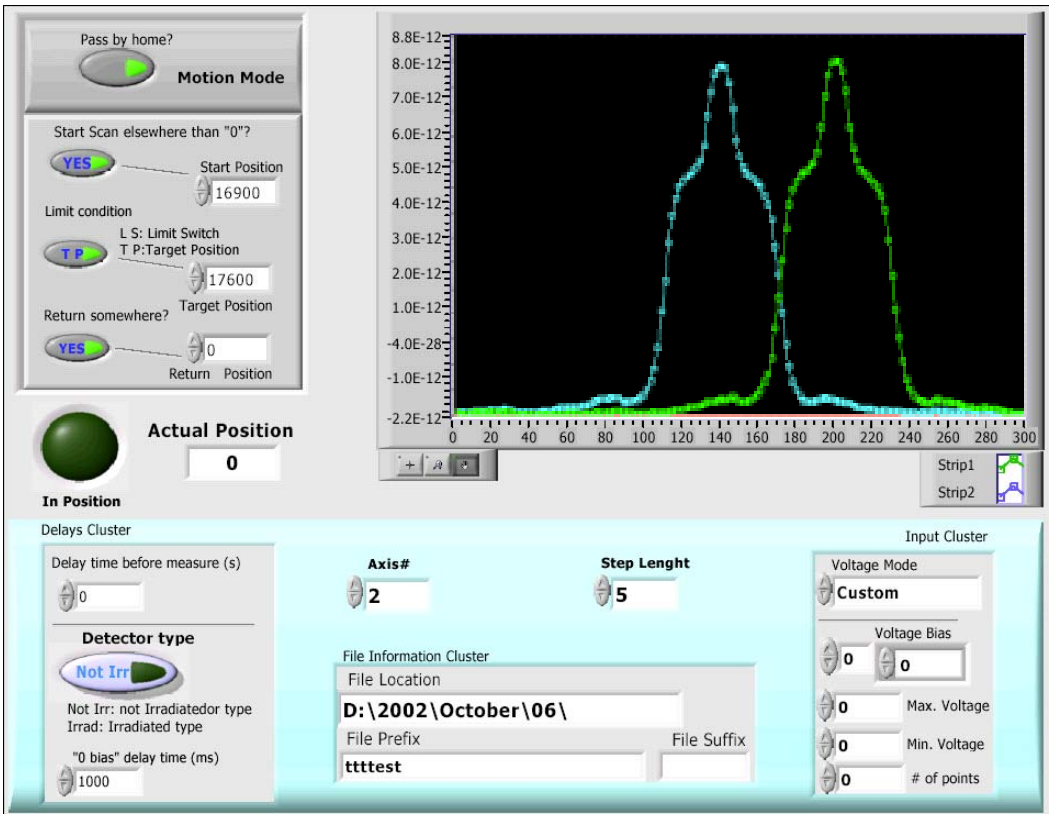

Figure 6 Control panel of one of the programs for the automatic control of the setup. The internal picture represents charge measurement scan over two adjacent strips and read by the amplifiers on the same strips. The signal is due to an IR laser illumination from the back.

5.3 Measurements and Characterisations

The following paragraphs describe some operations that have been carried out with this system. The sample used in this study is a 10 x10 mm^2 *baby detector* copy of the full-sized microstrip vertex detectors designed for the ATLAS experiment in terms of the bias, guard-ring and edge design, but with only 98 strips (+2 edge strips). The *baby detectors* have been processed on 285 μm thick, n-type high resistivity (4kOhm cm) silicon wafers. The details of the detector design are given in [11]. The strip pitch of the detector is 80 μm and the strip width (p^+-implant) is 18-20 μm. The aluminium contact is capacitively coupled over the p^+-implant strip. Each strip (p^+-implant) is biased through a 1.25 MOhm polysilicon resistor. On the back plane, in the middle of the aluminium metallisation that initially entirely covered the n^+-implant, a circular window with a diameter of 5 mm was etched to allow carrier generation by laser as well as to avoid reflection. A simplified diagram of the detector's cross-section is shown in Figure 7, which also indicated several points used to describe the experiment in the next paragraphs.

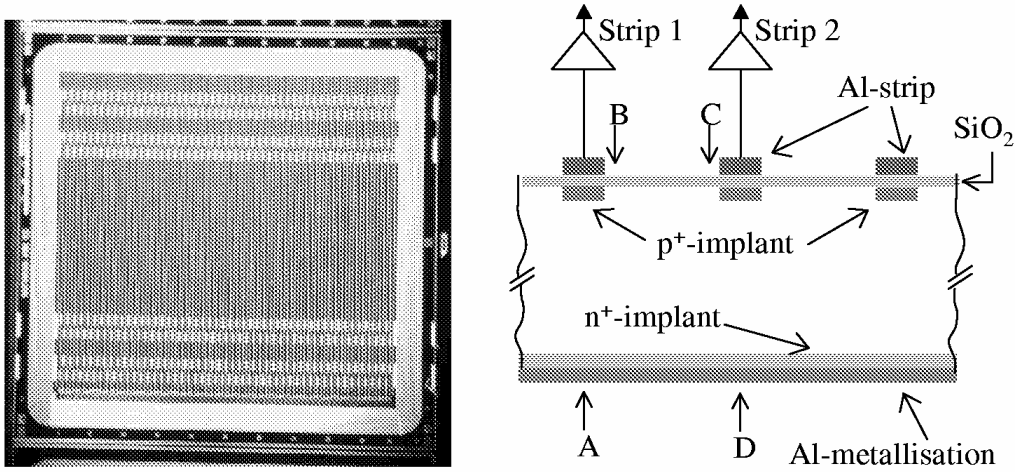

Figure 7 Picture of a baby microstrip detector (left) and schematic cross-section of the device (right).

5.3.1 Laser spot (LS)

The evaluation of the laser spot (LS) amplitude is necessary to interpret the result of the measurements correctly. To achieve the optimal spatial resolution in the set up, the laser spot should be as small as possible. This check is the first to be performed when a detector is positioned beneath the laser. For this operation the optimal position of the lens respect to the detector is given by the signal read by the detector under inspection.

The lens shape dominates the profile of the LS. The lens being circular, the diffraction pattern that comes out of it is a set of concentric disks of light separated by dark rings. In the central disk (Airy's disk) contains more than the 84% of the total light coming out of the lens [12]. The diameter of the Airy's disk is what we consider as the LS diameter. Scanning the detector surface with a laser going from a region where metallisation is present to an active region without metallisation the charge collection will rise. Hence a conservative estimation of the Airy disk diameter is the distance from the 5% to the 95% of the full charge signal. The following picture shows the evaluation of the LS scanning across a metallised strip of a microstrip detector showing a diameter of (10.0±2.5) μm.

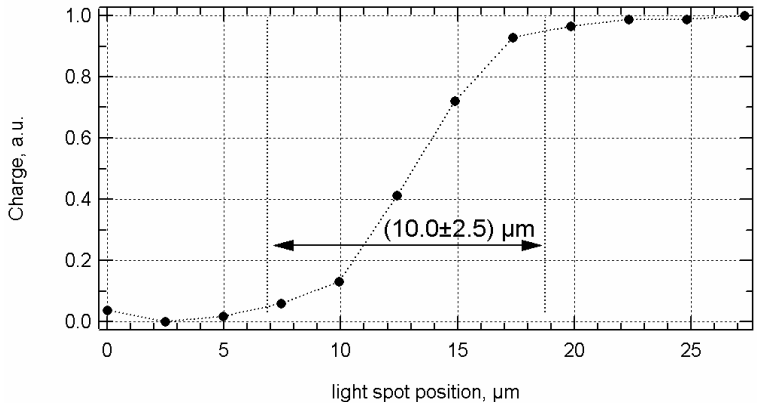

Figure 8 Measurement of the laser beam spot on the silicon detector.

5.3.2 Infrared absorption in silicon

With this system it is also possible to estimate the absorption coefficient when the light penetration depth exceeds the detector thickness. This is possible by illuminating the detector from the n^+-side pointing the laser around the strip axis (point A for strip1 in Figure 7), starting off the strip axis at a distance greater than the

laser spot diameter and scanning up to the centre strip axis. The absorption is evaluated by comparing the charge collected at the point where the light pulse traverses the detector completely and where the light is reflected and therefore generate twice the charge. At these two points the charge is respectively the charge collected when the IR laser travels once, *Ch(d)*, and twice, *Ch(2d)*, through the detector bulk.

As the collected charge is proportional to the absorbed light intensity (cf. eqn. *(4.1))* the absorption coefficient for the infrared laser is given by:

$$\alpha = \frac{1}{d}\ln\frac{I(d)}{I(2d)} = \left(\frac{1}{.03}\ln\frac{.43}{.95}\right)cm^{-1} = 26cm^{-1} \qquad (5.3)$$

in agreement with published data in [5].

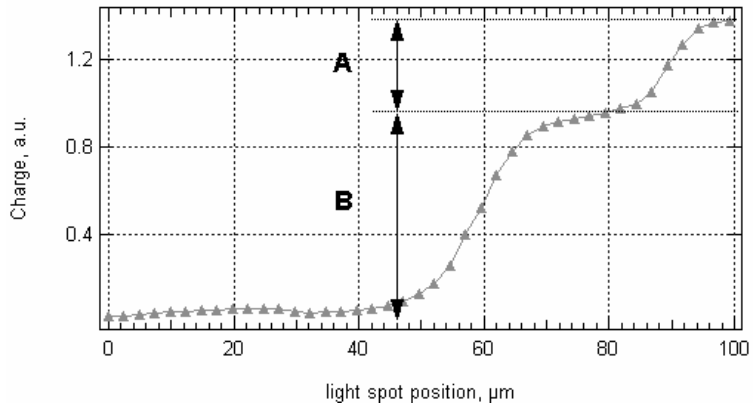

Figure 9 Measurement of the IR absorption in the silicon detector. The amplitude B is proportional to the light intensity after a travel length of one detector thickness, while A is proportional to the light intensity after two travel lengths.

5.3.3 Charge Collection studies

Given our set up, charge collection studies could be done by integrating in the oscilloscope the output pulses of the used current amplifiers over specific time intervals. In order to make these studies with laser comparable to charge collection with mips, the laser intensities have been appropriately regulated. As seen in the Chapter 2, mips generate in silicon an amount of electron-hole pairs that distributes following a Landau statistics with the most probable value of generated pairs in 300 μm of silicon of ~25000. Nevertheless to work with a good signal to noise ratio in

our setup it was necessary to generate with laser an amount of charge equivalent to 4 times the peak of a mip signal that, given the current amplifiers used in the setup with an average gain of G=30 at the working bandwidth, corresponds to a measured charge signal of 25 pVs. Nevertheless this still makes our system very close to one using mip particles to test silicon detectors. In fact, for IR laser, this amount of generated charge can be compared to higher energetic events at the Landau tail while for red laser the charge cloud is not such to have plasma screening effects that would increase the collection time. Here follows the picture of the charge collection at two different light intensities, comparing two shaping times.

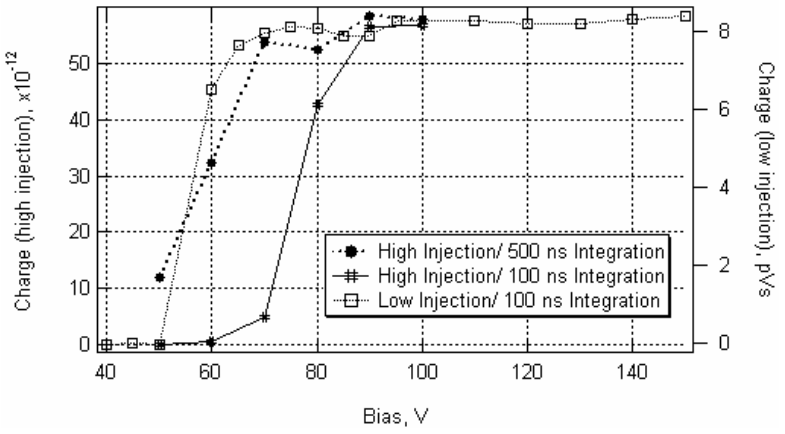

Figure 10 Charge collection vs. voltage for different injection amplitudes and different integration times for red laser illuminating on the back side.

5.3.4 Full depletion studies

The full depletion for non irradiated segmented detectors can be evaluated illuminating the detector at the point A or C in Figure 11 and measuring the charge collected at the indicated strip as function of the voltage.

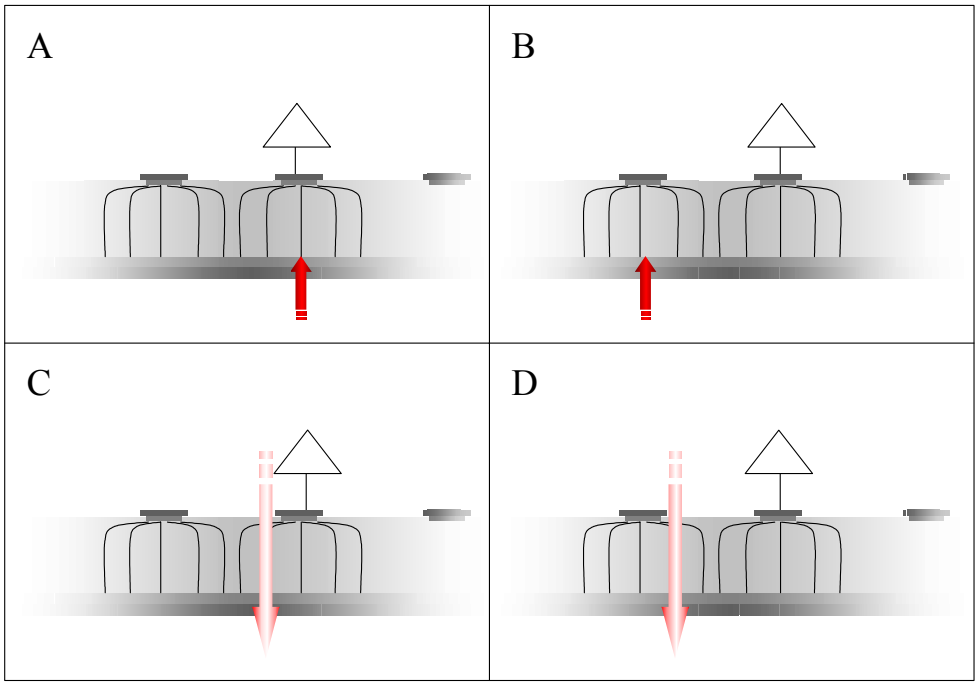

Figure 11 In these four different cases are described for different type of test to study the full depletion in microstrip detectors.

The saturation of these curves will give the full depletion voltage. The charge measured at other strips in this study is compatible with zero. In fact in these cases the current signal readout at the adjacent strip is bipolar and the integrated charge over the full collection time vanishes. This is well explained in the context of Ramo's theorem, where the charge induced on the electrode by a charge moving between two points is simply given by the product of the charge itself with the difference of the weighting potential at the two points (cfr. eqn. (45) in Chapter 2 and see also Figure 16).

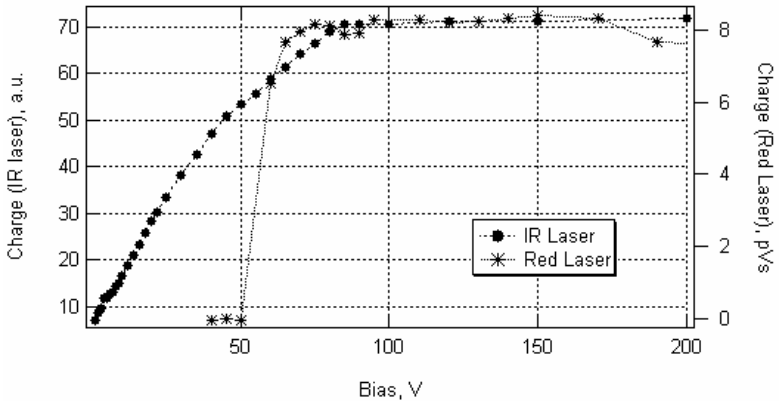

Figure 12 Full depletion measurement on a non-irradiated sample.

For irradiated detectors[1] the changes happening in the material complicate the interpretation of the curves of charge vs voltage. At a fluence of $1.7*10^{14}$ cm^{-2} (24GeV) protons, which is the lowest dose investigated in this study, the IR and red laser responses still retain many similarities, but they look completely different from those at zero dose. These data are presented in Figure 13. The data taken with IR following the case C of Figure 11 show an initial linear growth rate and then an "exponential" trend towards saturation from 200 V. The data taken with IR illuminating at the adjacent strip, (case D), are no longer vanishingly small and follow a linear increase first and then an "exponential" decrease that also seems to saturate at 200 V. Concerning the measurements of the charge induced by injecting holes with the red laser, the charge vs. voltage curves show a behaviour generally similar to that measured with IR but with a few differences:

- Where the data in the case C (IR laser) seem to saturate, the case A (red laser) seem to show a higher margin of growth for higher voltages
- Comparing the data from cases B and D the maxima are reached at different voltage, i.e. respectively around 60 V for the red laser and around 100 V for the IR laser.
- In contrast with the data taken with the IR laser, the initial rate of increase is the same for those with the red laser.

[1] For the studies done in this thesis, all irradiated detectors have been kept for the first 10 days after the irradiation at room temperature and then have been stored at -15°C.

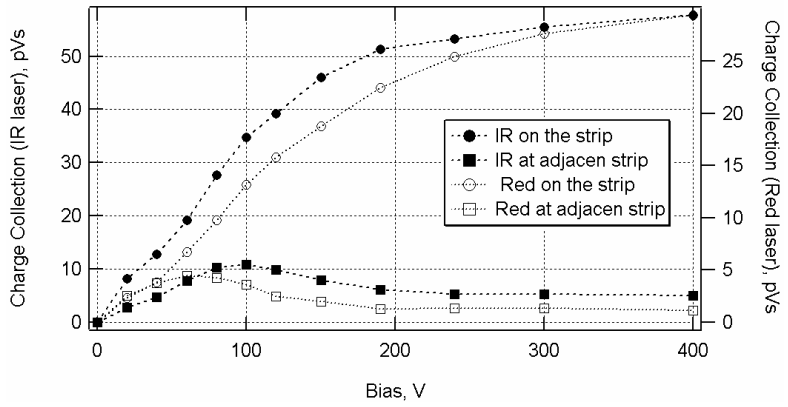

*Figure 13 Charge collection for the sample irradiated at 1.7*10^{14} cm^{-2} (24GeV) protons measured following the different schemes presented in Figure 11.*

At a dose of 4*10^{14} cm^{-2} (24GeV) protons, the charge collected vs. bias shows the similar behaviour to that at lower fluence, with the difference that for each curve, a given value of collected charge requires almost the double of the potential required for the sample at lower dose. These data are shown in Figure 14.

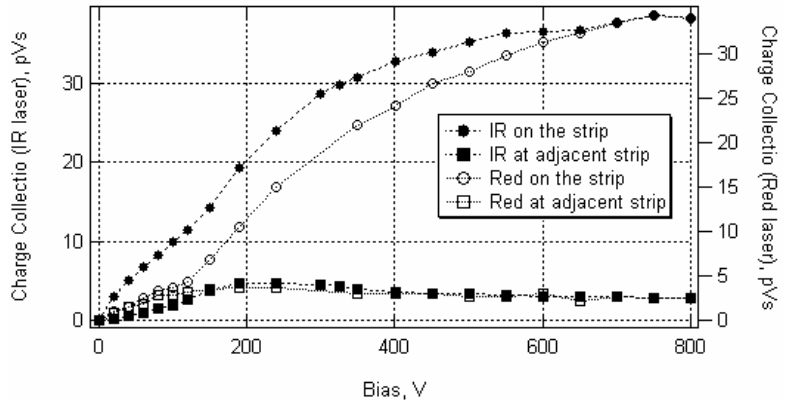

*Figure 14 Charge collection for the sample irradiated at 4*10^{14} cm^{-2} (24GeV) protons measured following the different schemes presented in Figure 11*

At the dose of 1*10^{15} cm^{-2} (24GeV) protons, the behaviour of the charge collected vs. bias changes dramatically with respect to that measured at lower doses. The first striking feature is the absence of signal for red laser illumination of the backside, in the bias range up to 900 V. The IR signal at the two points, on the other hand, grows linearly with the bias. This is exactly like the data at lower dose, in the first bias range. Nevertheless the limited range of the bias supply prevented

measurements beyond the range of linear growth of the charge collection, to check if this behaviour would end with saturation. The IR data are shown in Figure 15.

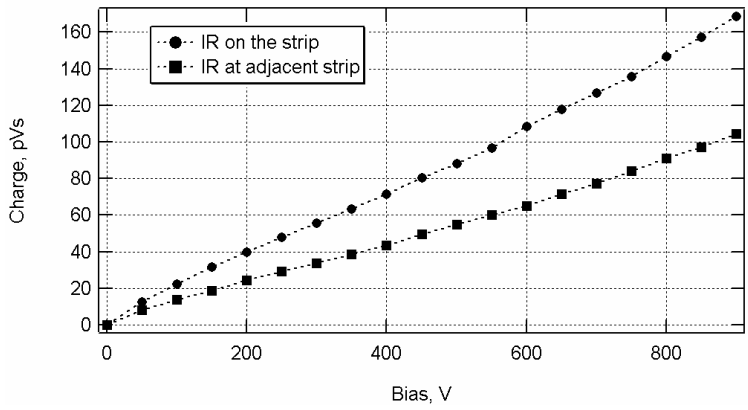

Figure 15 Charge collection for the sample irradiated at $1*10^{15}$ cm^{-2} (24GeV) protons measured following the different schemes presented in Figure 11.

Discussion of the Data

In a non irradiated detector operated at a certain voltage the pairs generated by radiation in the depleted area will separate and drift in opposite direction towards the electrodes. The increment of the charge on the electrodes at the end of the movement is, as seen in the Chapter 2:

$$Q_a = q\left[U_w\left(\vec{r}_{p1}\right) - U_w\left(\vec{r}_{p0}\right)\right] \qquad (5.4)$$

where q is the magnitude of the moving charge, U_w is the weighting potential, $\vec{r}_{p1}$ is the final and $\vec{r}_{p0}$ the starting position. Figure 16 shows the weighting potential for a given strip of a detector with the same geometrical characteristics as that used in the measurements, calculated along the same strip axis and along the axis of the adjacent strip.

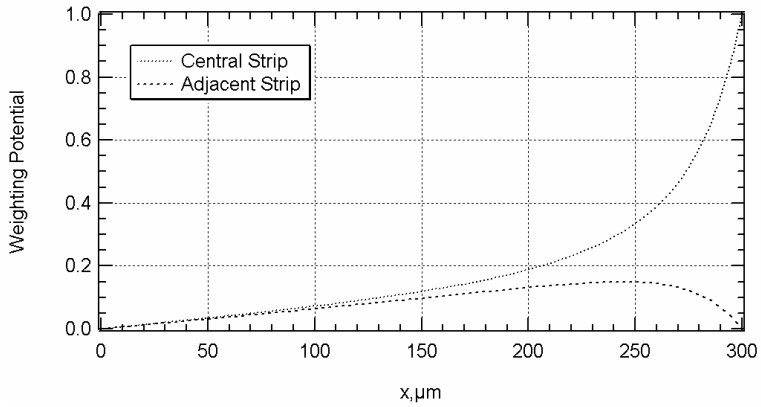

Figure 16 Values of the weighting potential relative to a strip of a microstrip detector with the same geometrical characteristics as the tested samples and calculated along the axis of the same strip and the axis of the adjacent one.

As can be seen from Figure 16, for each pair generated in the depleted region, for example along a strip axis, at the end of the collection process a charge equal to one hole is collected by the same strip and no net charge by the others.

It is worth stressing that in the non depleted region the voltage gradient is very low and hence there is essentially no carrier drift. Nevertheless the density of the free carriers in this volume and their long recombination time makes this volume behave like a conductor. So, for non depleted detectors, the calculation of the weighting potential has to be done only in the depleted area, considering as boundary the edge surface between the depleted and the non-depleted area (and not the back contact!!!). It follows that for a uniform ionising track along the direction orthogonal to one strip the charge collected by the same strip will grow linearly with the depleted depth and in proportion to the square root of the applied bias until the full depletion is reached. After this condition the charge collected remains constant with increasing voltage. At the same time the neighbouring strips do not collect any charge. This behaviour is well illustrated by the data in Figure 12 relative to IR illumination. For red illumination of the backside the data have a step-like behaviour with respect to bias voltage due to the fact that there is no collection of holes until the layer separating the depleted region and the volume where the holes are injected is small enough to let a portion of holes diffuse through it in a time shorter than the charge integration time.

For irradiated detectors things are more complicated. Already in the sample at the lowest dose, the bulk has experienced a type of conductivity inversion due to the

creation by high radiation, of levels in the forbidden gap that give, as seen in Chapter 3, a negative space charge in the depleted region. This is responsible for the junction type of contact at the microstrip backplane and explains why, even at low bias, charge is collected when the detector is illuminated with red light from the back. As observed in other experimental results, in irradiated detectors the electric field actually, seem to penetrate from both sides toward the centre leaving in the centre a region of low electric field, which can still be considered undepleted [13]. Nevertheless, in this case this undepleted area does not have a conductor-type of behaviour due to the short trapping time of the free carriers. Hence the weighting field is the same for full depleted and undepleted irradiated detector regions but the charge generated in the undepleted area will not be fully collected and will give a loss in the charge collection efficiency. Furthermore the charge generated in the depleted region might not be collected by the electrodes if its trapping time is less than the collection time, while the detrapping time is longer than the charge integration time and also if it ends in the undepleted region. This gives rise to the charge sharing mechanism appearing in the data from irradiated detectors.

The fact that the red curves show an initially similar behaviour is seen easily from the fact that the weighting potential at the backside is initially the same for the strip and the neighbouring. The additional fact that the IR does not show this behaviour is evidence that the detector starts to deplete from the two sides even though with a different penetration rate. In fact, for a smaller depletion at the strip side, the higher efficiency of signal induction relative to the backside reduces the charge induced at the adjacent strip and increases the charge at the (central) strip. The initial growth with bias of the induced charge on the neighbouring strip, for red and infrared laser, indicates that the depletion is increasingly moving towards the strip side. As the depletion extends over the region with higher induction efficiency[2] the charge induced on the neighbour decreases and that on the (central) strip increases rapidly, both in accordance with the weighting potential. The saturation occurring is the sign that:

[2] For microstrip detectors with the described geometry this region is around 50 μm from the strip side, as can be seen in Figure 16.

- Full depletion is achieved
- Most of the carriers travel through the bulk at their maximum velocity (*saturation velocity*), sweeping over the maximum distance before being trapped.

This saturation process does not seem to appear for holes injection (case A). This is due to the fact that even a minimal increase in the extinction length of the holes generated right at the backside can lead to a higher improvement of the charge induced on the central strip, given the ever increasing state of signal induction towards the strip side.

For the sample at the highest dose ($1*10^{15}$ cm^{-2} (24GeV) protons) it is difficult to see if the full depletion is reached at all. The signal from the red laser is not registered because at this dose the extinction length for holes is probably too small to allow them to reach a region where the weighting potential is sufficiently high with respect to the sensitivity of our system. The IR signal, by contrast, showing a linear increase over the whole range investigated does not give any easy indication of whether the full depletion is reached or not over the investigated bias range.

5.3.5 Other possible applications

The study of current pulses with this laser setup, which is generally referred to as transient charge technique (TCT) [14], can offer other valuables information on the internal electric field. The following chapter describes an extensive study with the TCT, presenting other highlights on the evolution of signal generation in irradiated microstrip detectors.

5.4 References

[1] Y. Tomita et al., Nucl. Instr. and Meth. A 270 (1988) 403

[2] S. Shaheen et al., Nucl. Instr. and Meth. A 352 (1995)

[3] J. Krizmanic et al., Nucl. Instr. and Meth. A 374 (1996) 315

[4] I. Abt et al., Nucl. Instr. and Meth. A 423 (1999) 303

[5] W.C. Dash and R. Newman, Phys. Rev. vol. 99, n. 4 (1955), p 1151

[6] Terahertz Technology Inc., 169 Clear road Oriskany NY 13424, U.S.A.

[7] R. Hofmann et al. Nucl. Instr. and Meth. in Phys. Res. 225 (1984) 601

[8] National Aperture, Inc. 16 Northwestern Drive, Salem, NH 03079-4810, U.S.A.

[9] National Instruments Corporation, 11500 N Mopac Expwy Austin, TX 78759-3504 U.S.A.

[10] For example see: http://www.labview.com/

[11] Atlas SCT/Detector FDR/99-2

[12] E. Hect and Zajac, Optics (6^{th} Ed.), Addison Wesley Publ. Co. (1980), Reading, Massachussetts U.S.A.

[13] V. Eremin et al., Nucl. Instr. and Meth. A 476 (2002) 556

[14] V. Eremin et al. Nucl. Instr. and Meth. A 377 (1996), 265

6 TCh/CT Measurements with Microstrip Detectors

The transient current /charge technique with the nanosecond infrared and red laser pulses for pair generation in the detector bulk was used to investigate the charge collection properties in non irradiated and irradiated silicon micro strip detectors developed for the ATLAS experiment at CERN. These techniques together with the full depletion studies, allow investigation of surface effects, timing, cluster size, and electric field degradation in the silicon bulk due to irradiation. Many of these studies will be presented in this chapter, together with their discussion.

6.1 Measurement Strategy

As we have seen in the previous chapter the TCh/CT setup is a valuable instrument to investigate the silicon detectors. Furthermore, the fine spatial resolution and a micrometric displacement system are fundamental to inspect segmented devices. In this way operating the two different lasers directed towards the top and the bottom of the device can be gained a good insight on the peculiarities of the electric field and the properties of the charge collection at different points of the sample. In Figure 1 is presented a simplified schematic of these operations that will be called in the future *X scan*.

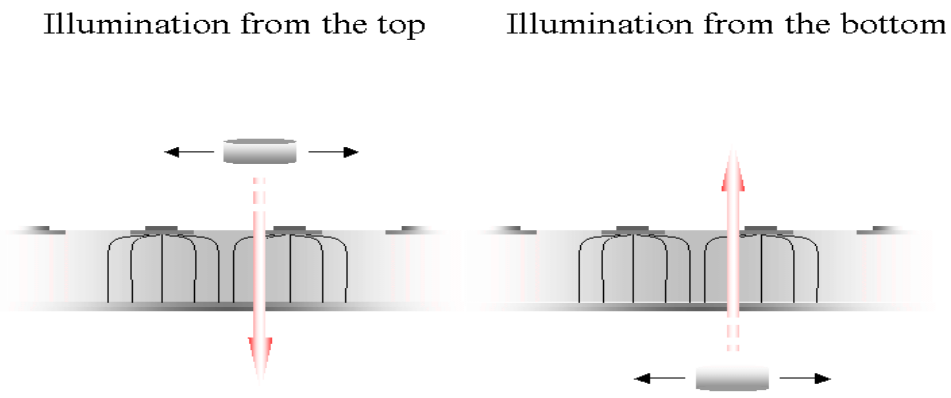

Figure 1 Schematic of the X-scan: the focused laser beam points toward the strip surface (right) or the back surface (left) moving with a step of few microns along the direction orthogonal to the strips as indicated in the figure, over a region of few strip pitches. The charge collected at each step for each strip laying in the investigated region gives the strip charge collection profile

In the following paragraphs will be presented first the measurements of the charge collection and then the analyses of the current pulses for each laser, operating as indicated in Figure 1. After the presentation of these measurements the results will be discussed.

6.2 Experimental Data

One parameter that is fundamental for the interpretation of the TChT/TCT data is the full depletion voltage. As described before, the samples under investigation, having been irradiated to different doses, show different values of the full depletion voltage. These values were extracted from the dependence of the collected charge Q_{coll} vs. bias, comparing the measurements with the IR and red laser generating carriers close to or on the readout strip axis as shown in the previous chapter. The values are summarised in Figure 2.

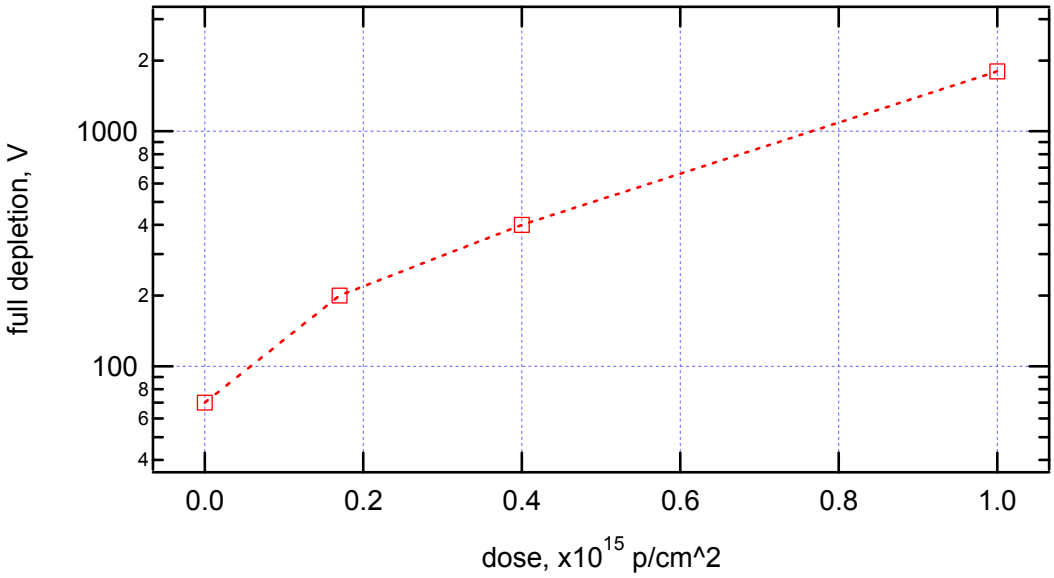

Figure 2 Full depletion voltages (V_{fd}) at different fluences. The V_{fd} at the highest dose was not measured but is an extrapolation from measurements in the range 0 to 1 kV. The justification of the extrapolation can be found in the text.

The full charge collection in the non-irradiated sample happens at 70 V. The full depletion bias is shown to increase with the absorbed dose. At the maximum dose the full depletion is certainly higher than the maximum bias that could be applied in our setup. Nevertheless within this bias range the charge collection increases linearly as seen in the previous chapter. This trend has been seen to be characteristic until the half of the full depletion voltage is reached. In this sense, for the experimental point at the maximum dose the indicated full depletion bias is only indicative of the minimum of its real value.

6.2.1 *Charge Collection for non irradiated detectors*

The cross strip scans measured with the red laser are shown in Figure 3, Figure 4 and Figure 5. For both scans measured with the laser on the strip side (p^+-side) and back side (n^+-sides) respectively the collected charge *(Q_{coll})* correlates well with the topology of the strips and the pitch of 80 µm is easily distinguished.

For the n^+-side, in the mid-gap between the strips, a charge sharing of 50% is observed. Due to the roughness of the unpolished silicon surface underneath the back contact the light is partially scattered away from the laser beam direction, which is orthogonal to the surface. This is evidenced by the non-uniformity of charge collection for each strip and is stronger for lower bias where the diffusion of the generated charge clouds plays a stronger role. At lower bias a wider profile of the charge collection is observed due to diffusion, however the 50% charge sharing is still at the mid gap point.

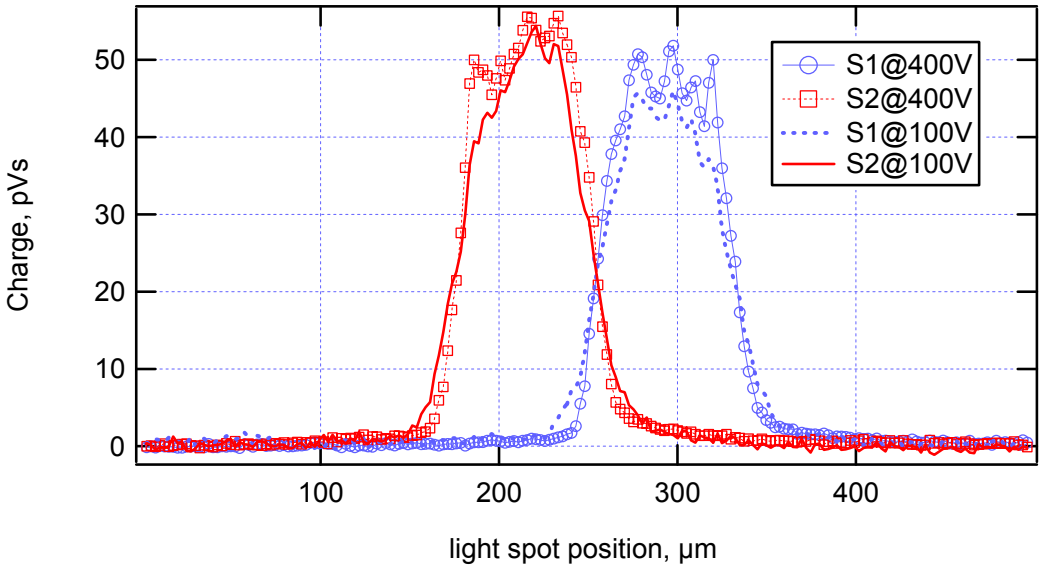

Figure 3 Cross-strip scan measured on the n^+-side with the red laser. The signals are the charge collected at the two adjacent strips (respectively S1 and S2) for the bias of 100V and 400V.

The signal distribution with the laser on the p^+-side (Figure 4 and Figure 5) shows different features from the n^+-side. First of all, the plot of Q_{coll} for the p^+-side scan contains low signal regions due to the opacity of the 18 µm wide Al metallisation. Nevertheless, although the charge collection correlates well with the topology of the strips and the pitch of 80 µm is easily measured between the opacity

zones for two adjacent strips, the charge shows the striking feature of a negative signal region. This negative signal is read out for each strip when carriers are injected beyond their closest interstrip midgap.

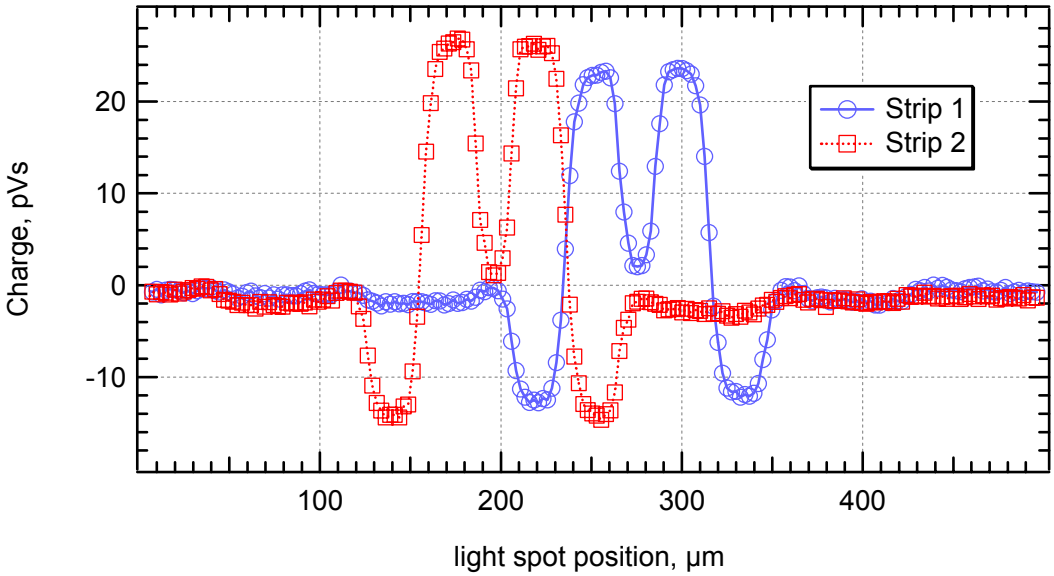

Figure 4 Cross-strip scan measured on the p^+-side with the red laser for a bias of 200V

As can be seen from Figure 5, the value of negative signal is more than 50% of the positive one and is not affected much by the applied bias. It is interesting to note that a very small negative charge, is also collected beyond the adjacent strip.

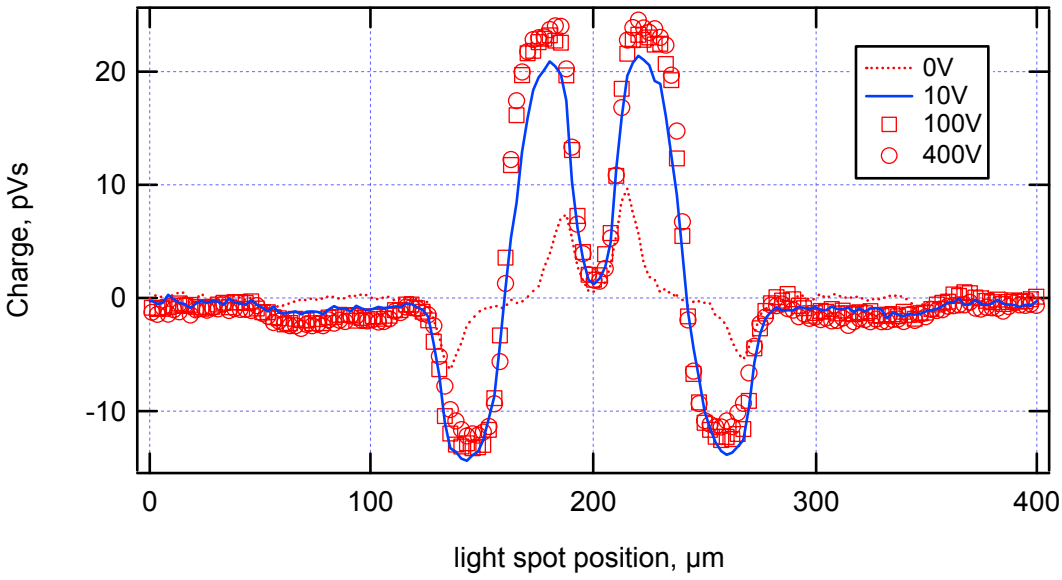

Figure 5 Cross-strip scan measured on the p^+-side with the red laser for different bias voltages.

At 0 V the collected charge is due the built in electric field at the p^+n junction and 10 V is enough to collect all the charge generated with the red laser.

The signal distribution measured with the infrared laser (Figure 6 and Figure 7) correlates well with the one observed with the red laser. The scan of the n^+-side shows a slightly irregular profile due to the roughness of the surface, as explained before; nevertheless the strip pitch is well resolved.

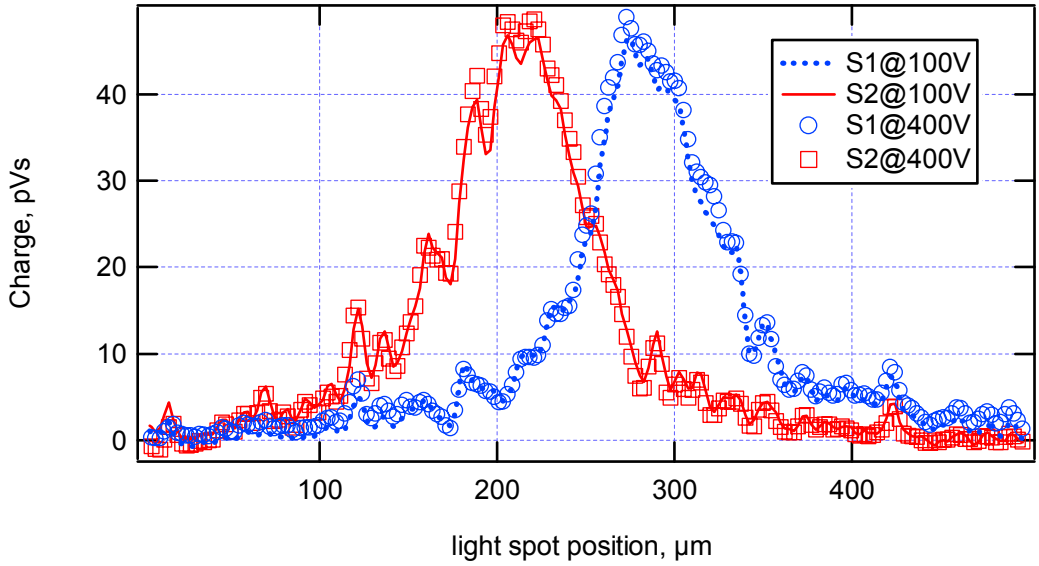

Figure 6 Cross-strip scan measured on the n^+-side with infrared laser. The signals are the charge collected at the two adjacent strips (respectively S1 and S2) for the bias of 100V and 400V

Apart from the low signal region due to the Aluminium strips, the scan of the p^+-side between the Al strips does not show any peculiarities compared with the n^+-side, both corresponding to a uniform pair generation through the whole bulk.

With respect to the case of the red light scan, the signal of inverted polarity is only observed for a much smaller bias than that required for the full depletion. Considering that in this case the depletion is achieved only within the superficial layers of the silicon microstrip and that the penetration depth of the red laser is only a few microns in silicon, this effect of inverted polarity charge is clearly related to the peculiarities of the segmented surface of the detector. A deeper investigation of this phenomenon, together with an attempt to explain it, will be given later in this chapter.

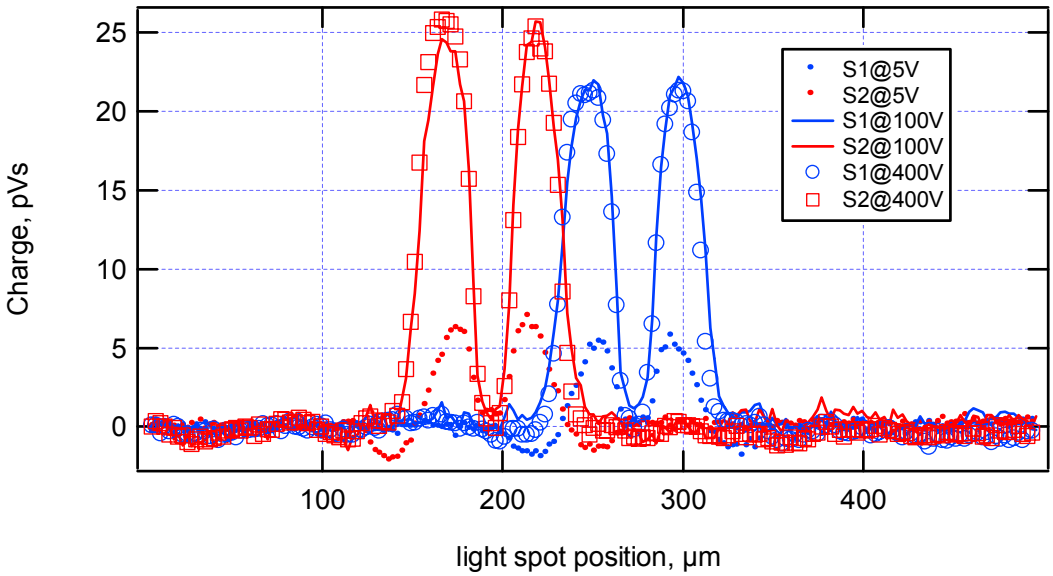

Figure 7 Cross-strip scan measured with infrared laser on the p-side for different bias voltages: 5 V, 100V and 400V respectively. At 5 V an inverted polarity charge is collected when illuminating the midgap region.

6.2.2 Charge Collection for irradiated detectors

As seen in previous chapters, the changes in the material due to heavy irradiation strongly influence the electrical properties of the silicon detectors. These are responsible for dramatic changes in the charge collection.

For the sample irradiated to a dose of $1.7*10^{14}$ $_{24GeV}$ pcm^{-2} the full depletion voltage is 200V. At this dose the inversion of the type of conductivity has already appeared and this is confirmed by the red scan of the n^+-side. In fact in this case, also for a lower bias than the depletion voltage, a portion of the charge generated at the backside is collected at the electrodes and a wide strip profile is measured. For higher voltages, the charge profile becomes steeper and the charge collection increases. These measurements are shown in the Figure 8.

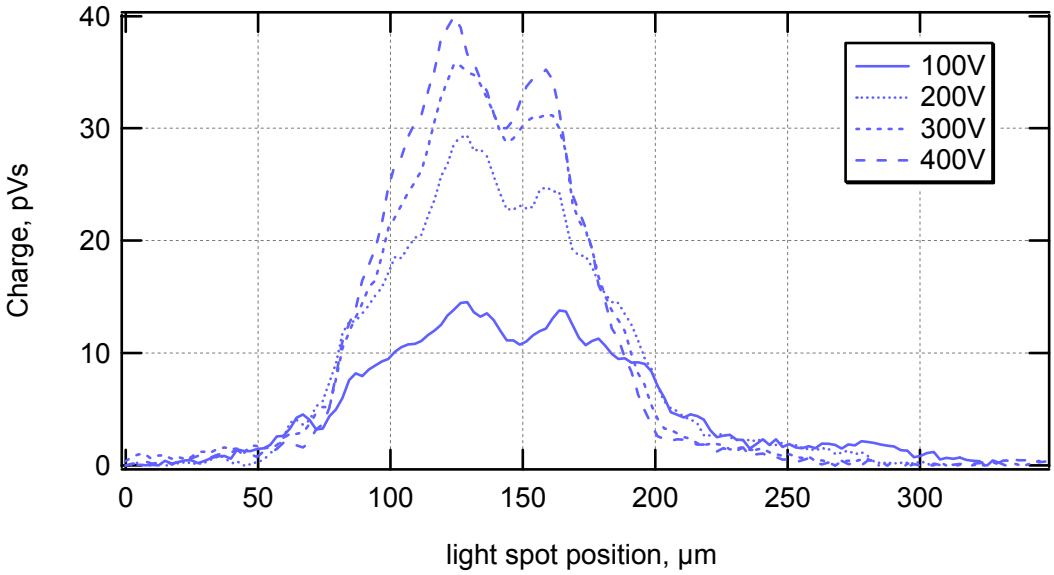

*Figure 8 Red scan of back side for the 1.7*10^{14}$_{24GeV}$pcm^{-2} sample at different bias voltages. Charge readout by only one strip.*

Although the bulk inversion has already appeared at this dose and the detector should start to deplete from the backside, for a lower bias than the full depletion voltage the electric field present at the strip contact enables same charge collection, although small. Nevertheless the electric field seems to be present only in the region closest to the strips. To collect the charge from the whole inter-strip gap the full depletion condition has to be satisfied. This can be seen in detail in Figure 9.

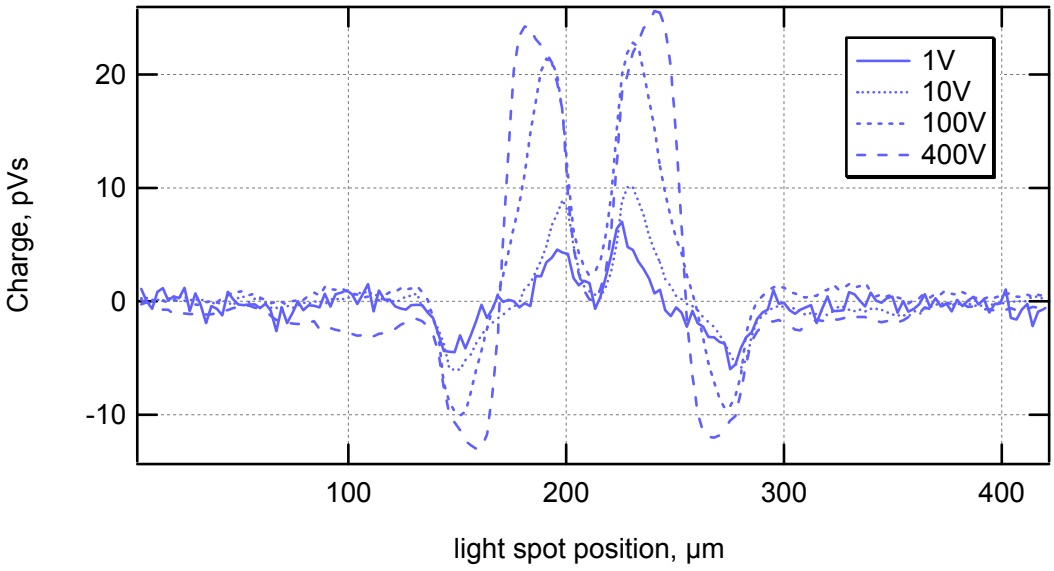

*Figure 9 Red scan of front side for the 1.7*10^{14}$_{24GeV}$pcm^{-2} sample at different bias voltages. Charge readout by only one strip.*

As can be seen from Figure 9, the inverted polarity charge feature is preserved after irradiation and at this dose it presents very similar features to the one shown before irradiation.

A better insight into the charge collection after a uniform generation of carriers through the bulk can be gained with the IR laser scan, as was seen in the case of the un-irradiated detector. After a dose of $1.7*10^{14}$ $_{24GeV}$ pcm^{-2}, a signal is also registered when illuminating regions a few strips away from the one being read out. This causes a loss of resolution, which plays a dramatic role in silicon detectors used for tracking in high luminosity experiments. As noted in the previous chapter, it is worth remembering that, in heavily irradiated silicon detectors, under depletion and trapping both play a role in the charge sharing mechanism. This is strongly evident from Figure 10 which shows IR laser scans, performed over an area of several strips, for different voltages. For a lower bias than the full depletion voltage, which is 200 V for this dose, the amplitude of the charge collected in points up to a few strips away from the one being read out is comparable with the signal collected at the read out strip and only after full depletion these signal are well distinguished. Nevertheless the charge sharing mechanism is also present at higher bias, due to trapping, and a residual charge is still collected away from the readout strip.

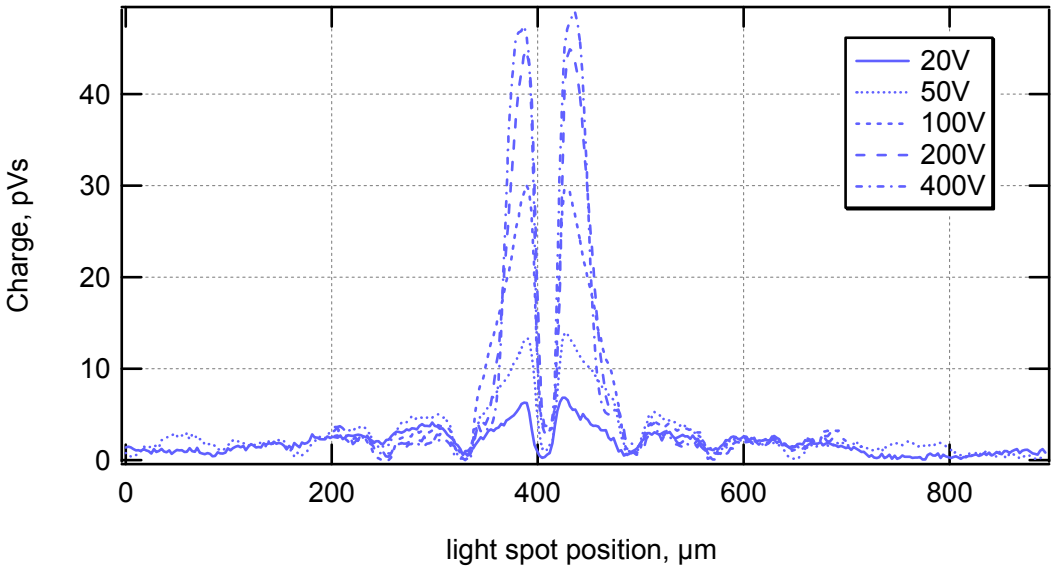

Figure 10 IR scan of the front side for the $1.7*10^{14}$ $_{24GeV}$ pcm^{-2} sample at different bias voltages.

The detector degradation increases for a dose of $4*10^{14}_{24GeV}pcm^{-2}$. With a full depletion voltage of around 400V, the measurements performed at this dose seem to reproduce the results obtained at half of the bias with the $1.7*10^{14}_{24GeV}pcm^{-2}$ sample. In particular, Figure 11 shows the charge measured on one strip for a red laser scan on the back side at different voltages. As can be seen, at 200 V the charge profile is still very wide. Only when the full depletion voltage is achieved a substantial difference in the charge collection appears between the readout strip region and the adjacent ones.

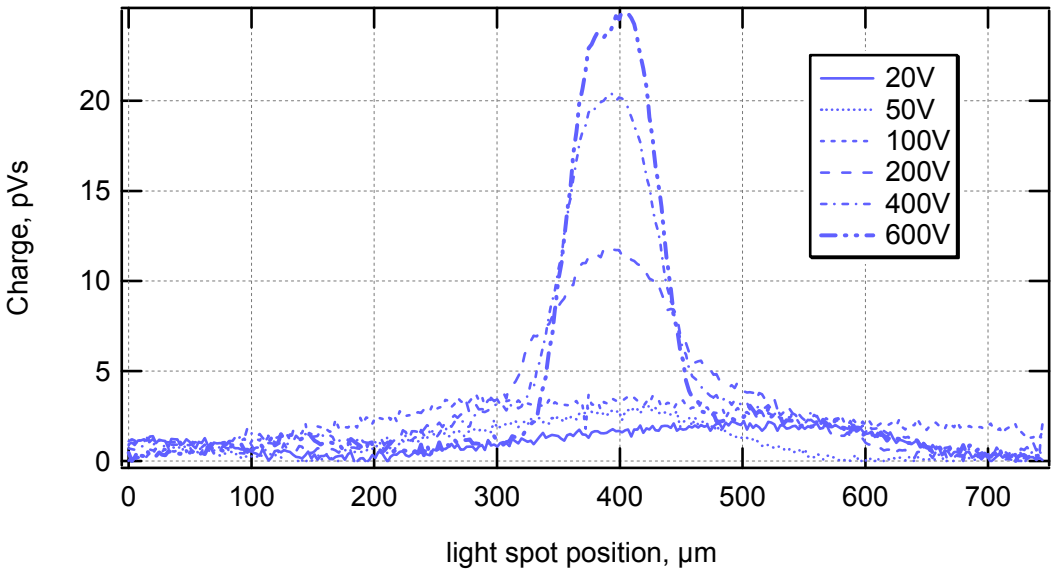

Figure 11 Red scan of the backside for the $4*10^{14}_{24GeV}pcm^{-2}$ sample at different bias voltages.

Concerning the red laser scan of the strip side, there is still some charge collection in narrow regions close to the strips. These regions become wider with increasing voltage. This width starts to stabilise only at the full depletion. Furthermore the trend observed previously of a negative signal when the charge is generated at the neighbouring strip, is still preserved.

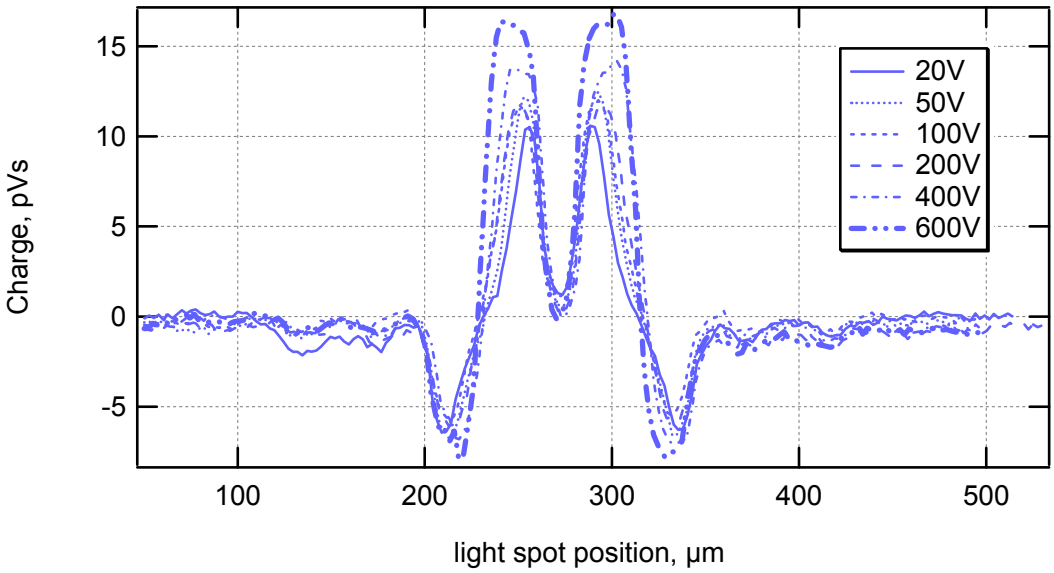

Figure 12 Red scan of the front side for the $4*10^{14}_{24GeV}$ pcm^{-2} sample at different bias voltages.

Also the IR laser measurements reproduce well the results seen with the $1.7*10^{14}$ $_{24GeV}$ pcm^{-2} sample with double the bias. It is worth noting that the charge collection increases almost linearly in going from the adjacent strip to the read out strip for all biases lower than the full depletion voltage. For values higher than the full depletion voltage, a rise steeper than the linear growth is observed.

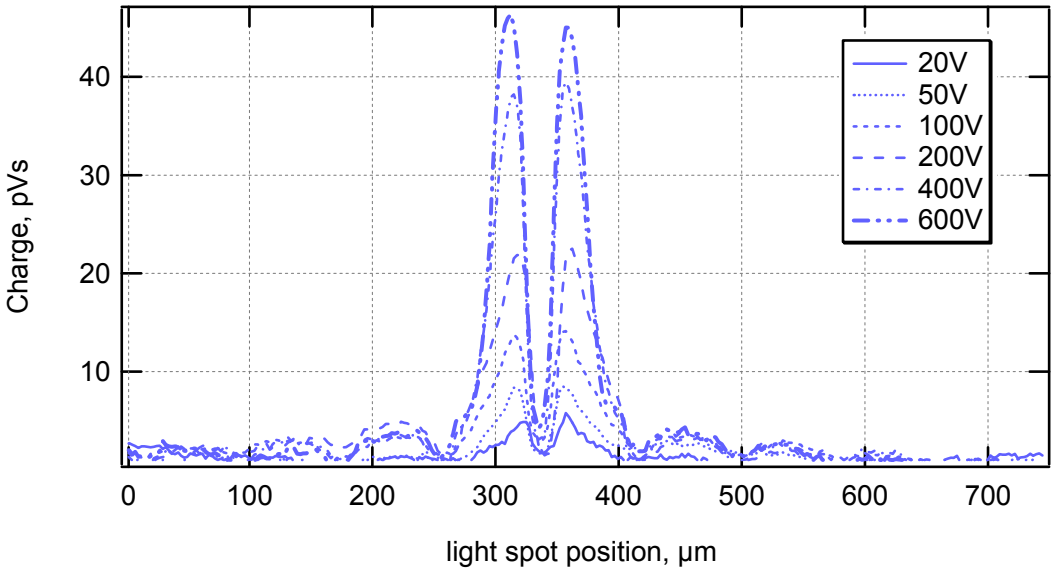

Figure 13 IR scan of the front side for the $4*10^{14}_{24GeV}$ pcm^{-2} sample at different bias voltages.

For the sample irradiated at $1*10^{15}{}_{24GeV}$ pcm^{-2} the degradation is such that the maximum bias that can be applied is not enough to deplete the detector fully. Moreover, in the available bias range (0V to 900V) the red light incident on the back plane generates a very low signal that cannot be detected with the available readout on the microstrips. The reason for such a limitation has to be found in the short extinction length of the generated carriers together with the low weighting potential at the back contact. The red laser scan of the strip surface (see Figure 14), on the other hand , still shows some charge collection. Nevertheless this is unchanged in the range from 50 V to 900 V and similar to the charge collected with the red laser illumination at lower doses for a very low bias. A particular effect which was not observed for lower doses, is the positive charge collected in regions beyond the adjacent strips.

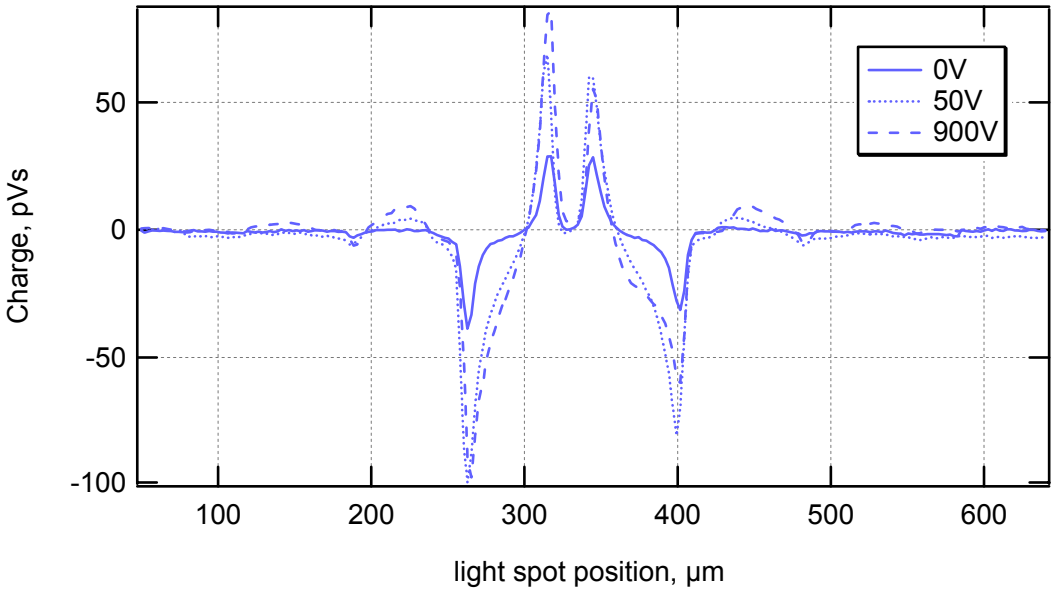

Figure 14 Red scan of the front side for the $1*10^{15}{}_{24GeV}$ pcm^{-2} sample at different bias voltages.

For uniform carrier generation in the bulk with the IR laser, the detector pitch is very poorly defined. It can be seen from Figure 15 that the charge collected at one strip decreases smoothly as the laser moves towards the neighbouring ones. Moreover there is no discontinuity between the read out strip and its neighbour over the whole bias range and the strips are localised only thanks to the opacity of their metallisation.

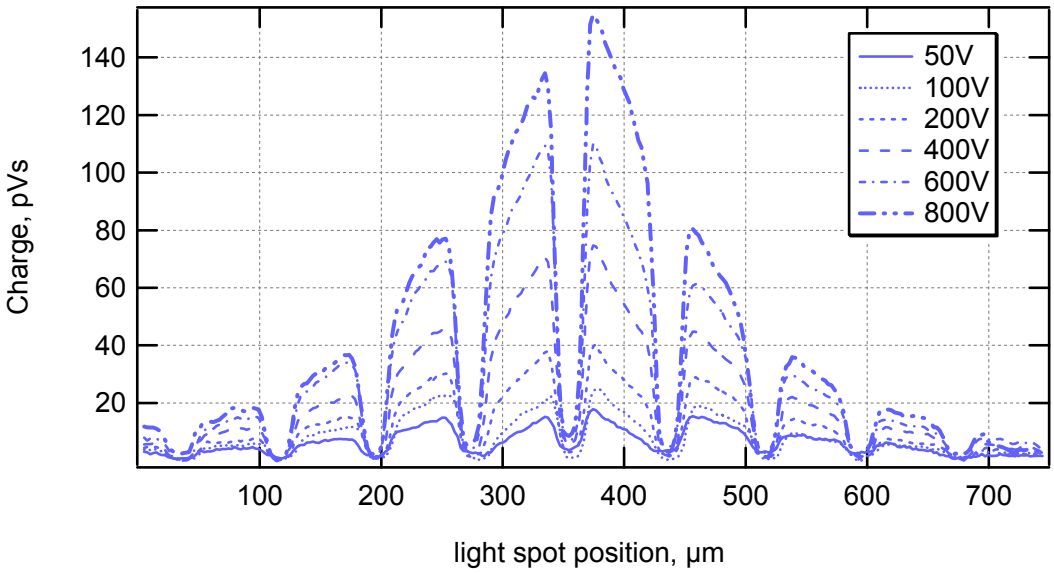

Figure 15 IR scan of the front side for the $1*10^{15}_{24GeV}$ pcm^{-2} sample at different bias voltages.

When microstrip detectors reach this state of degradation, the initial fine spatial resolution is lost and the tracking of ionising particles is seriously compromised. A more detailed analysis of the loss of resolution with fluence is described in the next paragraphs. The consequence of this loss on particle tracking will be described later on also in terms of limits on high energy physics studies.

Summarizing, measurements using the transient charge technique for microstrip detectors have revealed two main peculiarities, which deserve a deeper treatment. The first is the reverse polarity of the charge collected after a shallow generation of pairs at the strip surface. This feature has appeared without radical changes for every irradiation dose and its understanding is critical for a complete understanding of the device physics of microstrip detectors. The second point of discussion is the loss of resolution in irradiated strip detectors. This can become a serious limit on the use of segmented detectors in silicon and is a point of concern for most of the modern high energy physics experiments that need to run at high luminosity accellerators.

6.2.3 The reverse polarity of collected charge.

The reverse polarity of the collected charge will be discussed in the case of the non-irradiated detectors. Nevertheless, since there is no relevant change in this effect

before and after irradiation, the analysis that will follow can be applied also to the results from the irradiated detectors.

The charge collected in semiconductor detectors is the charge on the readout electrode at the end of the induction processes that appear while electrons and holes generated by the radiation and separated by the electric field drift towards the electrodes. In the case of the signal read out from the p^+-contact, which collects holes, the collected charge signal is positive. This regularity is confirmed for the red laser illumination of the n^+-contact. In this case the holes are collected by p^+-strips and induce a positive signal that falls to zero when the carrier injection point moves towards neighbouring strips, as shown in Figure 3.

Nevertheless, pairs generated on the strip side give a result different to the expected one, as shown in Figure 4 and in Figure 5. The charge collected at the p^+-contact is positive when the charges are generated in the area near the read out strip but, as the injection point approaches the adjacent strips, the charge signal, instead of falling to zero, turns to a negative polarity. Moreover, this effect appears only if the electron-hole pairs are generated in a shallow volume under the strip surface. In the case of the infrared laser scan, where pairs are generated almost uniformly along the laser track through the detector thickness, the charge collected does not show a polarity-inverted signal unless the detector is depleted only in a small region close to the strips (see Figure 7).

This phenomenon does not seem to depend on the applied voltage. One possible explanation could be found in the peculiarities of the electric field in the interstrip gap, where the presence of an undepleted area located in the midgap just underneath the SiO_2 layer can influence the charge collection. This layer can act as a sink for electrons generated near the surface causing the observed in-complete charge collection. This assumption is consistent with the predictions from Ramo's theorem, according to which a charge q moving over a distance dx will induce on each electrode j a charge Q_j that is:

$$Q_j(dx) = qdV_{wj} \qquad (1)$$

where dV_{wj} is the increment of the weighting potential relative to the electrode j over dx.

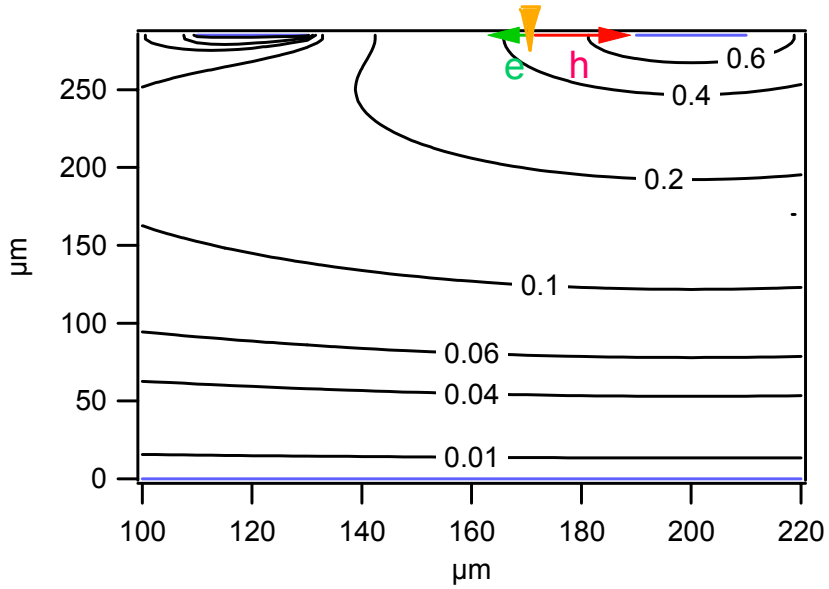

Figure 16 Weighting potential in microstrip detectors. For a short-range pair generation on the detector surface (orange arrow) the electron will move toward the mid-gap (green arrow) and the holes toward the strip. At the end of their motion the charge induced on the strip closest to the injection point is 60% of all the generated holes, as can be seen from the iso-potential lines.

For the assumption given before, all the pairs generated underneath the oxide will separate. While the holes are collected at the strip the electrons will drift toward the middle of the interstrip gap. Given the weighting potential for the investigated geometry (see Figure 16), the charge induced on the strip where the holes are collected is positive and only about 60% of the full-generated charge. At the adjacent strip the charge collected will be negative and about 40% of the full generated charge. This is exactly what is observed in the measurements as shown in Figure 17, which compares the measured charge X scan at the same strip respectively on the back side and on the front side, both resulting from red laser pulses of very similar amplitude and width.

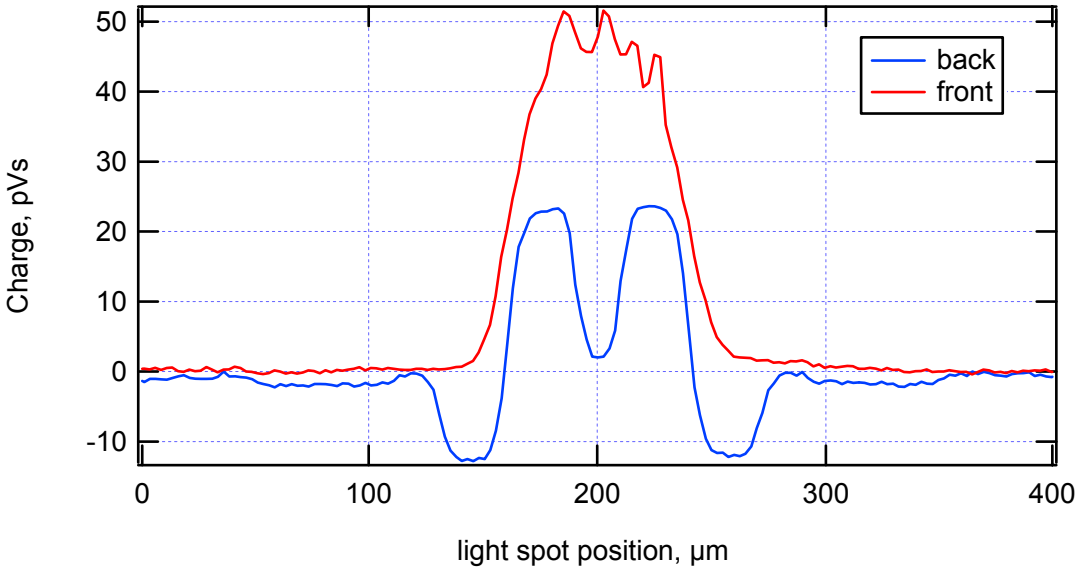

Figure 17 Comparison between the charge X scan at the same strip respectively on the back side and on the front side, both resulting from red laser pulses of very similar amplitude and width.

The presence of the undepleted layer influences also other features of the charge collection that will be described later.

6.2.4 Degradation of resolution in the irradiated samples

As a dramatic consequence of the irradiation of silicon detectors, the spatial resolution is seen to degrade. Under depletion of the detector and charge carrier trapping in the bulk have been proved to be the causes of this degradation. In fact these two phenomena, responsible for the incomplete charge collection at the detector electrodes of carriers generated by ionizing radiation, can cause if the radiation dose is too high, a loss of the information of the pitch of the strips. In the Figure 18 a striking comparison of the charge collection for a single strip between non-irradiated and irradiated ($1*10^{15}{}_{24GeV}$ pcm^{-2}) detector, based on IR laser X-scans, clearly shows the deterioration of the spatial resolution in the latter.

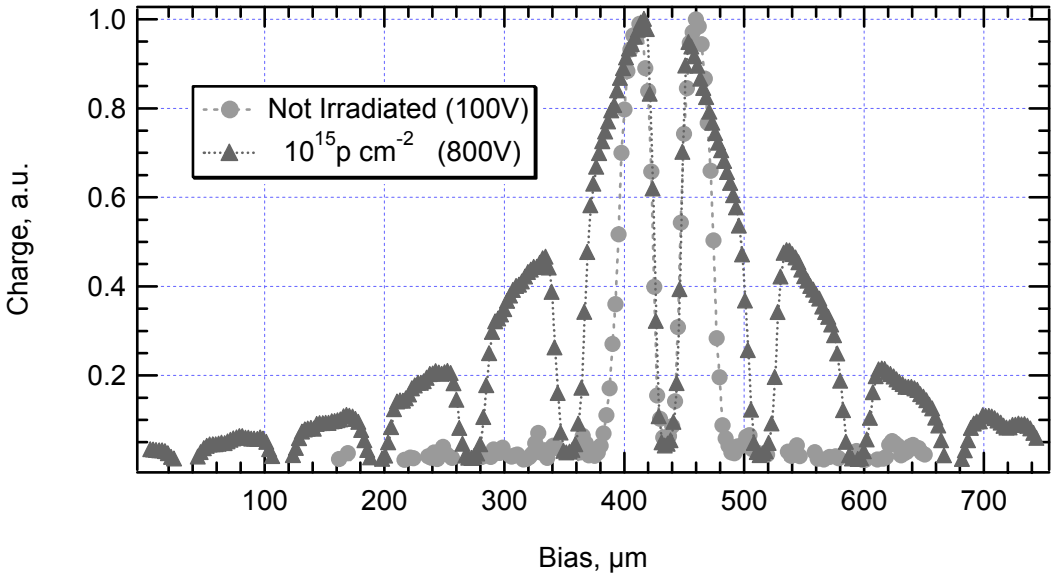

Figure 18 Comparison between the charge X-scan for a non irradiated and a very highly irradiated ($1*10^{15}{}_{24GeV}$ pcm^{-2}) detector. The two charge profiles are normalised to their maximum value.

This extreme case, well beyond the expected 10 year radiation dose in the inner region of the ATLAS strip detectors, is nevertheless useful to explore the radiation limits of these devices. Moreover it is very important to understand how the resolution varies for lower doses and if it can be improved by applying a higher bias. A qualitative criterion to evaluate the space resolution of the microstrip detectors is to see how much charge a strip reads when an ionizing track crosses the detector on the adjacent strip and compare it to the charge collected when the ionizing track is on the strip itself. The ratio of these two quantities, which for a non-irradiated detector is compatible with zero, is shown in Figure 19 for the available doses. This plot summarises the results already shown in the previous section. Here S_2 is the charge collected for an ionizing track at the adjacent strip and S_1 is that collected when the ionizing track is on the readout strip.

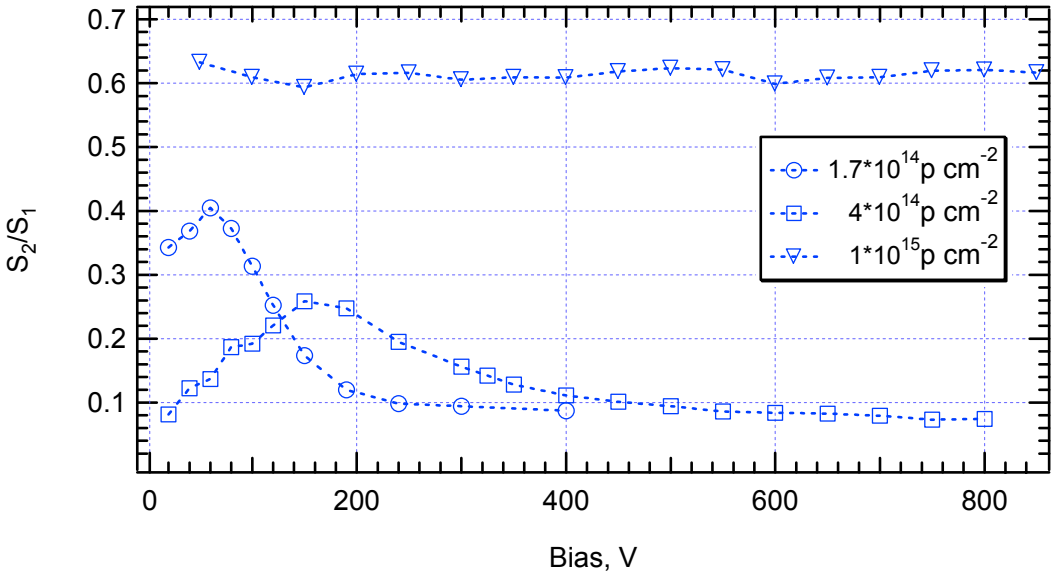

Figure 19 S_2/S_1 at different doses.

For the two doses lower than $4*10^{14}_{24GeV}$ pcm^{-2} S_2/S_1 is stably less than 0.1, once the full depletion is achieved. As the bias increases S_2/S_1 seems to ontinue to decrease but very gradually. For$1*10^{15}_{24GeV}$ pcm^{-2}, on the other hand, the ratio S_2/S_1 is stably high and seems to be independent of the bias. It is worth remembering that in the investigated bias range for this sample the full depletion voltage does not seem to be reached. The good result of high resolution for doses up to $4*10^{14}_{24GeV}$ pcm^{-2} testifies to the reliability of these tracking sensors even in the harsh radiation environment foreseen within ATLAS, in the region where this type of device will be placed.

6.3 Study of current pulses before and after high irradiation

The features of the collected charge distribution vs. laser beam spot position co-ordinate described above (from Figure 3 to Figure 7 before irradiation and from Figure 8 to Figure 15) are also seen in the current responses. Note here that the current response is:

$$i(t) = \frac{d}{dt} Q_{coll}(t) \tag{2}$$

Additional information on the electric field profile can be derived from the current pulses. In fact, as we have seen in the previous chapters, the current flowing through the electrodes when a charge q is moving in the detector bulk is given by:

$$i\left(x(t)\right) = -q * \vec{E}_w\left(\vec{x}(t)\right) * \mu\left(E\left(\vec{x}(t)\right)\right) * \vec{E}\left(\vec{x}(t)\right) \tag{3}$$

where $\vec{E}_w$ and $\vec{E}$ are respectively the weighting and the electric field, $\mu(E)$ is the mobility and $\vec{x}$ is the trajectory. In this case, given the short absorption length of the red laser, the current pulse due to hole clouds generated the back side[1] at each instant gives information on the electric field for a different point along the charge cloud trajectory which, apart from diffusion, runs along electric field lines. This information can be extracted more easily for straight-line trajectories, i.e. when the charge cloud is generated along the strip axis (for example, point A and D of Figure 20).

[1] As we have seen with the TChT measurements, for electron-hole pairs generated with the red laser on the strip side the electrons do not reach the backplane.

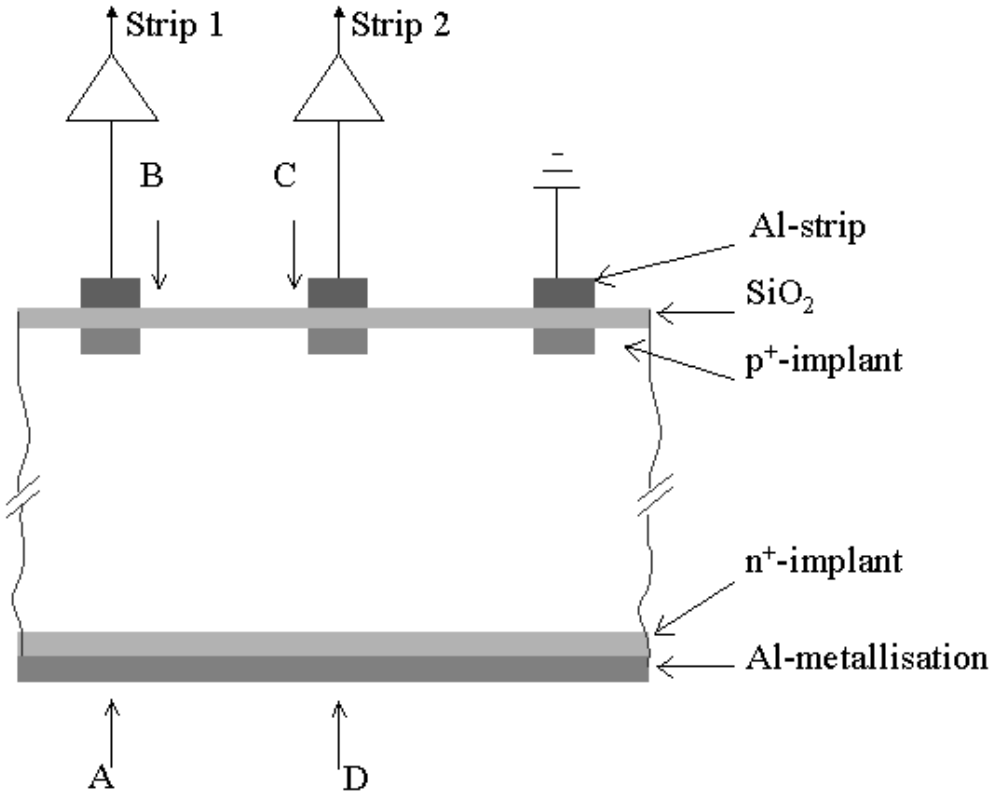

Figure 20 Schematics of the experiment. The points A, B, C, and D on the cross section of a portion of the microstrip detector indicate the laser pointing at different points of carrier injection with respect to the readout strip, the one linked to the amplifier, used in the experiment.

Given the almost uniform generation of charge density $\rho(\vec{x})$ in the detector bulk by the IR laser the current pulse readout will be:

$$i(x(t)) = -\int_{\gamma} \rho(\vec{x}) * \vec{E}_w(\vec{x}(t)) * \mu(E(\vec{x}(t))) * \vec{E}(\vec{x}(t)) d\vec{x} \qquad (4)$$

Hence information on the electric field is hard to extract. Nevertheless, measurements with the IR laser also play a key role in the TCT for microstrip detectors. In fact, due to the similarity with mips, the IR laser can give more reliable answers concerning to what is the timing in these devices.

In the following paragraphs these measurements will be described. For most of them the points in the Figure 20 will be used to describe the experiment.

6.3.1 Before Irradiation

For red laser injection on the p^+-side in the area close to the Al metallisation, the positive charge collected at the same strip (point B in Figure 20), corresponds to a positive polarity of current pulse with a gradual decay as illustrated in Figure 21. In the inter-strip gap (between points B and C) the current response decreases in amplitude and then inverts polarity at the mid-gap. From here on, the amplitude of the negative pulse increases, reaching a maximum at the border of the p^+-implant of the adjacent strip. This signal corresponds to the negative Q_{coll} in Figure 4 and Figure 5. The duration of the negative current response is close to the width of the positive current response.

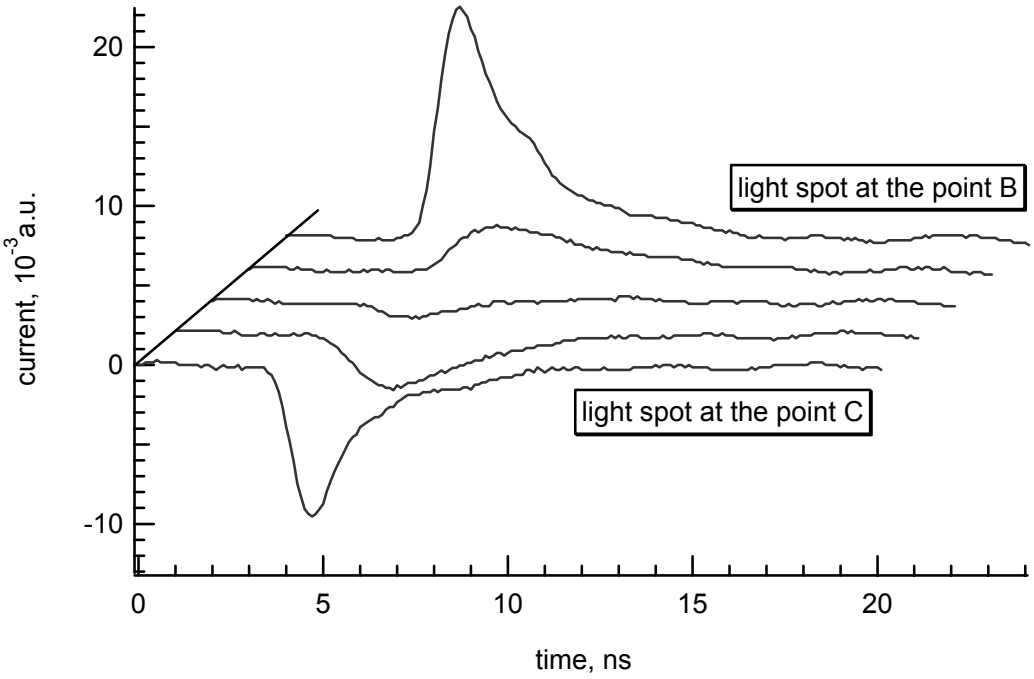

Figure 21 Current pulses measured for red laser illumination of the p^+-side of the detector at 200 V bias. The pulses are read out from the strip1 with the light spot at different points between two neighbouring strips.

Concerning carrier injection from the back side, where the electric field is lower, special attention has been paid to minimize or eliminate any experimental factor leading to a delay in the charge collection of the detector. The most important of these is the plasma effect arising when dense electron–hole plasma is generated in the detector space charge region. This effect, widely investigated for α-particle detection [5], can increase the duration of the charge collection by up to an additional

10 ns. A laser pulse focused within an area of 10 μm diameter, generating the same number of electron-hole pairs as the number generated by α-particles, gives a plasma effect which is even stronger, due to the shorter absorption length of the light (~5 μm at a wavelength of 660 nm). The limitations related to the plasma effect can be easily estimated in a one-dimensional model. In the approximation of pairs uniformly generated by the light in a thin layer, the electric field screened by the plasma is:

$$E = \frac{e\ N}{2\,\varepsilon\,\varepsilon_0 A} \qquad (1)$$

where the product $\varepsilon\varepsilon_0$ is the permittivity of silicon, N is the number of the light generated pairs, e is the elementary charge and A is the area of the light spot.

To eliminate the plasma effect the light intensity was adjusted to generate about 25000 pairs (equivalent to one minimum ionizing particle), that is about 50 times less compared to 5 MeV α-particles, giving rise to an electric field of $6*10^2$ V/cm at the back side. With this condition a bias of 2 V more than the full depletion voltage is enough to overcome screening due to the plasma effect.

The cross strip scan of the n^+-side towards the adjacent strip, as illustrated in Figure 22, does not show the negative current pulse and correlates well with Figure 3. However, pair generation at a point located on the other side of the interstrip gap leads to a bipolar current pulse.

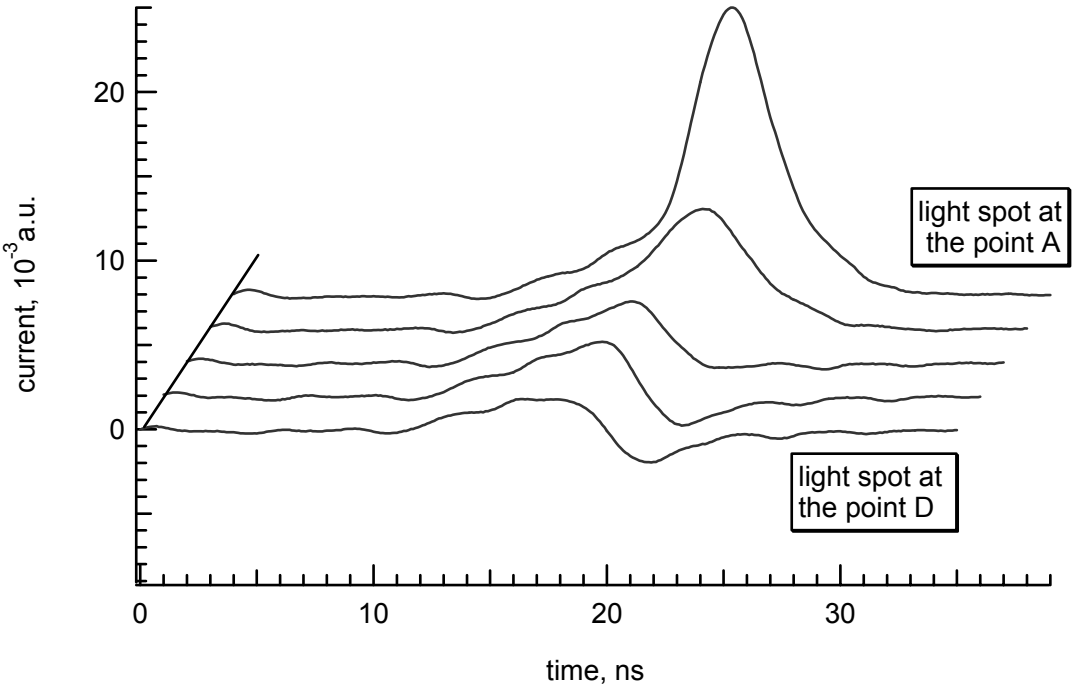

Figure 22 Current pulses measured for red laser illumination of the n^+-side of the detector biased with 200V. The pulses are read out from the strip1 with the light spot at different points between A and D.

The current responses measured at the n^+-side on the strip axes at point A (see Figure 20), show a slow rising component and a subsequent fast component. The duration of the slow component decreases with increasing bias (Figure 23), however even at the highest bias of 400 V the effect still exists.

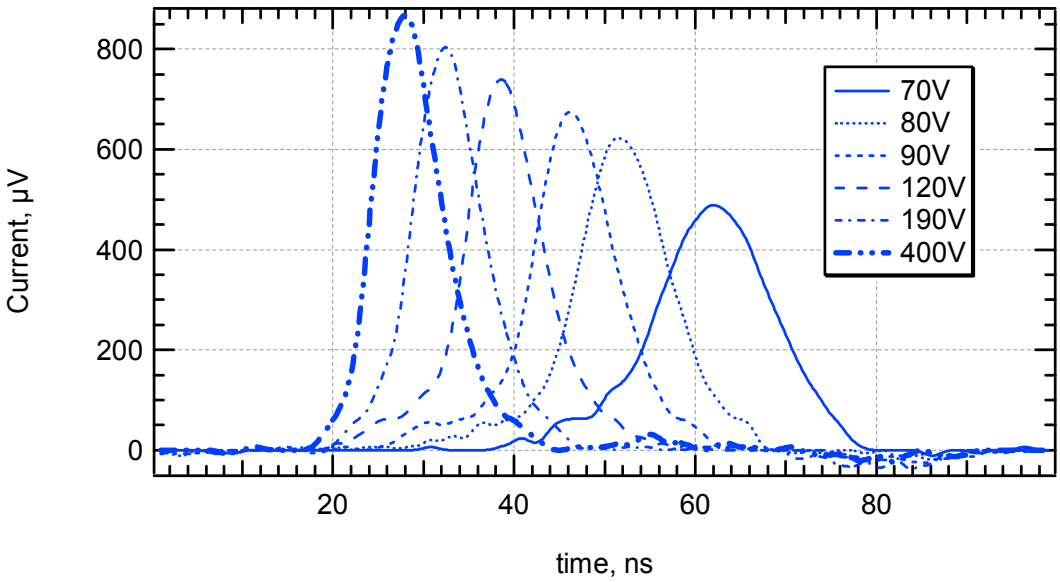

Figure 23 Current responses for pair injection by the red laser at the n^+-side of the detector on the axis of the read out strip.

The current pulse for the infrared laser illumination does not contain any peculiarities (Figure 24) and the amplitude of the current response is sharply reduced in the middle of inter strip gap, down to 0 when the light spot is positioned on the other half of the midgap.

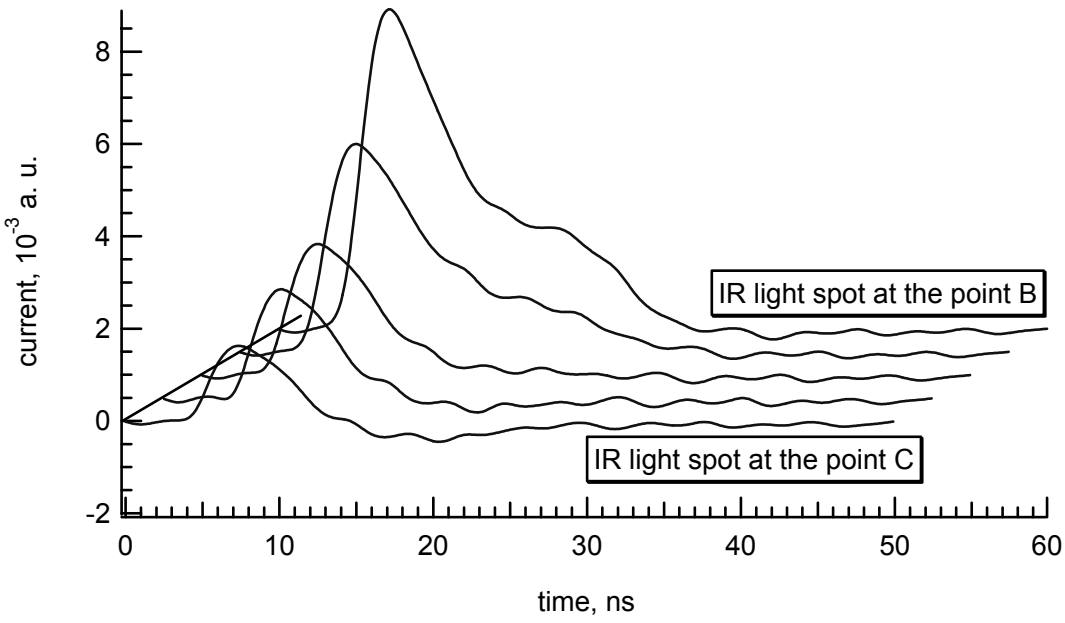

Figure 24 Current pulses measured with infrared laser illumination of the p^+-side of the detector at 200 V bias. The pulses are read out from the strip1 with the light spot at different points between two neighbouring strips.

For the signals with the IR laser pointing at A (see Figure 20) the initial steep rise is followed by an amplitude decrease whose duration decreases with increasing bias. The end of this decrease is characterised by a slow decrease that lasts around 10 ns and seems not to depend much on the bias. These pulses are shown in Figure 25.

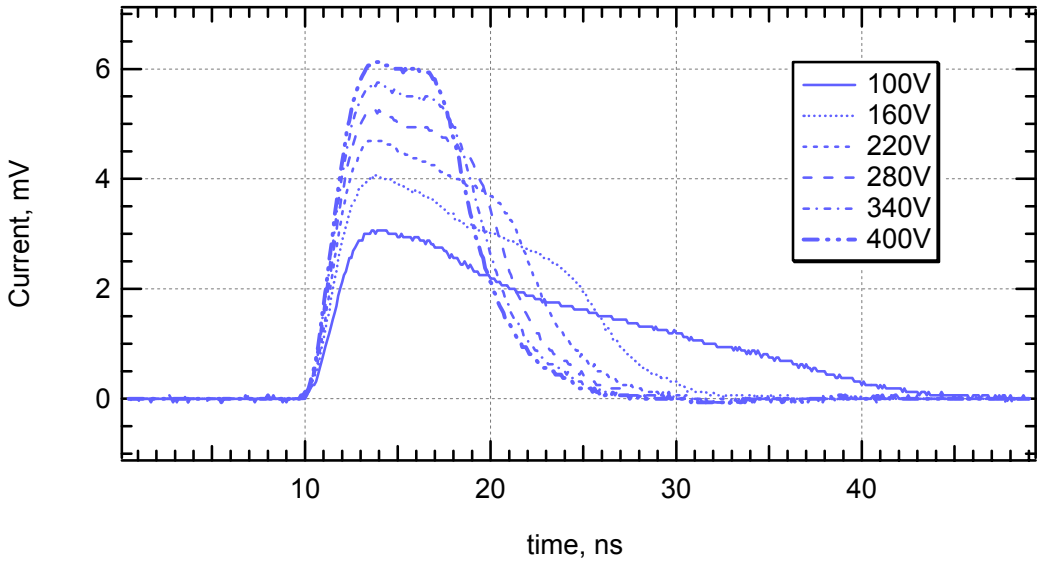

Figure 25 Current pulses measured for infrared laser illumination of the n^+-side of the detector at different bias voltages. The pulses are read out from the strip1 with the light spot on the same strip axis.

6.3.2 The charge collection time

The charge collection time in silicon detectors, i.e. the time the charge generated by ionizing radiation takes to reach the electrodes, is a fundamental characteristic of detectors used in high luminosity experiments. For pad detectors the charge collection time is coincident with the pulse length of the TCT IR signal as well as the TCT signal due to hole injection. These two types of signals are characterized by a rapid current reduction at the end of the collection process. Two main differences appear for the investigated microstrip detector: first, the hole injection signal is wider than the IR signal (see Figure 23 and Figure 25) and second, there is no rapid current reduction at the end of the signal. In particular, the pulses resulting from hole injection (Figure 23) show a first stage where the induction is low, lasting a time t_{id}, and then a peak characterized by a peak time t_{max} and full pulse width t_{pulse}. To help

visualisation of these timiming quantities, Figure 26 shows a representation of the hole injection pulse.

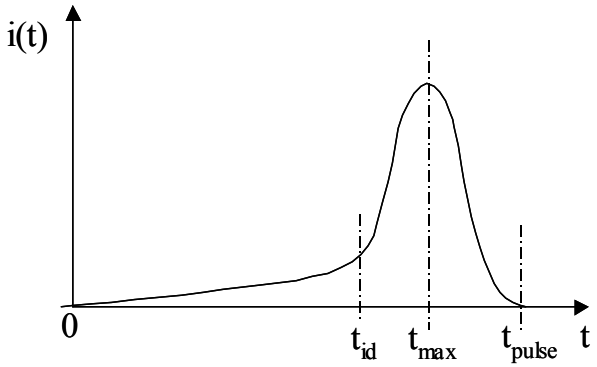

Figure 26 Schematic of a current pulse due to hole injection on the strip axis.

The returned charge

To understand the charge collection a numerical simulation of the process has been done. In particular the current pulses due to hole injection have been carefully examined. These current pulses, presented in Figure 23, were measured at the strip axis in order to simplify significantly the drift time estimation and the calculation of the detector response. In this case the trajectory of electrons is aligned along the electric field symmetry axis, and directed transversely to the detector contacts, therefore the path length of the collected carriers is equal to the detector thickness *d*. The electric field distribution in the detector bulk at different bias voltage can be calculated by solving the Poisson equation for the detector volume covering 5 strips. The effective concentration in the detector space charge region needed for the computation was derived from the measured value of the full depletion voltage V_{fd}=70 V. For a bias equal to V_{fd}, N_{eff} was used as a free parameter to have a vanishing electric field at the detector n^+-contact. A space charge density of $0.89*10^{12}\,\mathrm{cm}^{-3}$ satisfied this condition. This value is lower than that given by the equation for the space charge density in a pad diode.

$$N_{eff} = \frac{2\varepsilon\varepsilon_0 V_{fd}}{e d^2} = 1.05 * 10^{12} cm^{-3} \qquad (2)$$

This is an indication of the electric field reduction for strip detectors at the pad n^+-side due to its focusing on the strips at the opposite p^+-strip side.

The two dimensional *E(x,y)* distribution calculated for a bias voltage equal to V_{fd} and the E(x) distribution along the strip axis for different bias voltage are shown in Figure 27. The electric field has a linear profile at the n^+-side, like a regular pad detector, and starts rising sharply at a distance of 30 μm from the strip.

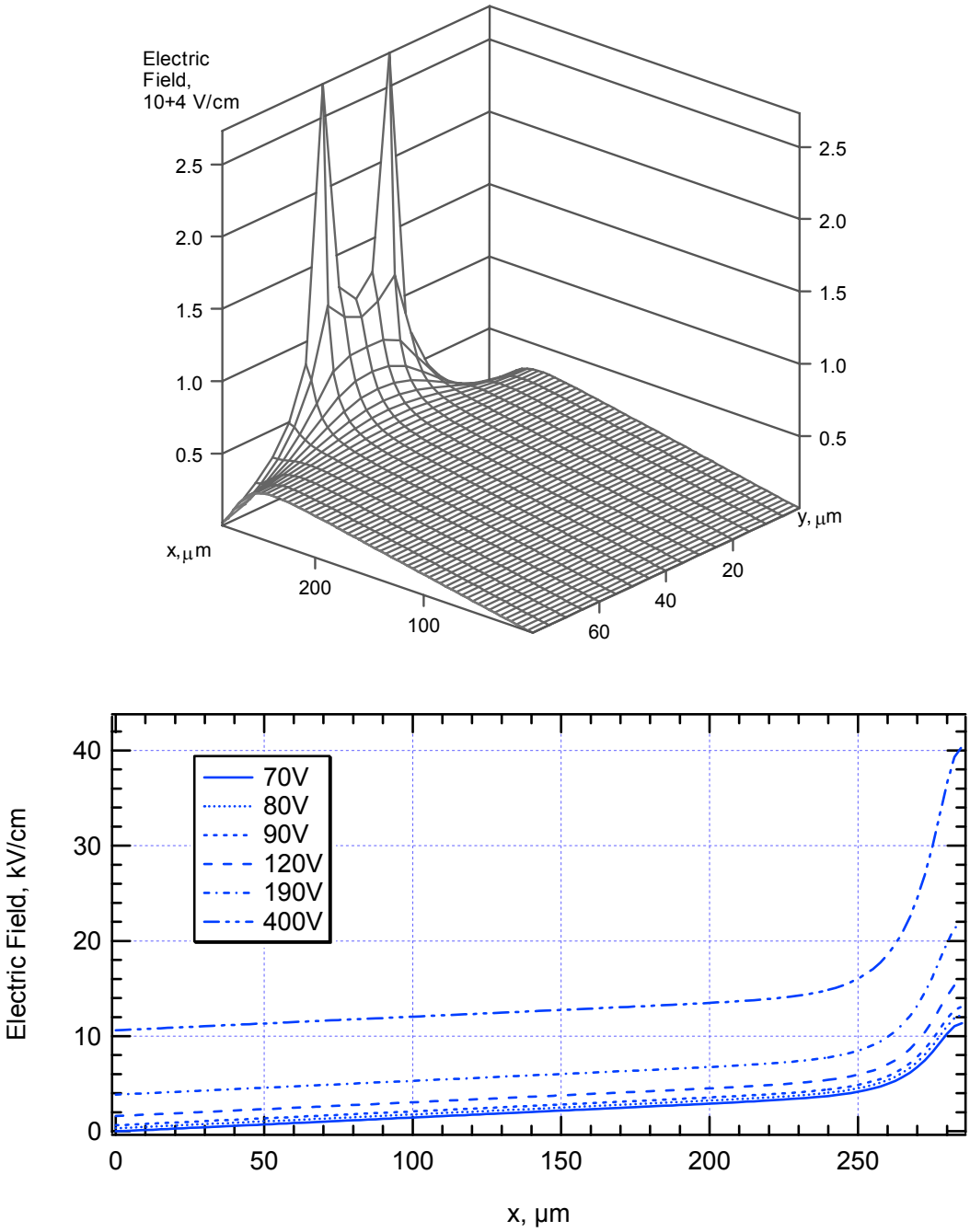

Figure 27 Two dimensional E(x,y) *distribution, at a bias voltage equal to* V_{fd}*, calculated over a region as large as the strip pitch and centred on it (top), and the E(x) distribution along the strip axis for different bias voltages (bottom).*

The calculation of the detector current pulse was performed on the basis of Ramo's theorem.

$$i(t) = -q \cdot \vec{v}(\vec{x}(t)) \cdot \vec{E}_w(\vec{x}(t)) \qquad (3)$$
$$d\vec{x} = \vec{v}(x)dt$$

The first term in eq. (3) is related to the kinetics of the charge collection *v(x(t))* and contains the dependence of the drift velocity *v* on coordinate *x* and time *t*. The second term, $E_w(x(t))$, is a weighting electric field which defines the charge induction efficiency on the readout strip. The simulation of the weighting potential used to calculate $E_w(x(t))$, is shown in Figure 28

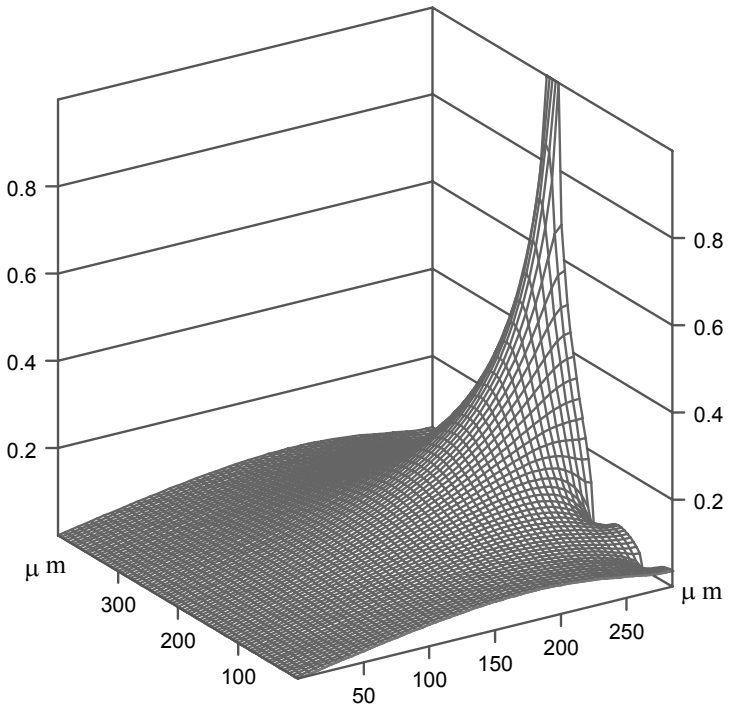

Figure 28 Weighting potential for strip detector

The corresponding convoluted pulses are shown together with the corresponding experimental pulses in Figure 29.

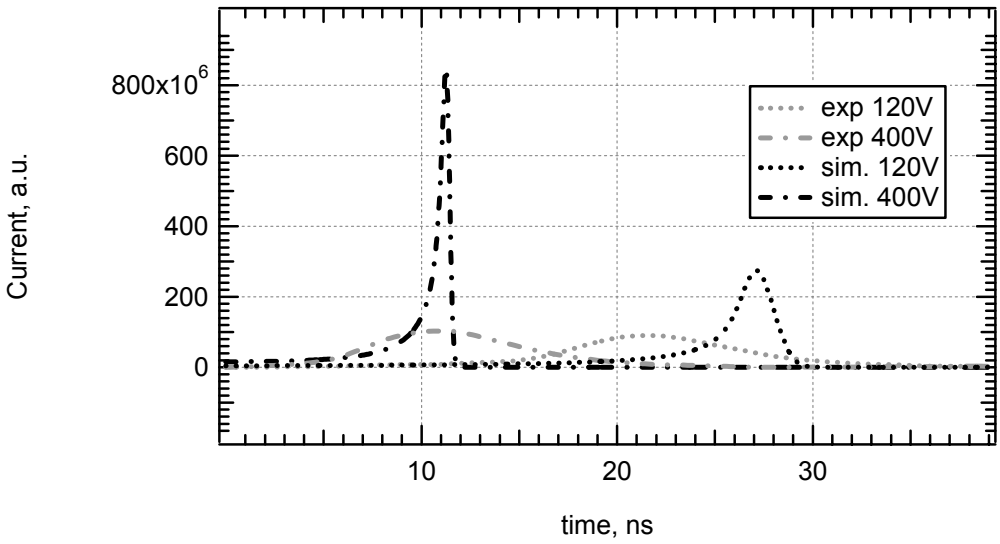

Figure 29 Comparison between the experimental and simulated pulses for different bias voltages.

The calculated pulses exhibit the same peculiarity as the experimental ones – a slow rising induction delay component and a peak. The peak time in the calculated pulses (t_{Coll}) is the time in which the holes are expected to be collected at the strip side Nevertheless, the comparison leads to several important points:

- The sharp current cut-off expected at $t=t_{Coll}$, is not observed for the experimental pulses;
- The duration of the experimental pulses is about 17 ns larger;
- The peak time of the experimental pulse (t_{max}) is close to the value of t_{Coll}.
- A significant part of the charge is collected after the drift time.

It is worth noting a small discrepancy between t_{max} and t_{Coll} at low voltage. This is due to the approximation used in the discretization to solve numerically the motion low of the carriers (cfr. equation (6) of chapter 4).

The evolution with detector bias of the peak time t_{max}, the full pulse width t_{pulse} and t_{id} are summarized in Figure 30. In this figure these quantities are also compared with the full width of the IR pulses.

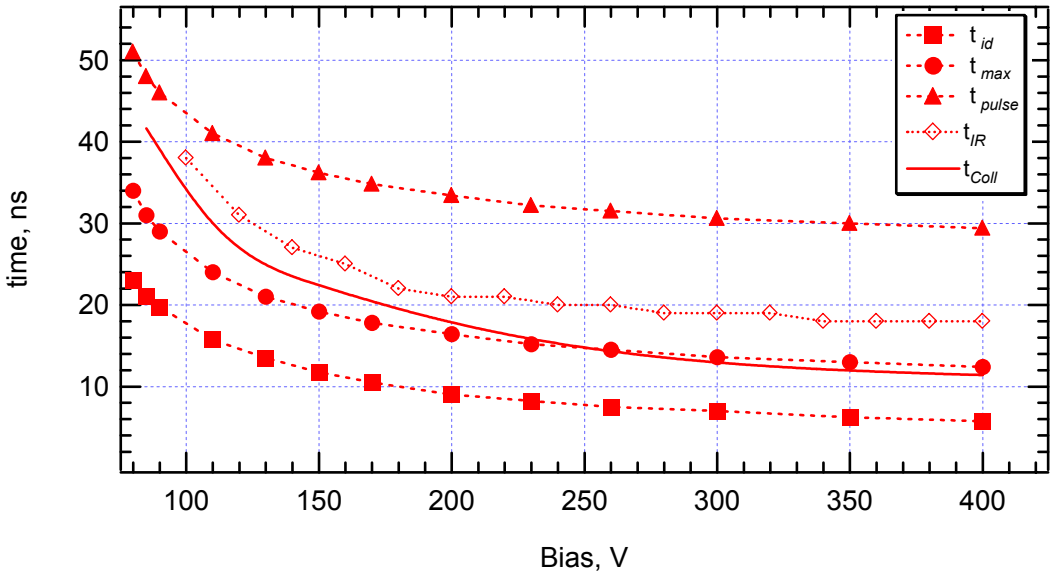

Figure 30 Bias dependence of the main parameters of the experimental and calculated pulses.

In addition to the features noted above, the fractions of the charge collected during the induction delay time (t_{id}), between t_{id} and t_{max} and during the pulse fall time (t_{pulse} - t_{max}) do not show any dependence on the applied bias. The charge that is collected after the drift time will be called the *returned charge*.

It is worth noting that the width of the IR pulse is larger than the charge collection time. This difference, although less substantial than the hole injection pulse, varies only very slightly with the bias and stays around 5 ns. In this case the returned charge is also smaller in proportion.

The model of the returned charge effect

A trivial possible explanation of the returned charge fraction is based on the charge trapping effect. In this case the collected charge is trapped during the collection time and then released by detrapping that gives rise to the returned component in the detector response. However this model is not consistent because the detector used in the experiment is not irradiated and therefore the concentration of the trapping centres is negligible and cannot explain why only 50% of the charge is collected after the drift time.

The returned charge effect can be explained within the context of Ramo's theorem extension for segmented detectors. In Figure 31 the charge induction on the electrode 2 due to the transfer of charge Q from electrode 1 to electrode 2 is shown

schematically. The potentials of electrodes 1 and 2 are φ_1 and φ_2 and do not change in time. The electrode 3 is grounded or read by an amplifier. It is important to note that all electrodes are considered as metallic with Maxwell relaxation time τ_M defined as:

$$\tau_M = \frac{\varepsilon \varepsilon_0}{e \mu n} \tag{4}$$

(where μ is the electron mobility and n is the electron concentration) much smaller than the drift time.

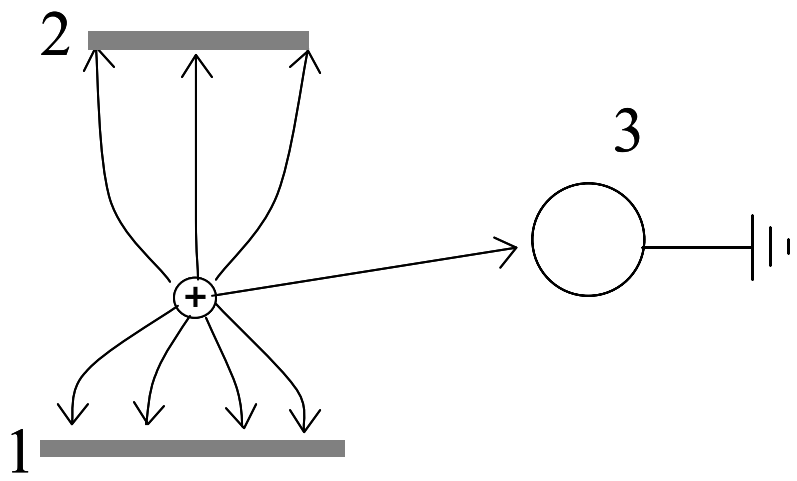

Figure 31 Schematic representation of the charge induction on the electrodes 1, 2 and 3 due to transfer of the charge Q from electrode 1 to electrode 2

It is clear that due to the fixed potentials at each electrode the initial and final electric field distribution between electrodes will be the same. Consequently the electrode 1 will collect the full charge Q, while the charge induced on the electrode 3 will be equal to zero. Therefore the current read from electrode 3 will be bipolar with equal negative and positive collected charges components. It is clear that the charge collection will be completed during the drift time and no current can flow after.

This simple consideration shows that a possible origin of the returned charge component could be related with charge redistribution (or relaxation) inside the detector after the drift time, initially disturbed by the collected charge motion between the n^+-contact and the p^+-strip. In other words in the detector bulk there must be a

volume with free carriers in which the Maxwell relaxation time is comparable with or larger than the carrier drift time.

Figure 32 presents a schematic drawing of the strip detector cross-section. For simplicity only two strips, originating at the p^+-implants and read out by the low input impedance preamplifiers, are considered. The gaps between strips are passivated by a SiO_2 layer, which contains a native trapped positive charge. Due to this charge the potential distribution at the SiO2/Si interface has a minimum at the layer of accumulated free electrons in it [6].

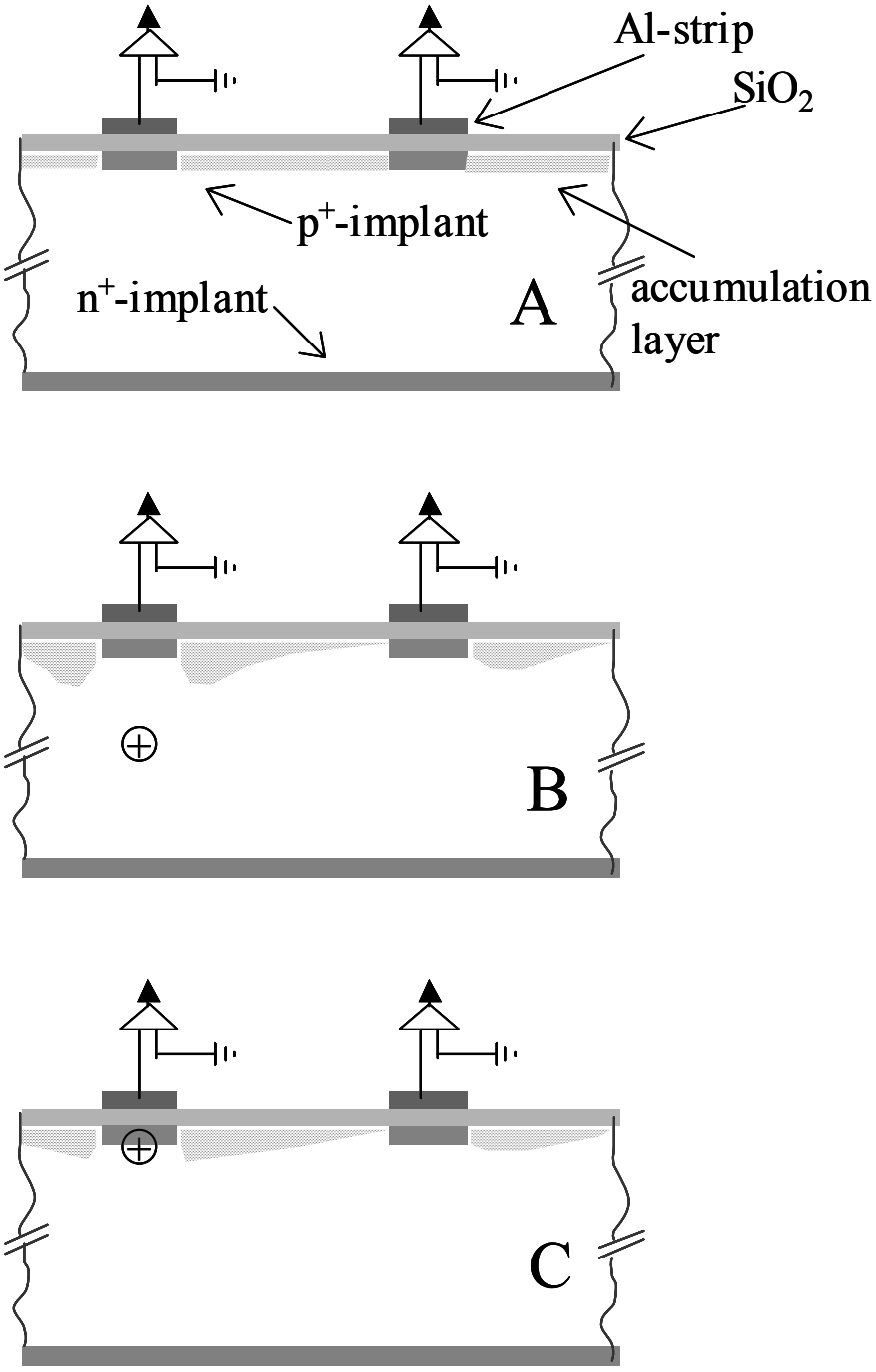

Figure 32 Schematic drawing of the strip detector cross-section. Through the cases A, B, C the process of the charge induction on the readout strip is shown.

The collected charge moving along the strip 1 axis induces a charge on strips 1 and 2 and influences the electron distribution in the accumulated layer. With decreasing distance between the charge Q and the detector strip side more electrons in the accumulated layer will be concentrated closer to strip 1, reducing the charge induced by Q. Finally, when the charge Q reaches the strip 1 at t_{dr} the non-steady-

state distribution of electrons in the accumulated layer will start to relax. For strip 1 this process is like electrons drifting away, inducing positive current.

The relaxation time for the accumulation layer can be estimated as distributed RC time constant for the layer itself, where $R = \frac{w}{\mu e n}$ and $C = \frac{\varepsilon \varepsilon_0}{w}$ are respectively the distributed resistance and capacitance and *w* is the thickness of the accumulated layer. The concentration *n* is defined by the density of the oxide charge, which is about $5*10^{11}cm^{-2}$. It is straightforward to see that RC do not depend on the accumulation layer thickness and its value is of the order of 10 ns. This value is consistent with the return charge time as defined in Figure 26. Nevertheless it has to be pointed out that RC is the decay time of the return charge process while the returned charge time has been defined as the time needed to return the full charge.

The proposed model is well supported by the experimental observation that the charge return time is constant over a wide range of the applied voltage. This indicates that the properties of the region responsible for the effect are not affected by the value of the electric field in the detector. The layer with accumulated electrons considered is strongly controlled by the density of fixed charge in the silicon dioxide layer passivating the surface between strips and therefore stable with respect to any changes in the electric field in the detector bulk. This maintains the stability of the returned charge component.

Summarizing, the returned charge effect considered is qualitatively explained as a relaxation of the layer of accumulated electrons under the SiO_2 passivated inter strip gap. The effect is significant and important for short-range particle detection. The direct proof of the model needs fabrication of microstrip detectors with specially designed construction, which is in progress.

In the case of the IR laser, the hole distribution drifting toward the strip still attract electrons toward the strip but now this is partially balanced by the repulsion due to the distribution of electrons that drift towards the back side. So, the effect of the returned charge that still exists is smaller proportion relative to the case of hole injection.

6.3.3 *After Irradiation (from 1.7*10^{14} p_{24GeV}cm^{-2} to 1*10^{15} p_{24GeV}cm^{-2})*

The measurements made on the un-irradiated sample have been repeated also for the available radiation doses. To start with the red laser, for the sample that received 1.7*10^{14} p_{24GeV}cm^{-2}, the pulses due to charge injection on the p^+-*side* in the region between two strips show the same peculiarities seen in the unirradiated sample, with a positive polarity in the region close to the readout strip turning to a negative polarity as the injection point approaches the neighbouring strip. For a bias of 200 V these pulses are shown in Figure 33. This behaviour correlates well with the charge collection at these points as seen in Figure 9.

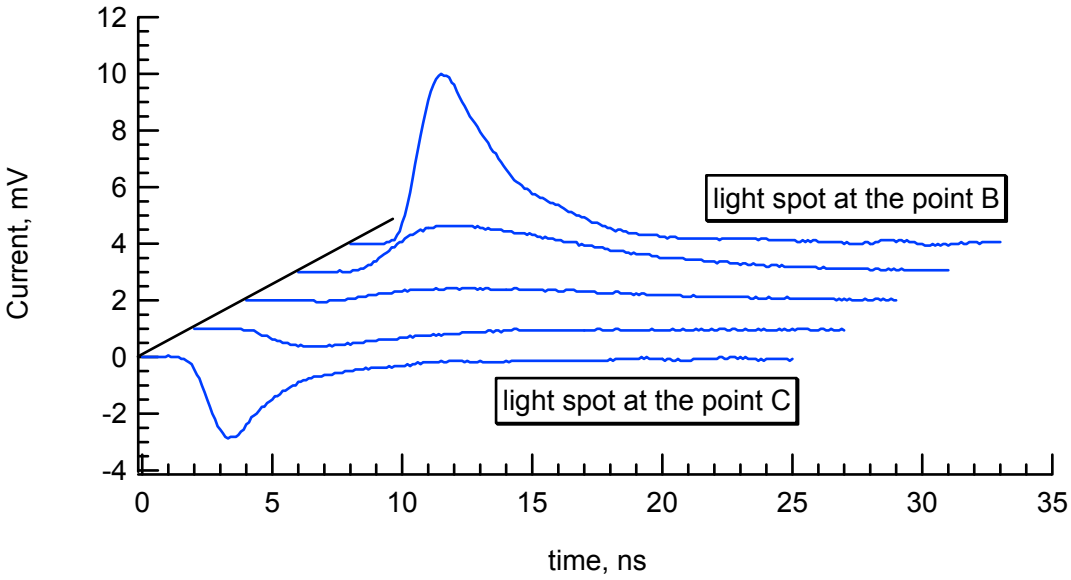

*Figure 33 Current pulses measured with red laser illumination of the p^+-side of the detector in the region delimited by the readout strip and the adjacent one. The detector irradiated at 1.7*10^{14} p_{24GeV}cm^{-2} is fully depleted and biased with 200 V.*

Concerning the signal due to the red laser injection at the n^+-*side*, at full depletion the current pulse still shows a slow rising component followed by a peak component (see Figure 34) for the laser spot at the point A and a bipolar pulse when the laser approaches the adjacent strip axis.

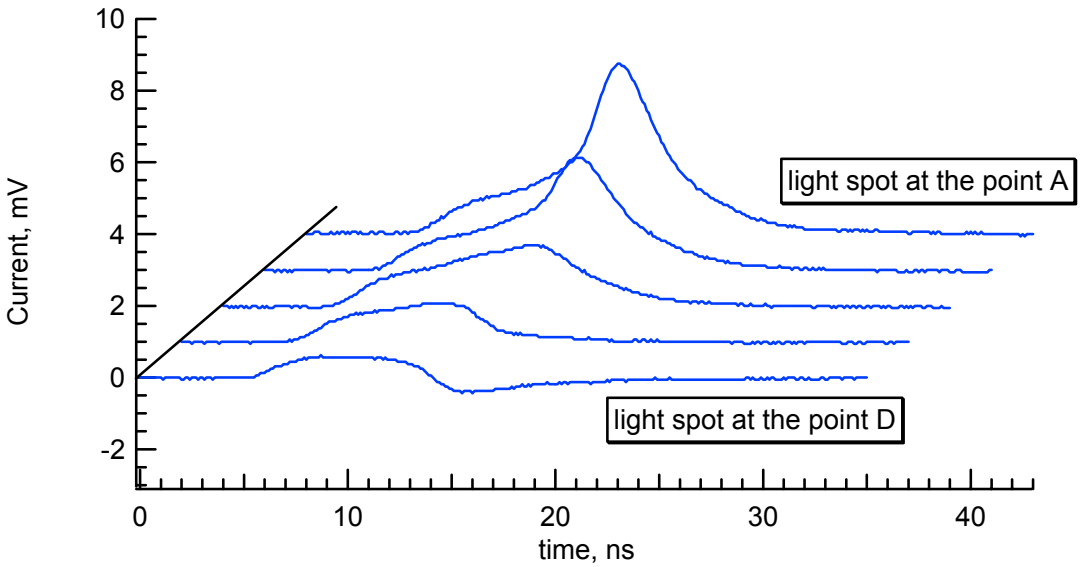

Figure 34 Current pulses measured with red laser illumination of the n^+-side of the detector in the region delimited by the readout strip and the adjacent one. The detector irradiated at $1.7*10^{14}$ $p_{24GeV}cm^{-2}$ is fully depleted and biased with 200 V.

An interesting difference in the pulse shape with respect to the un-irradiated case appears for bias lower than the full depletion voltage. It is worth remembering that at this dose bulk inversion has already appeared and in fact the presence of signal due to hole injection at the backside confirms this hypothesis. Nevertheless as explained in the previous chapter, for low bias, when the depleted region is confined in areas away from the strips where the weighting potential for each single strip is only weakly dependent on the coordinate orthogonal to the strip direction, the signal due to hole injection is like that of a pad detector with the junction at the back side. This can be seen in Figure 35. The current pulses due to charge injection at the point A show that at lower voltages the amplitude of the signal is higher at the beginning and then it slowly decreases to vanish within 30ns. Increasing the bias to achieve full depletion (about 200 V) changes this trend to a faster charge collection and a corresponding continuous increase in the signal amplitude. As the full depletion is achieved the pulse becomes very similar to the one before irradiation, with the only difference that the *induction delay* part of the signal is replaced by a step. The pulse cut off is still very long, lasting around 15 ns for all values of the bias.

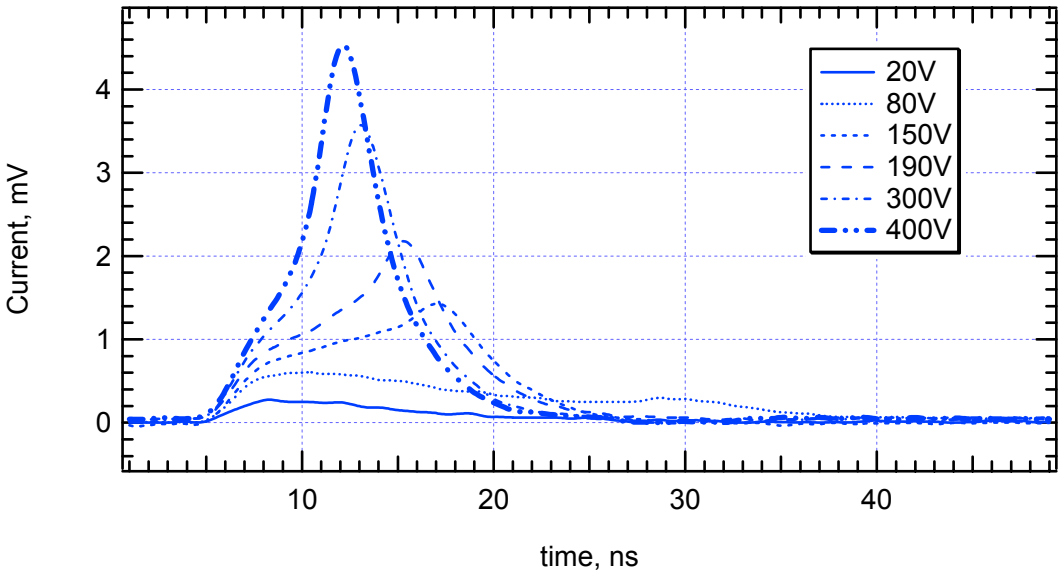

Figure 35 Current pulses measured with red laser illumination of the n^+-side of the detector pointing on the read out strip axis, for different bias voltages. The detector is irradiated at $1.7*10^{14}$ $p_{24GeV}cm^{-2}$.

Furthermore given the weak dependence of the weighting potential on the x coordinate, the signals recorded at low voltage when the injection point is at the points D (see Figure 36) and A are very similar. Nevertheless, in the first case the initially positive current pulse starting at low bias turns bipolar as the voltage increases, i.e. as the charge depletion gets closer to the strip side.

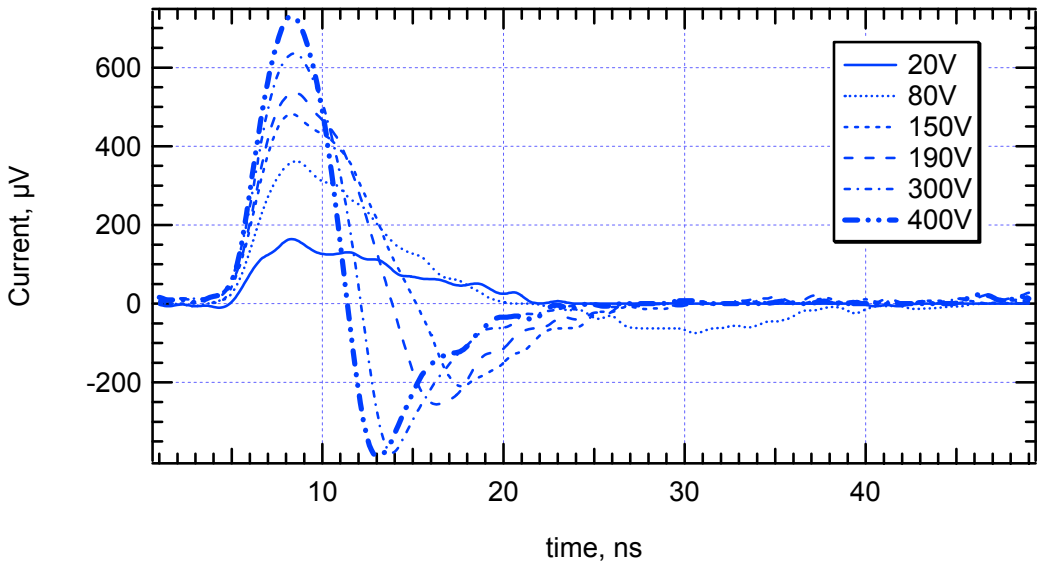

Figure 36 Current pulses measured with red laser illumination of the n^+-side of the detector pointing on the strip adjacent to the read out strip, for different bias voltages. The detector is irradiated at $1.7*10^{14}$ $p_{24GeV}cm^{-2}$.

The pulse shape due to illumination with the IR laser has also been analyzed. In this case there are no major variations with respect to a non-irradiated detector. The signal varies from positive polarity with the laser at the point B (or A) and towards bipolarity as the laser spot approaches the point C (see Figure 37).

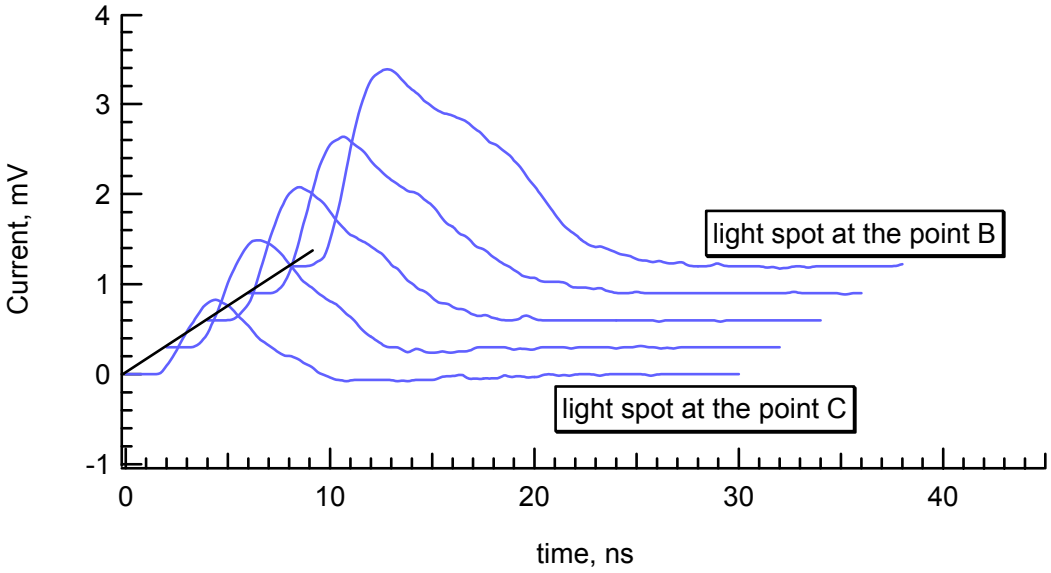

Figure 37 Current pulses read out from strip1 for infrared laser illumination of the n^{+}-side of the detector between points B and C The detector irradiated at $1.7*10^{14}$ $p_{24GeV}cm^{-2}$ is fully depleted and biased with 200 V.

Also the pulse timing remains unchanged once the detector is depleted (bias higher than 200V). In this condition, the full pulse width is shorter than 25 ns. A selection of pulses when the IR light is on the point A is shown in Figure 38.

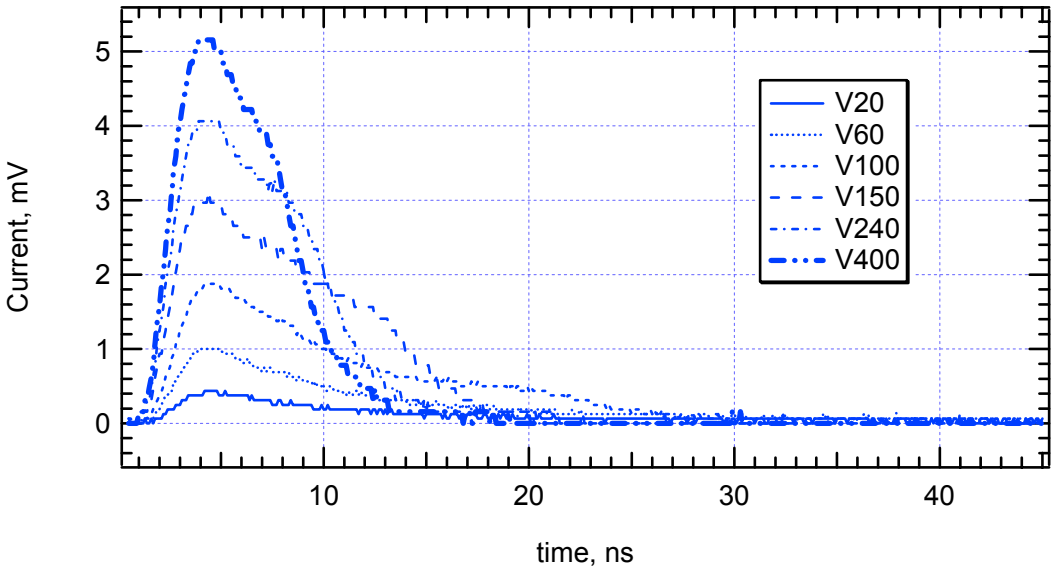

Figure 38 Voltage scan of the current pulses due to infrared illumination at the point A. The detector is irradiated at $1.7*10^{14}$ $p_{24GeV}cm^{-2}$.

With double the dose, fluence of $4*10^{14}$ $p_{24GeV}cm^{-2}$, the detector's full depletion bias has risen to 400 V. Nevertheless there are still many similarities in the pulse shapes compared to the previous dose. Figure 39 and Figure 40 show the pulse scans over a region between two adjacent strips for red laser illumination of the strip side and the backside respectively.

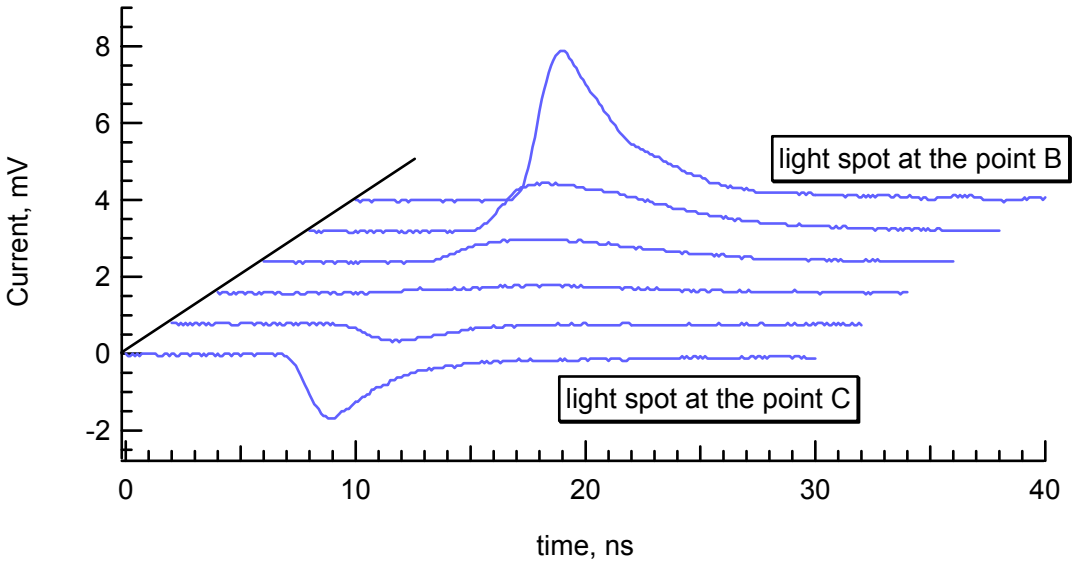

Figure 39 Current pulses measured with red laser illumination of the p^+-side of the detector in the region delimited by the readout strip and the adjacent one. The detector irradiated at $4*10^{14}$ $p_{24GeV}cm^{-2}$ is partially depleted and biased with 200 V.

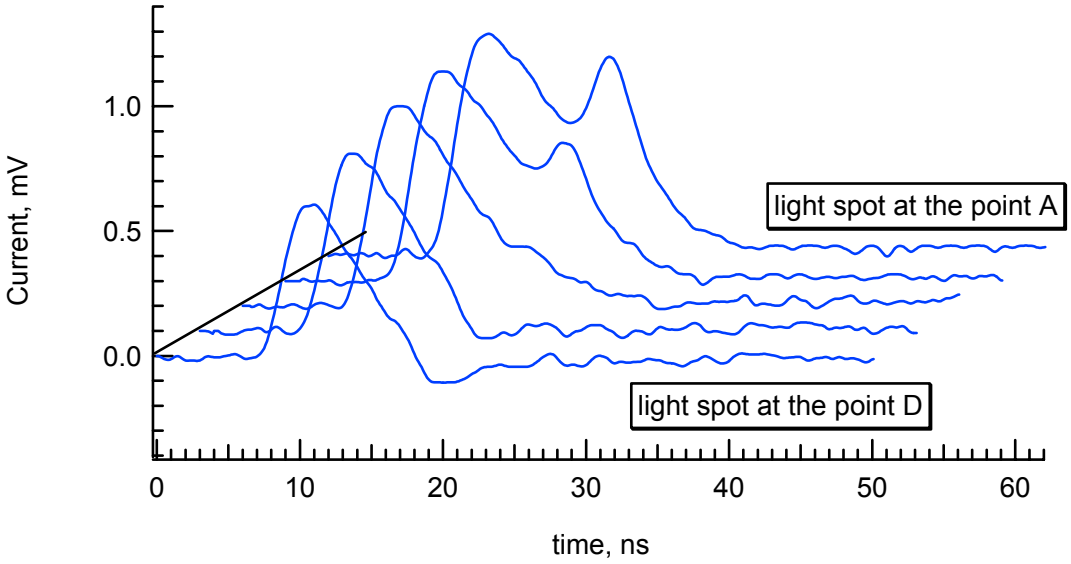

Figure 40 Current pulses measured with red laser illumination of the n^+-side of the detector in the region delimited by the readout strip and the adjacent one. The detector irradiated at $4*10^{14}\ p_{24GeV}cm^{-2}$ is partially depleted and biased with 200 V.

For laser injection from the back side the feature of the initial step is stronger at this dose, as seen in Figure 40 where the pulses were measured with the red laser at point A. It is also worth noting that the pulse width does not change much with the bias.

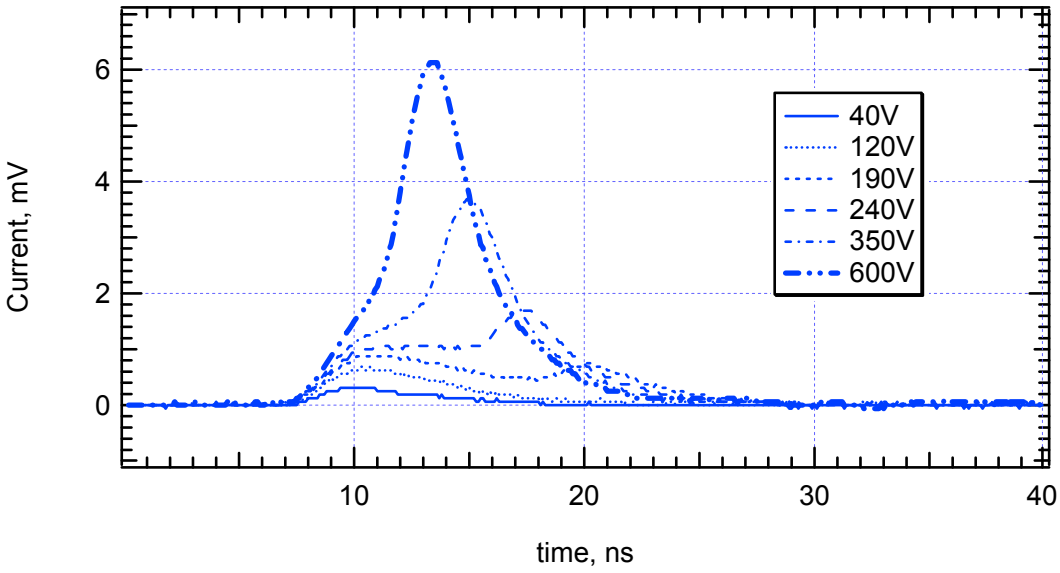

Figure 41 Current pulses measured with red laser illumination of the n^+-side of the detector pointing on the read out strip axis, for different bias voltages. The detector is irradiated at $4*10^{14}\ p_{24GeV}cm^{-2}$.

In similar manner, for low bias the responses with the light spot at point D present a similar pulse shape to the one at point A, turning to bipolar pulses as the bias increases.

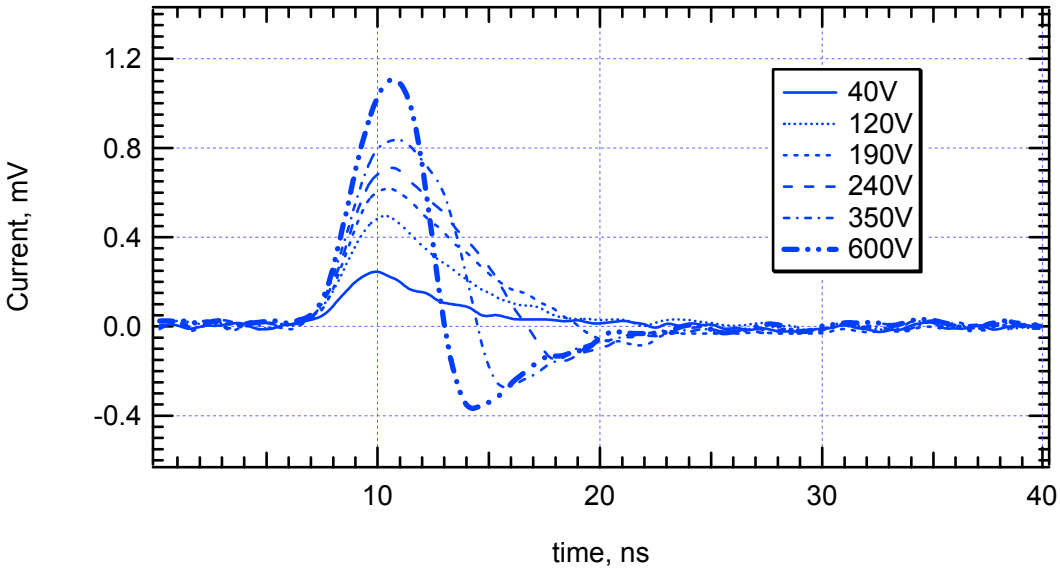

Figure 42 Current pulses measured with red laser illumination of the n^+-side of the detector pointing on the strip adjacent to the read out strip, for different bias voltages. The detector is irradiated at $4*10^{14}\ p_{24GeV}cm^{-2}$.

In the case of the IR laser the current response amplitude decreases with the distance from the read out strip. At low bias, (lower than the full depletion voltage),

the polarity stays positive everywhere. Only on approaching V_{fd} does the pulse become bipolar when the laser beam gets closer to the strip adjacent to the one read out (see Figure 43,Figure 44 and Figure 45). This is the same as at the lower irradiation dose.

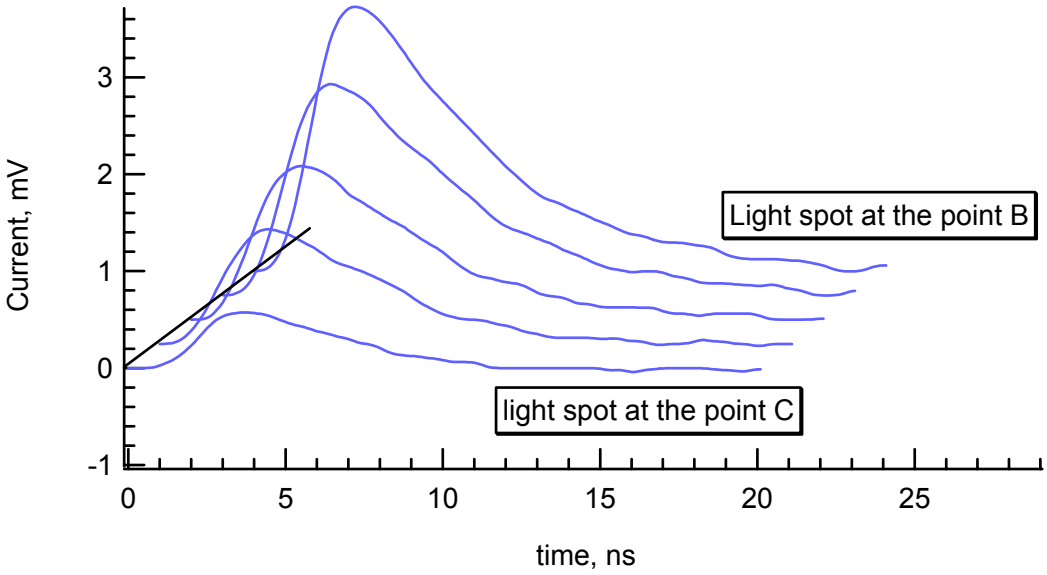

Figure 43 Current pulses read out from strip1 for infrared laser illumination of the n^+-side of the detector between points B and C The detector irradiated at $4*10^{14}\ p_{24GeV}cm^{-2}$ is only partially depleted and biased with 200 V.

Nevertheless an interesting feature that appears at this dose is the pulse width, which is almost independent of the voltage and is shorter than 20 ns.

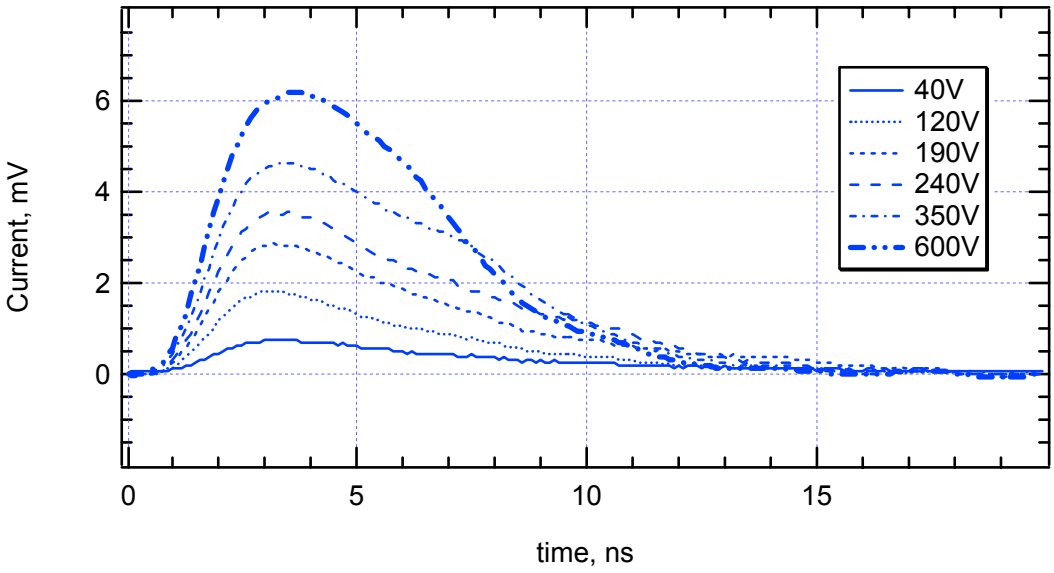

Figure 44 Voltage scan of the current pulses read out of strip1 due to infrared illumination at the point A. The detector is irradiated at $4*10^{14}$ $p_{24GeV}cm^{-2}$.

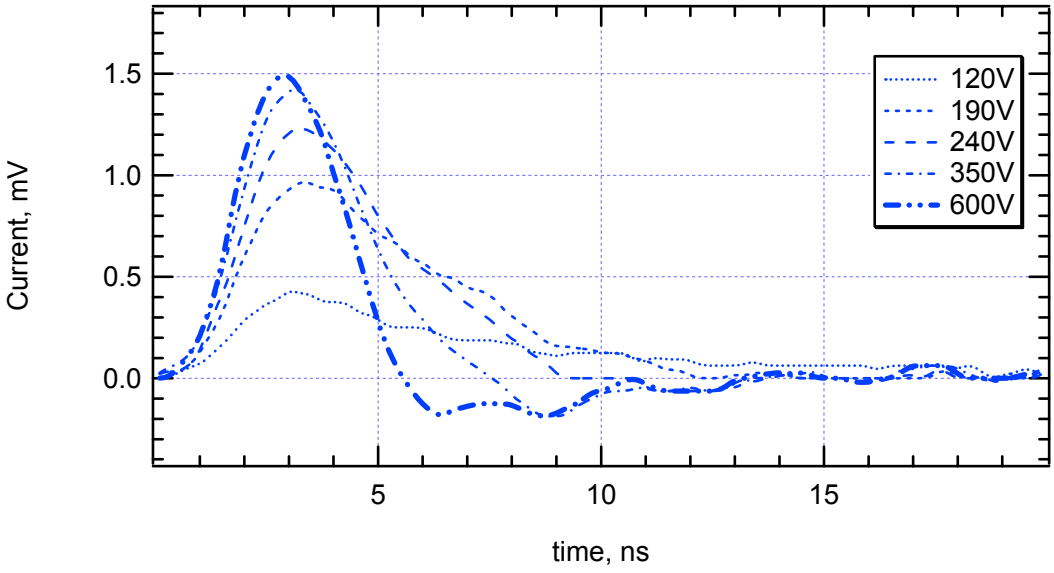

Figure 45 Voltage scan of the current pulses read out of strip1 due to infrared illumination at the point D. The detector is irradiated at $4*10^{14}$ $p_{24GeV}cm^{-2}$.

A dramatic change appears at the fluence of $1*10^{15}$ $p_{24GeV}cm^{-2}$. It is worth remembering that at this high dose the full depletion cannot be achieved due to setup limitations and probably the full depletion voltage stands over 1800 V. Then all the measurements done at this dose can be compared with the ones at lower doses for bias lower than V_{fd}, when the signal is rather small.

The first striking result is that at this dose it is impossible to measure any signal from carrier injection at the back side, no matter what the bias is.

Nevertheless, charge injection on the strip side gives rise to a signal that is shown in Figure 46. Differently from the other doses, in this case the current signal measured at the adjacent strip has bigger amplitude than that of the signal due to the laser beam at the readout strip.

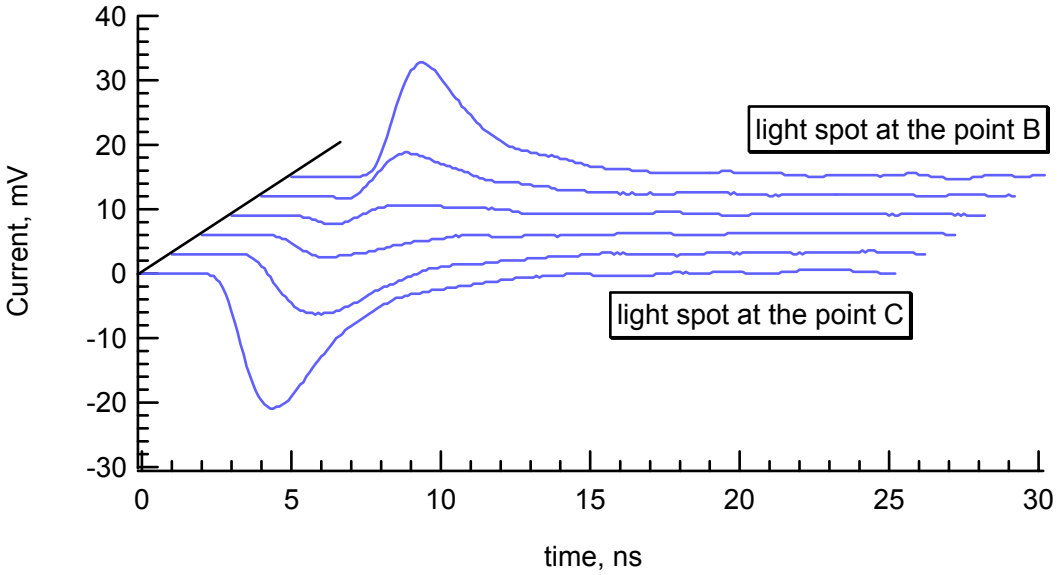

Figure 46 Current pulses measured with red laser illumination of the p^+-side of the detector in the region delimited by the readout strip and the adjacent one. The detector irradiated at $1*10^{15}$ $p_{24GeV}cm^{-2}$ is biased with 200 V.

The current pulse due to the IR laser illumination has also been measured, showing over the whole bias range a behaviour that is very close to that at the previously analysed dose for a bias lower than V_{fd}. In the Figure 47 is shown the signals for the laser beam in the region between two strips.

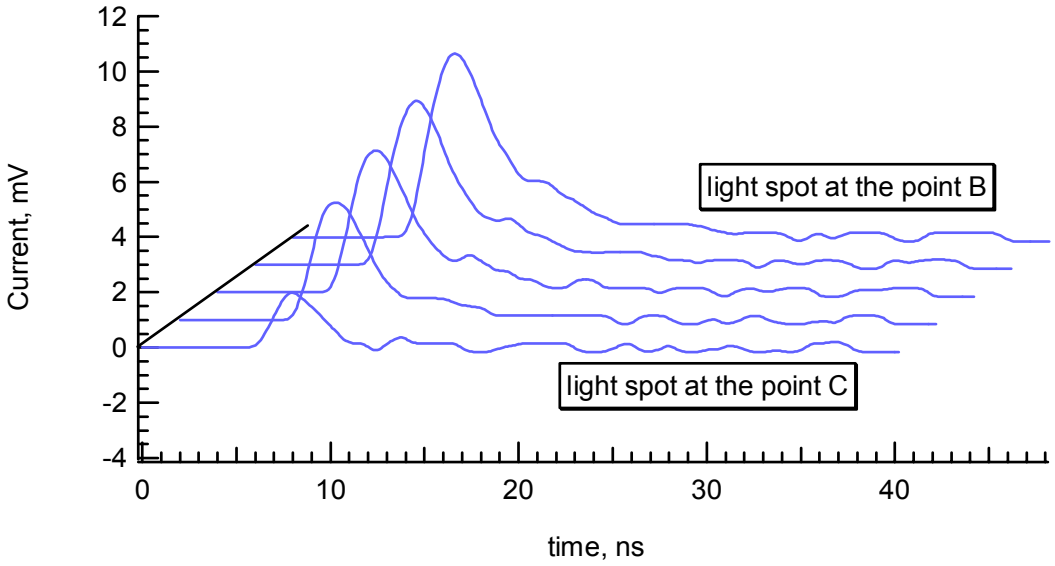

Figure 47 Current pulses read out from strip1 for infrared laser illumination of the n^+-side of the detector between points B and C The detector irradiated at $1*10^{15}$ $p_{24GeV}cm^{-2}$ is only partially depleted and biased with 200 V.

It is interesting that the pulse width for IR laser illumination is not affected by the bias. Figure 48 shows the pulses measured when the IR laser beam is close to the readout strip. As can be seen all the pulses vanish within 20 ns

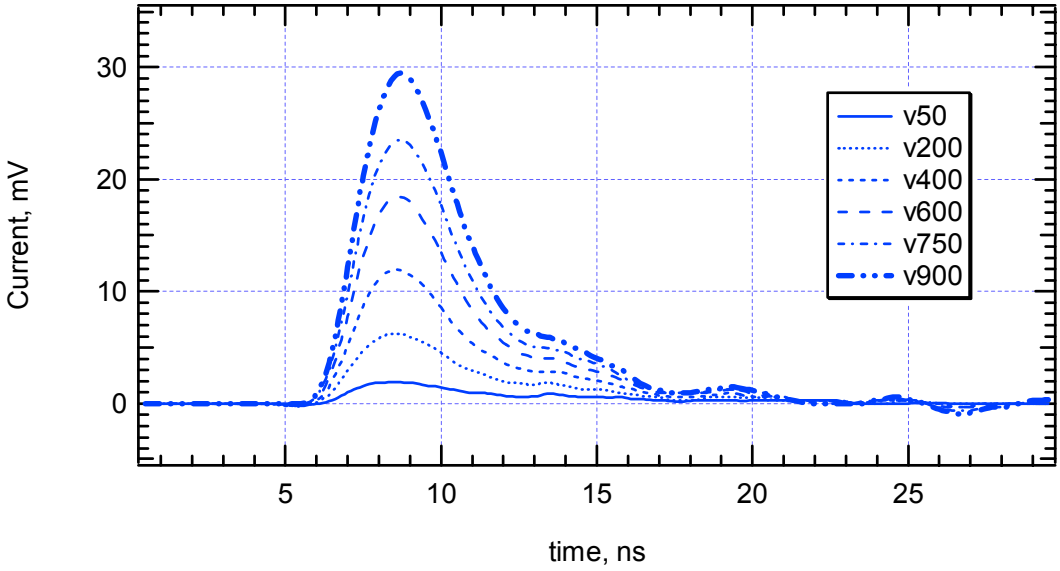

Figure 48 Voltage scan of the current pulses read out of strip1 due to infrared illumination at the point A. The detector is irradiated at $1*10^{15}$ $p_{24GeV}cm^{-2}$.

The double peak effect

The current pulses measured with irradiated samples have shown many interesting features. As already discussed for the charge collection, these

measurements first of all reject the model that describes the effect of the irradiation only as an inversion of bulk conductivity type. In other words, although it is true that these highly irradiated detectors start to deplete from the back side they seem to show sensitivity on the front side also at low voltage. A more appropriate model for the electric properties of the silicon after high hadron irradiation may be that described in [7] which, as previously discussed, assumes in biased detector a steady state carrier filling of traps which is not uniform throughout the detector thickness. This non-uniformity is manifested as a positive space charge region towards the back side and a negative space region at the strip side. These two regions extend towards the back side with increasing bias until they meet. This feature corresponds to a double peak electric field which has been clearly seen in pad detectors. In strip detectors this double peak is distorted due to the focusing of the electric field lines at the strips. In particular, hole injection at the back side as illustrated in Figure 35 and Figure 41 shows this feature before the bias approaches the full depletion voltage. At full depletion the high efficiency of the signal induction at the strip prevails, giving a peaked current pulse shape. The double peak probably appears only when the depletion extends to the region where the weighting field is almost constant over the along the strip axis, just as in pad detectors.

While this has seen to be true up to a dose of $4*10^{14}\, p_{24GeV}cm^{-2}$, at $1*10^{15}\, p_{24GeV}cm^{-2}$ the striking absence of any signal for hole injection on the back side has not been fully explained yet. One possible reason may be the very short extinction length of the holes at this fluence. In this case the distance traversed by these carriers is limited to a thin region close to the back side where the very low weighting potential for the read out strip does not allow the induction of a signal wide enough to be detected with the available setup.

Apart from the signal shapes, another interesting feature to look at in the irradiated samples is the signal timing. For the sample irradiated at $1.7*10^{14}\, p_{24GeV}cm^{-2}$, the IR pulse length is unchanged relative to the unirradiated sample once full depletion is reached and decreases with further bias. On the other hand, for the two most irradiated samples, the timing seems not to be affected at all by the bias and all the IR pulse widths are within 20 ns. These peculiarities merit further

investigation for a deeper understanding of the processes which silicon undergoes after a heavy irradiation.

6.4 References

[1] V. Eremin et al, NIM A372 (1996) 388-398.

[2] V. Eremin, J. Bohm, S. Roe, G. Ruggiero, P. Weilhammer, C*harge collection in single side silicon microstrip detectors*. To be published in NIM A

[3] CERN LHC/ ATLAS SCT/ Detector FDR/ 99

[4] G. Ruggiero, V. Eremin, S. Roe, *Application of Transient Current/Charge Technique for measurement of full depletion voltage in heavily irradiated strip detectors*. Submitted to NIM A

[5] A. Alberigi-Quaranta, M. Martini, G. Ottaviani, "The pulse shape and the timing problem in solid-state detectors - a review paper". IEEE-NS16-2 (1969) pag. 35.

[6] B.E. Deal, M. Sklar, A. S. Grove and E. H. Snow, "Characteristics of the Surface-State Charge (Q_{ss}) of Thermally Oxidized Silicon", J. Electrochem. Soc. 114, 266-274, March 1967

[7] V. Eremin et al. A476 (2002) 556-564.

7 Summary and Conclusions

Silicon detectors are doubtless essential tracking devices in modern high energy experiments. Nevertheless the high requirements of LHC have raised some questions on their performance over the whole period of data taking. This concern has pushed the scientific community to produce systematic studies on the radiation hardness of silicon over the last ten years to achieve a better comprehension of the damaging mechanism due to radiation in silicon. A lot has been done but still many questions are unsolved. This thesis work has been animated by the purpose of a better understanding of the degradation of performance of these devices when high irradiation occurs. In this context a deep study of the signal formation in silicon detectors and in particular in microstrip detectors with the geometry foreseen for the ATLAS Semiconductor Tracker has been proposed. Moreover a big attention in this study has been put also in some operational techniques that would improve the radiation hardness of silicon.

For what concerns the improvement of the radiation hardness of Silicon with low temperature operation (~130 K) in this thesis has been proven that the temperature of irradiation does not change very much the formerly studied recovery at low temperature of the Charge Collection Efficiency (CCE) in highly irradiated silicon detectors. It has also shown that reverse annealing consequent to a long permanence at room temperature after low temperature irradiation does not influence the CCE as well. This would allow the use of silicon detectors at low temperature which would benefit of an extended life with respect to the case of room temperature use. Moreover, the cooling would be needed only during data taking and eventual thermal cycles to room temperature that could be required for maintenance operation would not affect the recovery at all. The mechanism of recovery has been studied and seems to be the result of two competing phenomena: first the reduction of the space

charge density with the temperature (i.e. neutralisation of the charged trapping centres) allowing the reduction of full depletion voltage down to 130 K, and then, at a temperature lower than 130 K, the reduction of the trapping time due to the increase of the carrier capture cross-section would be the dominant effect leading to the decrease of the CCE experienced after 130 K.

The study of signal generation has been fundamental for the development of this thesis. For this purpose a software package to simulate numerically the electric properties of the silicon detectors and the signal generation due to mip radiation has been developed. A particular attention has been given to the geometry of the microstrip detectors foreseen for the ATLAS Semiconductor Tracker. For the case of irradiated detectors, some of the parameters required for the simulation have been taken from experimental results. Among the main outcomes of this simulation work is the asymmetry found in the contribution of holes and electrons to the charge signal. The asymmetry existing between contribution of holes and electrons is due to the particular shape of the weighting potential. The fact that among the charge carriers holes contribute more is because they are the carrier type collected at the electrode read out. This could suggest a device with n^+-type strips on n-type bulk (and the junction on the back contact) especially for applications with fast electronics given the fact that electrons are nearly three times faster than holes. Moreover also for radiation hard applications, when carrier trapping becomes relevant, this type of device would have the advantage that for a comparable trapping time of the two different carriers the charge collected at the read out strip electrode would be higher due to a longer drift length of electrons respect to holes, for a given bias voltage.

Another relevant outcome of the simulation is the fact that for fluences foreseen at the ATLAS semiconductor tracker radii the CCE would overcome the 50% even after the severe dose of $4*10^{14}{}_{24GeV}$proton/cm^2 for a bias voltage of 600 V. Moreover in these conditions, for tracks crossing the detector perpendicularly at the centre of one strip, the charge signal at the adjacent strip would still be at least ten times smaller than the signal at the strip crossed by the mip and guaranteeing still a small amount of two strip-clusters in the highly irradiated detector.

Together with the simulation of microstrip detectors, in the thesis work a wide experimental activity has been performed. Most of it has been based on the Transient

Current/Charge Technique (TC/ChT) measurements. This has required first the development and realisation of a very powerful automatic TC/ChT setup. The automatic mode of this setup has allowed a very fine scanning of several samples irradiated at different doses up to the extreme one of $1*10^{15}_{24GeV}$proton/cm^2.

The outcome of these measurements is a detailed study of the signal generation in microstrip detectors. Among the main features analysed are the effects due to the presence of the accumulation layer underneath the SiO_2 layer that passivates the strip surface. The accumulation layer has been found to influence the charge collection for carrier generation at the strip surface, away from the implanted strip. In fact measurements done in this thesis show that electrons generated in these regions stay in this layer without crossing the detector bulk. Moreover this accumulation layer also influences the timing of the charge collection (*returned charge*) due to the redistribution of the charge in the accumulation layer when the radiation generated carrier drifts towards the electrodes. Those effects are present in both irradiated and non irradiated detectors. In irradiated detectors it has also been investigated how the trapping as well as incomplete depletion can appear as a charge sharing mechanism for fluences up to $*10^{15}_{24GeV}$proton/cm^2. The striking feature found is that for doses up to $4*10^{14}_{24GeV}$proton/cm^2 depleting the detector is enough to reduce the charge sharing to a reasonable level and moreover further improvements can be observed with high bias operation, while for the extreme dose of $1*10^{15}_{24GeV}$proton/cm^2 even for the bias voltage of 950 V the charge sharing is so high that the strip pattern is completely lost.